High power 2 μm fiber laser for mid-infrared supercontinuum generation in fluoride fibers

Giuseppe Scurria

THÈSE PRÉSENTÉE
POUR OBTENIR LE GRADE DE

DOCTEUR DE L'UNIVERSITÉ DE BORDEAUX

SCIENCES PHYSIQUES ET DE L'INGÉNIEUR
LASERS, MATIÈRE, NANOSCIENCES

par Giuseppe SCURRIA

HIGH POWER 2 µm FIBER LASER FOR MID-INFRARED SUPERCONTINUUM GENERATION IN FLUORIDE FIBERS

Sous la direction de : Inka MANEK-HÖNNINGER

Thèse soutenue le 6 décembre 2019 devant le jury composé de :

Dr. ABDOU AHMED, Marwan	*IFSW, Stuttgart*	Rapporteur
Dr. BALCOU, Philippe	*CELIA, Bordeaux*	Examinateur
Dr. BIGOTTA, Stefano	*ISL, Saint-Louis*	Encadrant
Dr. COUDERC Vincent	*XLIM, Limoges*	Président/Rapporteur
Pr. MANEK-HÖNNINGER, Inka	*CELIA, Bordeaux*	Directrice
Dr. HILDENBRAND-DHOLLANDE, Anne	*ISL, Saint-Louis*	Encadrante, invitée
Dr. PAOLACCI-RIERA, Sylvie	*DGA, Paris*	Invitée

Titre : Laser à fibre à 2 µm de forte puissance pour la génération de supercontinuum dans le moyen infrarouge dans les fibres en verre fluoré

Résumé :

Le développement de sources optiques ayant une forte brillance et un large spectre est nécessaire pour différentes applications telles que les contremesures optroniques, les systèmes LIDAR et la spectroscopie. Ce travail de thèse est consacré à l'étude de la génération de supercontinuum de forte puissance dans le domaine spectral allant de 2 à 5 µm. Un laser à fibre dopé thulium, émettant à 2 µm, a été réalisé et caractérisé en régimes continu, déclenché et à verrouillage de modes déclenchés. En régime continu, une puissance de 45 W a été atteinte avec un rendement différentiel de 58%. L'intégration de deux embouts en quartz fondu, fusionnés aux extrémités de la fibre active, a permis une amélioration drastique du contrôle de la température et de la stabilité générale du système dans tous les régimes de fonctionnement précédemment mentionnés. En régime combiné, de verrouillage de modes déclenchés, la puissance moyenne maximale en sortie de laser était de 40 W à une fréquence de déclenchement de 150 kHz. Pour une puissance moyenne en sortie de 20 W et une fréquence de déclenchement de 50 kHz, l'impulsion verrouillée la plus énergétique avait une énergie de 88 µJ et une puissance crête estimée de 60 kW. Dans tous les régimes de fonctionnement mentionnés, le facteur de propagation du faisceau M^2 était proche de la limite de diffraction avec une excellente valeur de 1,1. Le faisceau de ce laser fibré a été utilisé pour pomper des fibres optiques en fluorure pour la génération de supercontinuum dans le domaine spectral de 2 à 5 µm. Les travaux expérimentaux ont été focalisés sur les matériaux en fluorure que sont le ZBLAN et le fluorure d'indium (InF_3). Avec la fibre en ZBLAN, plus de 10 W ont été générés sur l'ensemble du domaine spectral avec une limite supérieure de domaine spectrale allant jusqu'à 4,4 µm. L'efficacité de conversion du supercontinuum a été mesurée à 35%, 28%, 15% et 8% pour un faisceau généré de longueur d'onde supérieure à 2,15 µm, 2,65 µm, 3,1 µm et 3,5 µm, respectivement. Concernant la fibre en InF_3, la réalisation d'un nouveau système d'injection (combinant une fibre ZBLAN large coeur et un coupleur commercial fibre à fibre) a permis d'atteindre une grande stabilité thermo-mécanique de la fibre pendant les expériences à haute puissance. La génération de supercontinuum dans cette fibre s'est concrétisée par un faisceau de sortie dont le spectre atteignait la longueur d'onde de 4,7 µm et une puissance de 7 W sur l'ensemble du domaine spectral. À notre connaissance, ceci est le premier faisceau supercontinuum, ayant une puissance de l'ordre de quelques watts, généré dans une fibre en InF_3 pompée par un oscillateur unique.

Mots clés : Fibre laser impulsé, fibre en verre fluoré, génération supercontinuum

Title: High power 2 µm fiber laser for mid-infrared supercontinuum generation in fluoride fibers

Abstract :

High brightness and broad spectrum optical sources in the mid-infrared (mid-IR) are promising for different applications such as optronic countermeasures, LIDAR systems and spectroscopy. This thesis research work is dedicated to the investigation of high power supercontinuum generation in the 2-5 µm range. A thulium-doped fiber laser emitting at 2 µm has been built and characterized in continuous wave, Q-switching and Q-switched mode-locking regime. In continuous wave operation, as much as 45 W have been reached with a slope efficiency of 58%. The implementation of two fused-quartz end-caps fusion spliced at the extremities of the active-fiber improved the thermal management and the overall stability of the entire system in all mentioned regimes of operation, allowing for higher pump powers. In Q-switched mode-locking, the maximum average output power level was 40 W, for a Q-switch repetition rate of 150 kHz. At the average output power level of 20 W and 50 kHz of Q-switch repetition rate, the most energetic mode-locked pulse had an energy of 88 µJ and an estimated peak power of ~60 kW. In all the mentioned operation regimes, the measured beam parameter M^2 of the fiber laser was 1.1, close to the diffraction limit. This laser has been used to pump fluoride optical fibers (ZBLAN and InF_3) for supercontinuum generation in the 2-5 µm range. In ZBLAN, more than 10 W in all spectral bands have been obtained, with an output spectrum extending up to 4.4 µm. A conversion efficiency of 35%/28%/15%/8% has been measured for wavelengths longer than 2.15 µm/2.65 µm/3.1 µm/3.5 µm, respectively. For the InF_3 fiber, a new design of an injection system, consisting of a large core diameter ZBLAN optical fiber and a commercial fiber-to-fiber coupler, allowed to enhance the thermo-mechanical stability of the fiber. The supercontinuum radiation generated in InF_3 showed an output spectrum spanning up to around 4.7 µm with an output power level of 7 W in all spectral bands. To the best of our knowledge, this was the first Watt-level supercontinuum radiation in an InF_3 fiber pumped by a single-oscillator.

Keywords : Pulsed mid-infrared lasers, fluoride fibers, supercontinuum generation

---

Unité de recherche

CELIA (Centre Lasers Intenses et Applications)

UMR5107 CNRS – Université de Bordeaux – CEA

43 Rue Pierre Noailles Bat C6

33400 TALENCE

Acknowledgements

It was not easy. This PhD has been a truly life-changing experience for me and it would not have possible to complete it without the support and advice that I received from all the people around me.
First, I have to thank the ISL directors for giving me the opportunity to perform my thesis at ISL. It was a pleasure to work in such well organized and friendly environment. I would also like to express my gratitude to DGA for funding my PhD thesis; thank to Dr. Adam for his support and Dr. Paolacci-Riera for having accepted the invitation to be part of my jury.
I want also to thank Dr. Abdou Ahmed and Dr. Couderc for having accepted to review my manuscript and to be part of the jury for my defense.
I want to thank Dr. Balcou for being part of the jury.
My infinite gratitude goes to the three most important people during my PhD thesis: my thesis director Prof. Inka Manek-Hönninger: despite the distance, she has always been available, kind and helpful. She had the power to always cheer me up when the things were not so shiny.
Dr. Anne Hildenbrand-Dhollande that without any hesitation accepted to be my tutor at ISL. She really showed me what it means to be a group leader: ready to listen, to discuss and propose solutions. Dr. Stefano Bigotta without his guidance and constant feedback this PhD would not have been achievable. But most of all, for sharing with me truly powerful and soothing words that helped me change the course of my PhD and, maybe, of my life. I will never forget that. Thank you a lot, you were the lights at the end of my dark tunnel.

I also have to thanks all the colleagues of the DPA group at ISL, it was a real pleasure to work in such a friendly group. Special mention goes to Dr. Nicolas Dalloz for his help during the implementation of the "end-caps" for my laser. My office neighbor Stephan Schmitt, it is also thanks to you if now I can speak French. To my colleagues Dr. Louot and Dr. Piotrowsky for reading my manuscript and giving me important advises. To Mr. Christen, Mr. Loll and Mr. Bontemps for the realization of many mechanical parts necessary for my laboratory setup.
I would also like to say a heartfelt thank you to my Mum, Dad and my brother Salvatore for always believing in me and encouraging me to follow my dreams.
And finally my special dedication to Stefania for being simply the most beautiful thing in my life.

Why do we fall, Bruce? So we can learn to pick ourselves up

Thomas Wayne
"Batman begins"

Writing is a lonely job. Having someone who believes in you makes a lot of difference.

Stephen King
"On Writing: A Memoir of the Craft"

Synopsis

L'étude de la génération de radiations lasers dans la région de l'infrarouge moyen, en particulier entre 2 μm et 5 μm, a connu un fort essor au cours des dernières années. Les sources optiques à large bande d'émission et à forte brillance sont nécessaires pour de multiples applications, parmi lesquelles les communications en espace libre, la télédétection chimique ou encore les contremesures optroniques. Cette thèse est consacrée à l'étude de la génération de supercontinuum de forte puissance dans la bande spectrale située entre 2 μm et 5 μm. La génération de supercontinuum est un processus d'obtention d'un large spectre de longueurs d'onde continu par la propagation d'impulsions optiques (que l'on appelle alors pompe) à travers un milieu non linéaire. Dans la mesure o les effets non linéaires impliqués dans ce processus requièrent de fortes intensités pour être stimulés, il est d'usage d'avoir recours à des systèmes lasers impulsionnels pour jouer le rôle de source de pompe. Cependant, les systèmes à blocage de mode (mode-lock , ML) ou à commutation de gain (Q-switch, QS) couramment utilisés pour générer des impulsions lasers délivrent des niveaux de puissances crêtes insuffisants pour les applications visées dans cette thèse. Par ailleurs, la configuration à amplificateur de puissance d'oscillateur matre (en anglais, MOPA) qui utilise un laser matre suivi de plusieurs chaines d'amplifications est souvent préférée. Dans ces conditions, des diodes lasers à rétroaction répartie émettant des impulsions d'une durée proche de 1 ns ou bien des lasers fibrés à blocage de mode passif émettant des impulsions de l'ordre de la picoseconde ont déjà été utilisés. Dans le premier cas, pas moins de trois amplificateurs sont nécessaires pour

atteindre les puissances nécessaires au pompage à forte puissance tandis que dans le second cas, le supercontinuum généré dans l'infrarouge moyen en a requis au moins deux. Le système entier d'une configuration MOPA semble donc à la fois compliqué et onéreux, du fait qu'il demande un nombre important de diodes de pompes, de fibres actives, d'isolateurs ou encore de composants permettant la mise en forme du faisceau. Dans cette thèse, un laser basé sur l'utilisation d'une fibre en silice dopée aux ions thulium placée dans un oscillateur simple et émettant des impulsions autour de 2 μm est utilisé pour pomper un milieu non linéaire et ainsi générer un supercontinuum dans l'infrarouge moyen de plusieurs watts de puissance. Ce laser agit simultanément en régime de commutation de gain et de blocage de mode, de façon à générer des trains d'impulsions présentant une puissance crête suffisante pour stimuler les effets non linéaires responsables de l'élargissement spectral. Pour induire le double procédé de commutation de gain et de blocage de mode (que l'on appellera QSML) simultanément, deux modulateurs acousto-optiques non fibrés sont placés dans la cavité laser en espace libre. Cette architecture laser permet d'atteindre des puissances crêtes très élevées et des niveaux d'énergie d'impulsion importants sans l'action d'un quelconque amplificateur externe. Le premier supercontinuum généré le fut dans des fibres de silice du fait de la bonne maitrise de la fabrication des fibres avec ce matériau, leur conférant une bonne résistance aux conditions atmosphériques et une certaine robustesse. Toutefois, la fenêtre de transmission des fibres de silice empêche l'émission de longueurs d'onde au-delà de 2,8 μm. La volonté de générer un supercontinuum entre 3 μm et 5 μm impose alors de se tourner vers des fibres arborant de plus faibles pertes dans l'infrarouge moyen, et par conséquent d'abandonner la silice au profit d'autres matériaux tels que les fluorures. Les verres de fluorozirconate (ZrF_4-BaF_2-LaF_3-AlF_3-NaF, souvent appelé ZBLAN par souci évident de facilité) ou le fluorure d'indium (InF_3) sont actuellement considérés comme les milieux non linéaires les plus prometteurs pour la génération de supercontinuum dans l'infrarouge moyen. Bien

que les fibres de ZBLAN permettent le transport de fortes puissances, leur fenêtre de transmission ne s'étend que jusqu'à 4,5 μm. Dès lors, les fibres de InF_3 semble être de bonnes candidates puisqu'elles sont transparentes jusqu'à 5,5 μm. Elles subissent cependant un retard de maturation technologique qui ne leur permet pas à l'heure actuelle d'atteindre les niveaux de puissances obtenus dans les fibres de ZBLAN. Au cours de cette thèse, la plupart des expériences sur des lasers impulsionnels basés sur l'utilisation de fibres de silice dopées aux ions thulium ont été menées en régime QSML. Il est à noter que le régime continu et le régime simplement QS ont également été étudiés. En régime continu, des puissances lasers jusqu'à 45 W ont été atteintes, correspondant à une efficacité de 58%. L'ajout de deux embouts (end-caps) en quartz fondu, soudés aux deux extrémités (distale et proximale) de la fibre a amélioré la gestion thermique et la stabilité globale du système laser complet pour l'ensemble des régimes temporels mentionnés. Cette amélioration a permis de travailler avec de plus fortes puissances de pompe. La commutation de gain seule a ainsi permis de générer une puissance de sortie de 40 W, pour différents taux de répétition. L'énergie la plus élevée obtenue a été de 350 μJ, pour une durée d'impulsion de 48 ns, correspondant à une puissance crête de 7 kW. En régime QSML, la seconde modulation du train d'impulsions (issu du blocage de mode) par l'enveloppe de commutation de gain a entrainé la génération d'impulsions à très forte énergie. L'impulsion la plus énergétique obtenue et utilisée pour la génération de supercontinuum présentait une énergie de 88 μJ et une puissance crête d'environs 60 kW (huit fois supérieure à la puissance générée par le régime de commutation de gain seul). Les impulsions obtenues par le régime QSML présentait dans le domaine temporel la forme d'un pic entouré d'un piédestal, de durées respectives 30 ps et 1,6 ns. La qualité du faisceau en sortie de laser a été évaluée pour les trois régimes temporels par l'intermédiaire du facteur M^2, calculé à chaque fois proche de la limite de diffraction ($M^2 = 1{,}1$). Concernant la génération de supercontinuum, une fibre de ZBLAN et deux tronçons de fibre

de InF_3 ont été utilisés. Les performances du supercontinuum alors généré ont été systématiquement évaluées, à la fois par la mesure de l'efficacité de conversion spectrale, du niveau de puissance totale à la sortie du laser et de l'étendue du spectre généré. La fibre de ZBLAN utilisée, d'une longueur de 20 m, avait un diamètre de coeur de 12 μm et une ouverture numérique de 0,23. Son utilisation a permis de générer plus de 10 W sur l'ensemble du spectre, étendu jusqu'à 4,4 μm. Dans les meilleures conditions de conversion, la mesure de la puissance dans différentes bandes du spectre a permis d'identifier la répartition de la puissance dans le supercontinuum : 35 % de sa puissance au-delà de 2,15 μm, 28 % au-delà de 2,65 μm, 15 % au-delà de 3,1 μm et jusqu'à 8 % convertis vers les longueurs d'onde supérieures à 3,5 μm. L'une des deux fibres de InF_3 utilisée avait un coeur de 7,5 μm de diamètre et une ouverture numérique de 0,3. Les instabilités thermique et mécanique ont été réduites par le recours à un nouveau système d'injection, composé d'une fibre de ZBLAN à large coeur et d'un coupleur fibre à fibre commercial. Ainsi, il a été possible de générer un supercontinuum jusqu'à 4,7 μm à travers la fibre de InF_3, dont la puissance totale s'élevait à 7 W. Il s'agit de la première démonstration de supercontinuum de plusieurs Watts généré dans une fibre de InF_3 placée dans un système de pompage par oscillateur simple.

Contents

Chapter 1

Introduction

The generation of laser radiation in the mid-infrared (mid-IR) wavelength region, especially between 2 μm and 5 μm, has been widely studied during the last decades . The large demand of high brightness and broad spectrum optical sources is required in different applications. One example of application is in the telecommunication sector for free-space applications, where it is possible to use several transmission windows of the atmosphere [1]. Other applications for mid-IR sources are optronic countermeasures [2] or remote chemical sensing for molecules or species with spectral fingerprints in the mid-IR, e.g. explosives [3]. The strong water absorption in this wavelength region offers also interesting applications in the medical and biomedical field like tissue ablation [4], optical coherence tomography [5] or Coherent Anti-Stokes Raman Scattering (CARS) microscopy [6].

Supercontinuum generation is nowadays widely investigated to target wavelengths in the mid-IR. It is a method to generate broad continuous spectra by propagating optical pulses through a non-linear medium. The field of supercontinuum generation gained additional interest with the developing of optical fibers. Owing to the guiding properties of fibers, it is possible to maintain a high intensity interaction over the entire length of the fiber. The non-linear interaction is therefore not limited to few millimeters (as in the case of gases, liquid cells or crystals). This puts optical fibers in the posi-

tion of best candidates for supercontinuum generation, offering to the entire system robustness and compactness.

In this thesis research work, I was responsible of the development and the improvement of a high power Q-switched mode-locked thulium-doped silica fiber laser emitting at 2 μm. In addition, I used this laser to pump different optical fibers to generate Watt-level supercontinuum radiation in the wavelength region 2 - 5 μm. Q-switched mode-locked operation provides sufficient peak power levels for the realization of a single-oscillator pump source for supercontinuum generation, without the need of amplifier chains. This is very beneficial regarding the complexity and the compactness of the entire system.

To address the spectrum window 2 - 5 μm, the use of fluoride glasses fibers is mandatory because of their transparency at longer wavelengths compared to standard silica which is transparent up to 2.6 μm. In particular, I used fluoride materials such as ZBLAN (a composition of ZrF_4, BaF_2, LaF_3, AlF_3 and NaF) and InF_3 during this thesis. The use of a thulium fiber laser as pump arises from the fact that the wavelength conversion during supercontinuum generation is much more efficient if the non-linear material is pumped in its anomalous dispersion region, namely in the region in which the chromatic dispersion is negative. This means that the pump radiation experiences a negative dispersion. This is obtained by pumping the optical fiber with a pump wavelength longer than the zero dispersion wavelength. The zero dispersion wavelength of the used fluoride fibers lies between 1.6 μm and 2 μm, dependent on the fiber design making the thulium-doped silica fiber laser emitting at 2 μm suitable for this application.

This thesis is composed by six chapters, including this introduction, and structured as follows:

Chapter 2 introduces the theoretical description of a fiber laser, with particular focusing on the electronic transitions in thulium-doped silica that are most relevant when used as a 2 μm source. The main techniques for

generating optical pulses are described: Q-switching, mode-locking and Q-switched mode-locking. Furthermore, a review of the state of the art of continuous wave and pulsed thulium-doped fiber laser systems is done at the end of the chapter.

Chapter 3 covers the theoretical background of fiber optics, including the description of the linear and non-linear fiber propagation effects in single-mode step-index fibers. These effects are then used to qualitatively explain the process of supercontinuum generation depending at which dispersion region (normal or anomalous) the fiber is pumped. At the end of the chapter, an overview of the main materials for mid-IR supercontinuum generation is presented together with an analysis of the state of the art in the scientific literature.

Chapter 4 presents the results obtained from my thulium doped fiber pump laser. The setup is described with all the optical elements, the available active-fiber and all the measuring tools used for the investigation. The results are then separated into three different operating conditions: continuous wave, Q-switching and Q-switched mode-locking.

Chapter 5 contains the results of supercontinuum generation in fluoride fibers pumped by the thulium-doped silica fiber laser. I mainly investigated ZBLAN and InF_3 material as non-linear fibers. Special attention is given to the description of the fiber preparation (stripping and cleaving) and light coupling which are more sophisticated compared to standard silica fibers. The experimental setup for preparing the laser beam before coupling into the core of the non-linear fiber is presented with all the optical elements used. Then, an analysis of the supercontinuum spectrum evolution is studied depending on different parameters such as the pump power levels and pulse energies. Finally, the results of the high power experiments are described together with a comparison with the state of the art in the scientific literature.

Chapter 6 resumes the achieved results and gives an outlook for future supercontinuum generation experiments.

Chapter 2

Thulium-doped fiber lasers

In this chapter the theoretical background of fiber lasers is given. Much attention is dedicated to the electronic transitions in thulium-doped silica that are most relevant when it is used as source emitting at 2 μm. Then, the theories of Q-switching, mode-locking and Q-switched mode-locking techniques are reported. At the end of the chapter, the state of the art in the literature of continuous and pulsed thulium-doped fiber laser systems is presented.

2.1 Theory

2.1.1 Fiber lasers

Fiber lasers offer many attractive features that bulk solid-state lasers lack. These characteristics include: high gain per unit length, efficient pump coupling/absorption via the double-clad design, high brightness and excellent beam quality due to the single-mode propagation inside the core. There are many configurations in which a laser can be realized. The essential elements of a solid state laser device are:

- a **laser medium** consisting of an appropriate collection of atoms, molecules, ions or in some instances a semiconducting crystal;

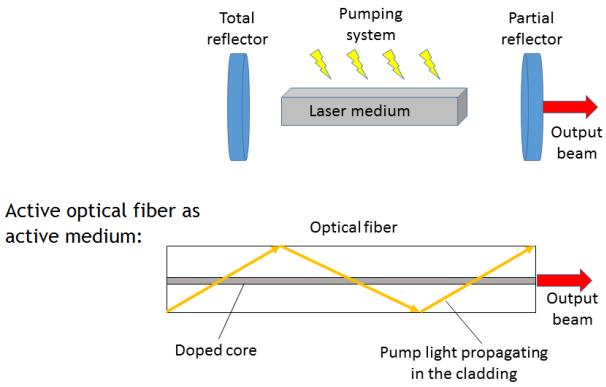

Figure 2.1: *top:* Generic scheme of a laser; a gain medium that is excited, and a cavity formed by two mirrors to allow the build up of laser light. *bottom:* In the case of a fiber laser, the active medium is replaced by a doped optical fiber.

- a **pumping setup** to excite these atoms into higher quantum-mechanical energy levels;
- an **optical feedback** system that allow a beam of radiation to either pass through the laser medium or bounce back and forth through the laser medium.

The fiber laser developed and improved during this thesis acts in a similar way. The optical fiber is used as active medium and it is inserted in an optical cavity which allows the amplification of the stimulated light. A schematic drawing of a laser system is shown in Figure 2.1. Rare-earth elements are used to dope the fiber core to make it an active medium. A characteristic feature of the trivalent rare earth ions is that their electronic transitions usually occur within the 4f shell, which is shielded from the host lattice by the optically passive outer electronic shell [7]. This reduces the influence of the host lattice on the wavelengths, bandwidths and cross sections of the relevant optical transitions. If the fiber ends are perpendicularly cleaved,

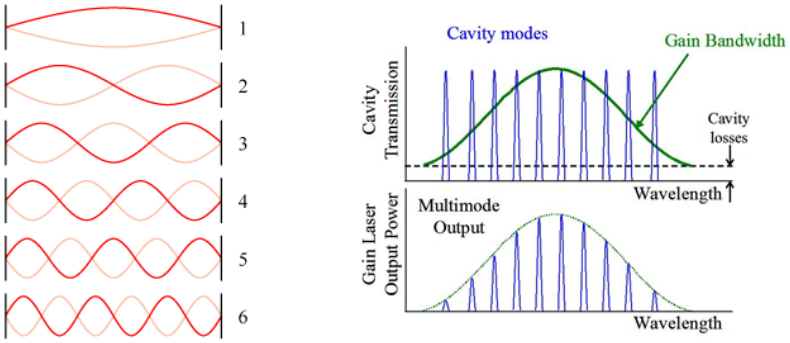

Figure 2.2: *left:* A linear cavity formed by two mirrors can sustain an infinite number of longitudinal modes; *right:* The modes are equally spaced in frequency across the gain spectrum of a laser.

even the small Fresnel reflection from the ends (e.g. $\approx 4\%$ for SiO_2 glass at 2 μm) can provide enough feedback for lasing action if the gain is much greater than the total losses inside the cavity. This is only the simplest form of a fiber laser. In a laser resonator there are many longitudinal modes that can oscillate (Figure 2.2). They are separated by $\Delta\nu = c/2L$ where c is the speed of light and L is the optical length of the cavity. The finite spectral width of the gain medium sets a limit to the number of modes that can oscillate inside the optical cavity. The inverse of this frequency spacing gives the round-trip time of the cavity $\tau_{rp} = 1/\Delta\nu$, namely the time light takes to make one complete propagation cycle inside the cavity. The existence of these longitudinal modes becomes important in Section 2.1.4 where the mode-locking method to create pulses will be explained.

Another important parameter for a cavity is the Q-factor. This value is related to the ratio between the energy stored in the cavity to the energy lost per cycle. The Q is related to the amount of time a laser photon is contained inside the cavity (large values of Q refer to longer storage times). It can be shown [8] that for a laser resonant frequency ν_o of a spectral width $\Delta\nu$ the Q-factor is approximated to:

$$Q \approx \frac{\nu_o}{\Delta\nu}\mathcal{F}, \tag{2.1}$$

where $\mathcal{F}$ is the *finesse* of the cavity defined by:

$$\mathcal{F} = \frac{\pi}{2\sin^{-1}\left(\frac{1-\sqrt{\rho}}{2\sqrt[4]{\rho}}\right)}, \tag{2.2}$$

where ρ is the percentage of the circulating power lost after one round-trip of the cavity. In the case of low round-trip losses (e.g. $< 10\%$, indicating high Finesse values), Equation 2.2 can be approximated as follows:

$$\mathcal{F} \approx \frac{\pi}{1-\sqrt{\rho}} \approx \frac{2\pi}{1-\rho}. \tag{2.3}$$

One can controle the Q-factor of a laser by changing the conditions inside the cavity (e.g. either introducing losses or changing the pumping conditions). This will become the subject of Section 2.1.3, where the Q-switching technique for pulse generation is introduced.

One of the most significant advantages of fiber lasers is their power-scalability. The large surface area to volume ratio makes fiber lasers excellent devices to release excess heat produced from high power pumping. However, problems can occur when directly pumping the core. At high power operation, despite the favourable geometry of the optical fiber, thermal effects become significant. Also, in terms of the laser process, unwanted effects such as excited state absorption (multiple absorptions of pump photons from already excited states) may occur that terminate the lasing process. Therefore at high powers it is often desirable to absorb the pump power over a longer distance, and one way to achieve this is to use a double-clad fiber geometry. As the name indicates, a double-clad fiber has two claddings. The core is doped with rare-earth elements and often designed to be operating only at the fundamental mode. It is then surrounded by a cladding which guides the pump light that, due to its larger diameter, is highly multi-mode. As the cladding guides the pump light, the guided modes intersect with the doped

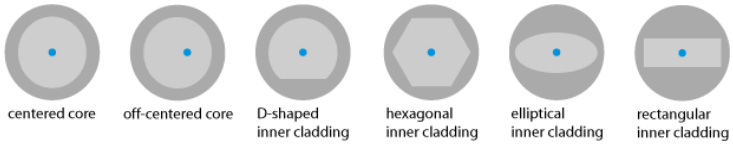

Figure 2.3: A series of double-clad fiber geometries are shown (image adopted from [11]).

core. In this way, pumping of the rare-earth ions is performed distributively over a longer distance. Another benefit of this structure is that coupling light into the larger cladding is easier than into the core, relaxing the conditions on the spatial beam quality of the pump light. This allows high power laser systems to be pumped by relatively low-cost laser diodes. Since the large dimension of the cladding, it can support highly multi-mode beams, and the spatial distribution of the pump light can be very complicated. For circular claddings there are modes that do not have an efficient overlap with the core and thus can lead to low absorption of the pump, making the laser inefficient. It has been reported that changing the shape of the cladding can produce better light absorption [9]. Figure 2.3 shows some commonly used cladding structures. Numerical studies of mode-overlaps have been performed on various cladding shapes [10, 11]. The choice of the shape of the cladding results in a trade-off between high absorption in the core and more practical characteristics, such as difficulties of fabrication, cleaving and splicing.

2.1.2 Thulium-doped fiber lasers

Thulium-doped fiber lasers provide emission in the 2-μm spectral region [12]. One important feature of lasers emitting wavelengths above 1.4 μm is to be considered eye-safe, because their radiation is absorbed in the vitreous body of the human eye before reaching the retina [13]. Since the first reported thulium-doped laser with yttrium aluminum garnet (YAG) as host material in 1965 [14], high power 2 μm sources are attractive for applications in: exploiting the high atmospheric transmission window beyond 2 μm for directed

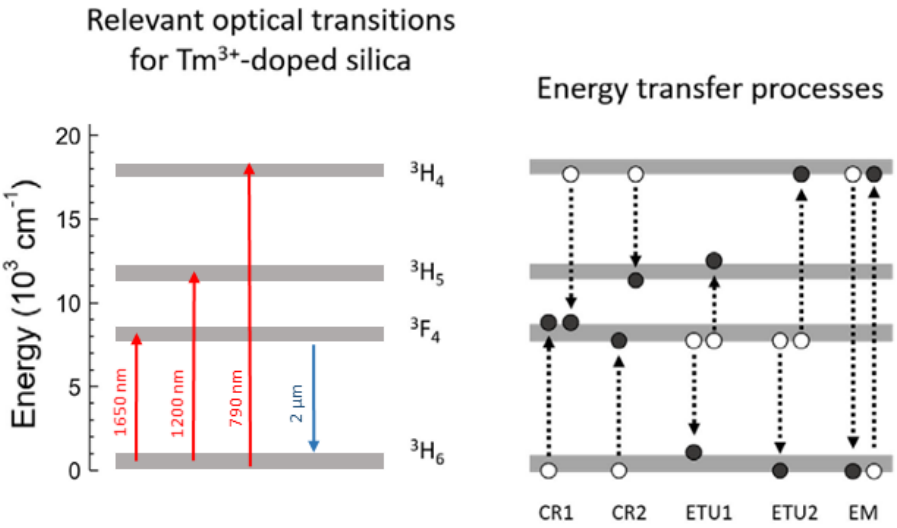

Figure 2.4: *left*: Radiative transitions relevant for 2 μm thulium-doped fiber lasers with common pump bands highlighted in red; *right*: Main ion-ion energy transfer processes: CR is the cross-relaxation, ETU is the energy transfer up-conversion and EM is the energy migration.

energy or remote sensing [15, 16], processing of plastics and exotic materials [17, 18] and pumping mid-IR sources [19, 20].

Figure 2.4 details the electronic transition in Tm^{3+}-doped silica that are most relevant when used as a 2 μm source. The ${}^3F_4 \rightarrow {}^3H_6$ emission band is one of the broadest for a rare-earth ion doped in silica, extending from $\sim$1600 nm to $\sim$2200 nm. These lasers can be either pumped at around 790 nm, 1.2 μm, or at 1.65 μm. The 2 μm laser emission ends in the upper Stark level of the ground state and it has therefore to be considered as quasi-three-level laser system with a thermally populated ground state [21]. The 790 nm is the most attractive wavelength pump due to the commercially available AlGaAs pump diodes. For high power configurations, pumping with 790 nm and extracting at 2 μm generates a large value of quantum defect ($\sim$60%)[1].

[1]In the scientific laser community, the term "quantum defect" refers to the fact that

Fortunately, the cross-relaxation process (CR) can provide two excited-state electrons for one pump photon [22]. CR (also sometimes called self-quenching) occurs between two identical molecules (or ions). When a first molecule (or ion), initially in an excited state, exchanges energy with a second molecule (ion), that is initially in the ground state, both molecules (ions) change simultaneously to another excited state that is intermediate in energy between the two initial states. The drop in energy for the first molecule (ion) is equal to the increase in energy for the second molecule (ion), thereby conserving energy in the cross-relaxation. In a common example of cross-relaxation the intermediate states for the two molecules (ions) have the same energy and are energetically halfway between the initial excited state of the first molecule (ion) and the ground state of the second molecule (ion). High power thulium-doped fiber lasers rely on the CR process and have thus improved overall efficiencies beyond 40% [7].

Several ion-ion energy transfer processes are possible in Tm^{3+}-doped silica, and are depicted in Figure 2.4. CR is beneficial because it populates the upper laser level $^3F_4$. Energy transfer up-conversion (ETU) is a physical process that involves the excitation of a laser-active ion to a level above that which would be achieved by simple absorption of a pump photon, the required additional energy being transferred from another laser-active ion undergoing non-radiative disexcitation. In contrast to CR, ETU is unwanted because it quenches the $^3F_4$ level. CR1 ($^3H_4$, $^3H_6 \rightarrow {}^3F_4$, $^3F_4$) is the dominant energy transfer process, while CR2 ($^3H_4$, $^3H_6 \rightarrow {}^3H_5$, $^3F_4$) is negligible because it requires multi-phonon assistance [23]. ETU1 ($^3F_4$, $^3F_4 \rightarrow {}^3H_6$, $^3H_5$) and ETU2 ($^3F_4$, $^3F_4 \rightarrow {}^3H_6$, $^3H_4$) also requires multi-phonon assistance and they are weaker than CR1 [24], but still important processes because they reduce the CR efficiency. ETU2 has been observed in highly-doped (2900 ppm of Tm_2O_3) Tm^{3+}-doped silica fibers [25].

the energy of a pump photon is in general higher than that of a signal photon. As a consequence, the power efficiency of the laser could not be 100% even if every pump photon could be converted into a laser photon [11].

Energy migration (EM) is a resonant process that re-distributes ion excitations between $^3H_4$ and $^3H_6$. EM was found to have a substantial role in Tm^{3+}-doped fluoroindogallate glasses [26], and it could be assisting the CR process for silica-based thulium-doped fiber lasers.

Cross-relaxation is strictly correlated with ion-ion separation, and thus to dopant concentration [27]. The high dopant concentration can lead to unwanted effect of clustering. This is the tendency of laser-active ions in a solid-state gain medium to form clusters rather than to be randomly spread. This is normally an undesirable effect, as it allows for energy transfer between laser ions which can seriously degrade the gain and power efficiency. To reduce unwanted clustering at high Tm^{3+} concentrations, Al^{3+} is co-doped to increase the solubility [28]. This modifies the Tm^{3+} ion's local environment and reduces the local maximum phonon energy [29]. It was found that Al^{3+}:Tm^{3+} ratios >10:1 are ideal to prevent concentration quenching [30]. According to these studies, fibers with ∼4.0 wt.% Tm^{3+} and high Al^{3+} co-doping are typical designs to improve thulium-doped fiber laser efficiencies beyond 40%. Thus, doping concentrations >2.0 wt.% are necessary to enable CR and exceed ∼40% efficiencies; however, increasing the Tm^{3+} concentration over 3.5 wt.% appears to have no further benefit [7].

Thulium-doped fiber lasers pumped at 790 nm exhibit blue fluorescence, originating from the $^1G_4$ level [31]. In general, this up-conversion needs to be minimized to prevent photodarkening and improve the overall 2-μm emission [32, 33, 34]. Two possible processes can cause this transition. As shown in Figure 2.4, excited state absorption from the $^3H_5$ level by 790 nm is allowed, but the $^3H_5$ level is poorly populated due to the fast non-radiative decay. The second possible process was described in [35], and involves ETU via ($^3H_4$, $^3H_4 \rightarrow {}^3F_4$, $^1G_4$), requiring multi-phonon assistance.

2.1.3 Q-switching

Q-switching is one of the most common laser techniques to produce short pulses. The name originates from the Q-factor of an optical resonator, which depends on the cavity losses. During this operating condition, the laser pumping process is prolonged to build up a much larger population inversion inside the active medium than usual, by removing the feedback or highly increasing the cavity losses. Then, after a large inversion has been developed, the factor Q of the cavity is "switched" back to its usual large value. The result is a short, intense pulse of laser output which dumps all the accumulated population inversion in a single short laser pulse, typically of a few tens of nanoseconds.

Different methods are employed to modulate the Q-factor of the laser cavity and can be separated into **passive** and **active** methods regarding the mechanism how the resonator losses are induced.

With passive modulators some form of saturable absorbing medium inside the laser cavity is used. The laser inversion is built up by the pumping process until the gain inside the cavity exceeds the saturation absorption level, and laser oscillation begins to develop inside the cavity. This oscillation then saturates the absorber and thus opens up the cavity, leading to the development of a rapid and intense oscillation pulse. Passive Q-switching is in general simple, however, the Q-switching repetition rate is adjusted by the cavity parameters and not stable with pump power and exhibits low damage thresholds.

Active devices can be either electro-optic and acousto-optic modulators (EOM and AOM). Their damage threshold is higher than passive modulators [36]. An EOM consists in general of an electro-optic crystal which becomes birefringent under the influence of an applied electrical voltage. Frequently used nonlinear crystal materials for EOMs are potassium dideuterium phosphate (KD*P = DKDP), potassium titanyl phosphate (KTP), beta-barium borate (BBO) (the latter for higher average powers and/or

higher switching frequencies), also lithium niobate ($LiNbO_3$), lithium tantalate ($LiTaO_3$) and ammonium dihydrogen phosphate ($NH_4H_2PO_4$, ADP) [37]. EOM for Q-switching provides the fastest form of pulses ($\leq$ 10 ns), with precise timing, good stability and repeatability. This approach requires both a fairly expensive electro-optic crystal and a very fast-rising high-voltage pulse source (at least several kV in a few tens of nanoseconds).
AOMs are based on the acousto-optic effect. Figure 2.5 shows the operation sketch of a typical AOM for Q-switching: a piezoelectric transducer transforms the electric signal into a sound wave, the incident light is then deflected from its direction by the induced diffraction grating traversing the modulator. A sound wave absorber on the other side of the crystal prevents any back reflection, which could prevent from any back reflection and thus the establishment of the standing wave inside the modulator. An orientation of the transmitted light under the Bragg angle θ_B is required for reaching highest diffraction efficiencies, which can be $\geq$ 90%. These modulators exhibit relatively longer build-up times compared to EOMs due to the low propagation speed of the sound wave inside the crystal. For this reason they are limited up to ∼400 kHz [38]. The material of such AOMs is usually fused silica (SiO_2) or tellurium dioxide (TeO_2). Fused silica has the highest laser-induced damage threshold, on the other hand, tellurium dioxide exhibits high optical homogeneity, low light absorption and scattering, and a transmission ranging from 330 nm to 5 μm [36]. Because of their availability in the laboratory, only TeO_2 AOMs are used in this thesis.

2.1.4 Mode-locking

Mode-locking is a method to obtain ultrashort pulses from lasers. In this context, the laser resonator contains a mode locking device, either an active or a passive element, which causes the formation of an ultrashort pulse circulating in the laser resonator. As already mentioned in Section 2.1.1, a laser can oscillate on many longitudinal modes, with frequencies that are equally

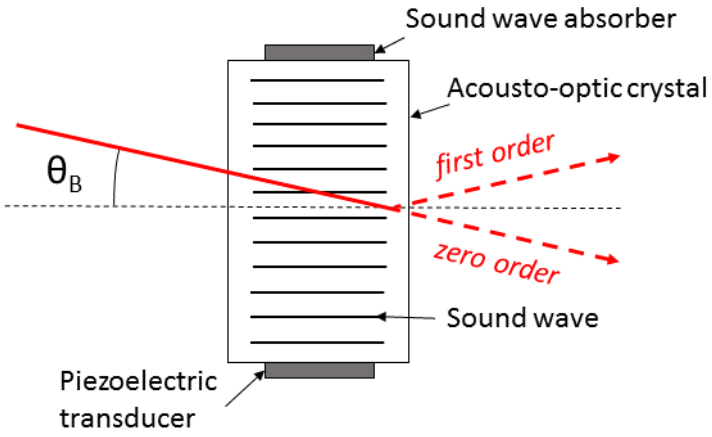

Figure 2.5: Sketch of an AOM for Q-switching operation. The sound wave propagates along the crystal inducing the diffraction of the incident beam.

separated by the intermodal frequency spacing $\Delta\nu$ = c/2L. If these modes oscillate in an optical resonator, each mode builds up a standing wave inside the cavity with a defined phase. During mode-locking, the phases of these longitudinal modes are forced to be equal, which results in a circulating pulse inside the cavity with the group velocity of the center frequency of its spectral bandwidth $\Delta\nu$. If each of the laser modes is approximated by a uniform plane wave propagating in the longitudinal mode z, with a velocity $c_n = c/n$, one can write the total complex wavefunction of the field in the form of a sum:

$$U(z,t) = \sum_q A_q \ \exp\left[j2\pi\nu_q\left(t - \frac{z}{c_n}\right)\right], \tag{2.4}$$

where:

$$\nu_q = \nu_o + q\Delta\nu \qquad\qquad q = 0, \pm1, \pm2, ... \tag{2.5}$$

is the frequency of mode q, and A_q is its complex envelope. For convenience it is assumed that the $q = 0$ mode corresponds with the central frequency ν_o. The amplitude of A_q may be determined from the knowledge of the spectral

profile of the gain and resonator loss. Since the modes interact with different groups of ions in an inhomogeneously broadened medium, their phases are random and statistically independent. Substituting (2.5) into (2.4) provides:

$$U(z,t) = \mathcal{A}\left(t - \frac{z}{c_n}\right)\exp\left[j2\pi\nu_o\left(t - \frac{z}{c_n}\right)\right], \tag{2.6}$$

where the complex envelope $\mathcal{A}(t)$ is the function:

$$\mathcal{A}(t) = \sum_q A_q \ \exp\left(\frac{jq2\pi t}{\tau_{rp}}\right). \tag{2.7}$$

The complex envelope $\mathcal{A}(t)$ in (2.7) is a periodic function of the round-trip time τ_{rp}, and $\mathcal{A}(t - z/c)$ is a periodic function of z of period $c\tau_{rp} = 2L$. If the magnitudes and phases of the complex coefficients A_q are properly chosen, $\mathcal{A}(t)$ may be made to take the form of periodic narrow pulses. If one considers M modes ($q = 0, \pm1, ..., \pm S$, so that $M = 2S + 1$), whose complex coefficients are all equal, $A_q = A$, $q = 0, \pm1, ..., \pm S$. Then:

$$\mathcal{A}(t) = A\sum_{q=-S}^{S}\exp\left(\frac{jq2\pi t}{\tau_{rp}}\right) = A\sum_{q=-S}^{S}x^q = A\frac{x^{S+1} - x^{-S}}{x-1} = A\frac{x^{S+1/2} - x^{-S-1/2}}{x^{1/2} - x^{-1/2}}, \tag{2.8}$$

where $x = \exp(j2\pi t/\tau_{rp})$. After few algebraic manipulations, $\mathcal{A}(t)$ can be cast in the form:

$$\mathcal{A}(t) = A\frac{\sin(M\pi t/\tau_{rp})}{\sin(\pi t/\tau_{rp})}. \tag{2.9}$$

The optical intensity is then given by $I(t,z) = |\mathcal{A}(t - z/c)|^2$ or

$$I(t,z) = |A|^2\,\frac{\sin^2[M\pi(t - z/c_n)/\tau_{rp}]}{\sin^2[\pi(t - z/c_n)/\tau_{rp}]}. \tag{2.10}$$

As illustrated in Figure 2.6, this is a periodic function of time. On the one hand, the shape of the mode-locked pulse train is therefore dependent on the number of modes M, which is proportional to the laser gain bandwidth. On the other hand, the pulse width τ_{ML} is inversely proportional to this

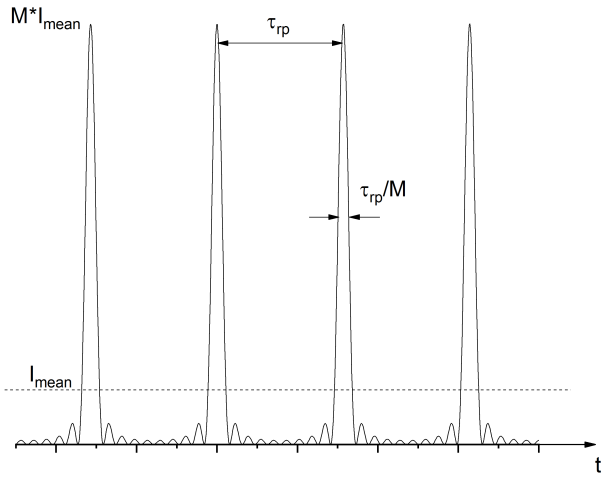

Figure 2.6: Intensity of the periodic pulse train resulting from the sum of $M = 10$ laser modes of equal magnitudes and phases. Each pulse has a width that is M times smaller than the round-trip time τ_{rp} and a peak intensity that is M times greater than the mean intensity.

bandwidth. Since the laser gain bandwidth can be quite large, very short mode-locked laser pulses can be generated. The ratio between the peak and mean intensities is equal to the number of modes M, which can be also quite large.

As in the case of Q-switching, two possible kinds of elements can be used to produce ultrashort pulses: **passive** or **active**.

Passive mode locking provides in general the shortest laser pulses [39]. Passive mode-locking is based on non-linear effects, which cause intensity-dependent losses of the cavity. For instance, the Kerr effect can be used. The general principle behind Kerr-Lens mode-locking is sketched in Figure 2.7. The Kerr effect (also known as quadratic electro-optic effect) is a phenomenon observed in non-linear optical materials where the refractive index of the material changes in response to an electric field. This effect is observed in all materials; however, it is more prominent in certain liquids. A pulse that builds up in a laser cavity containing a gain medium and a Kerr medium

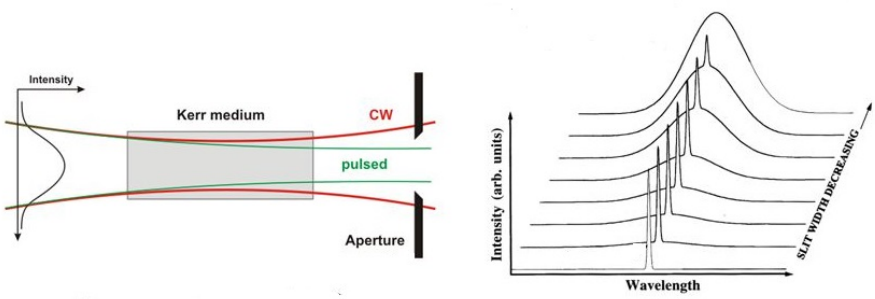

Figure 2.7: Self focusing of a high intensity beam inside a Kerr medium. The aperture at the output strips off the wings of the pulse leading to a shortening of the pulse. Image adopted from [21].

experiences self focusing, that is non-linear lensing of the laser beam due to the non-linear refractive index of the Kerr medium. A laser pulse propagating through the Kerr medium has a time dependent mode size as higher intensities undergo stronger focusing. If a hard aperture is placed at the right position in the cavity, it strips off the wings of the pulse, leading to a shortening of the pulse. Instead of a separate Kerr medium and a hard aperture, the gain medium can act both as a Kerr medium and as a soft aperture. Commercially available laser systems providing the shortest laser pulses are based on Kerr lens mode-locking. It has become a state-of-the-art as mode-locking mechanism, but only for crystal systems. A mechanism of Kerr-lens mode locking in ber laser has been proposed [40]. It could be realized in active photonic-crystal bers with nite number of the air holes hexagonally arranged around the core with refractive index larger than refractive index of the glass matrix.

Another passive technique for mode-locking uses saturable absorbers. If the laser is running in continuous wave operation, there are random peaks in the temporal intensity profile of the laser that are more amplified, compared

to the background due to the saturation of the absorber. Once this saturation level is reached by the highest intracavity peak, it gets further amplified when passes the absorbers at each round trip. Mode-locking operation is then initiated [39]. Many materials have been successfully used as saturable absorber, e.g. semiconductor saturable absorber mirrors (SESAMs) [41], carbon nanotubes [42] or graphene [43].

Concerning active mode-locking, it usually achieved by using modulators driven by an external signal. This technique is called Amplitude Modulation mode-locking (AM mode-locking) and it is usually performed with an acousto-optic modulator. These devices are different from the modulators employed for Q-switching lasers, because they operate at resonance. The modulator material, such as a quartz block, has parallel faces and the sound wave is reflected back and forth in the material. The length of the quartz cell is cut such that the length is equal to an integer number of the half-wavelength of the sound wave. In such standing-wave pattern, the diffraction loss of the optical beam will be modulated at twice the frequency of the sound wave since the diffraction loss reaches a maximum wherever the standing-wave pattern has a maximum. The AOM has consequently an acoustic free spectral range, $\Delta\nu_{AOM}$. Therefore, during active mode-locking, the external radio frequency drive signal for the AOM has to be synchronized with the resonance described by $\Delta\nu_{AOM}$ and the free spectral range of the laser, $\Delta\nu$. This can be achieved by changing either the cooling temperature of the AOM, and therefore the length of the acousto-optic material, or the optical length of the cavity by mounting one of the resonator mirrors on a translation stage for cavity length adjustment. The propagation mode gets thus frequency-shifted sidebands, which are exactly spaced by $\Delta\nu$ from its wavelength. After certain number of round-trips, more and more phase-locked longitudinal modes build up [21]. More details are given in Section 4.4.3.

Finally, to compare active and passive modulation techniques, it can be generally stated that passive mode-locking systems provide shorter pulses

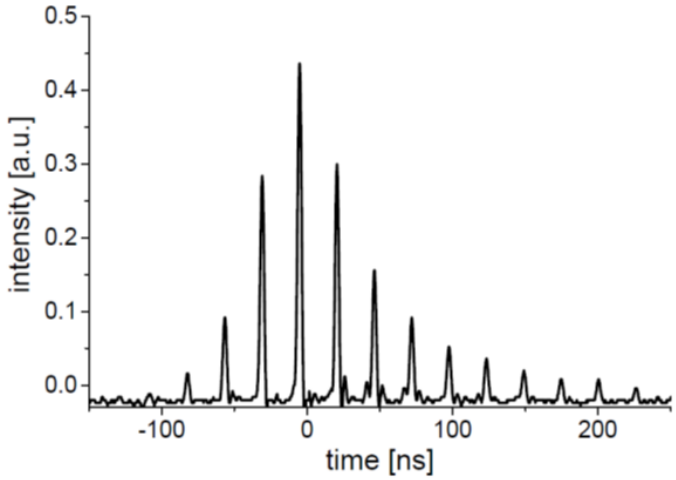

Figure 2.8: Example of a Q-switched mode-locking pulse train. The measurement has been performed at ISL with a slow photodiode, so the image is not resolved in time.

and higher compactness. However, the output power and pulse energy are limited up to a low level in terms of stability and damage threshold of the available passive modulators [44]. On the other hand, active modulation provides high optical damage thresholds, enabling the realization of systems without amplifier chains. For this reason, active modulation has been chosen for the pump laser source in this thesis work.

2.1.5 Q-switched mode-locking

Q-switched mode-locking (QML) is a different kind of pulse generation technique, where the mode-locked pulse train is additionally modulated by a Q-switching repetition rate. A typical QML pulse train is shown in Figure 2.8. In this operation, the peak power and the pulse energy levels of the mode-locked sub-pulses below the Q-switching envelope are orders of magnitude higher compared to single mode-locked systems. There are different approaches to establish Q-switched mode-locked pulses in a laser cavity us-

ing either active or passive modulators. Various results are obtained in terms of output stability, ease of implementation, compactness of the system and output power characteristics.

When a laser is purely mode-locked by a saturable absorber as a passive modulator, Q-switch instabilities can occur for certain cavity and modulator parameters. In this case, the laser will be Q-switched mode-locked with a Q-switch repetition rate that is approximately the same as the relaxation oscillation of the laser system [45]. The disadvantages of this approach are instabilities in terms of timing and pulse energy jitter [46, 47], fluctuations due to the inability of tuning the Q-switch repetition rate [47] and low damage thresholds caused by the use of passive modulators. A way to control the Q-switch repetition rate is to add an active modulator to the system [47], the output stability increases because of the external trigger of the modulator. However, passive mode-locker modulators need a certain build-up time from noise, therefore, the Q-switch repetition rate is limited dependent on the used passive modulator. This will increase the complexity of the system.

It is possible to obtain a Q-switched mode-locked system by simply using a single active Q-switch modulator. The necessary mode-locked modulation is provided by the modulator working with a radio-frequency that is exactly the free spectral range of the laser resonator $\Delta\nu$, which generates a slight frequency shift of the intracavity radiation [48]. This approach is the best in terms of compactness and ease of implementation, however is not practically convenient for fiber lasers, because the cavity length has to be always adapted and optimized.

A rare approach used in literature is the implementation of an active mode-locker and a passive Q-switch modulator in the system [49, 50]. With this approach it is evidently not possible to modulate the Q-switch repetition rate and the setup suffers from the low damage threshold and instabilities connected to the use of a passive modulator for Q-switching.

The last technique to stimulate Q-switched mode-locked pulses is to use active modulators for both pulse generation methods. This is the approach that I chose for the fiber laser reported in this thesis. High average power and high energy output pulses can be obtained owing to the high damage threshold of the active modulators. In actively Q-switching and actively mode-locked laser systems, the build-up time of the Q-switch envelope is not different compared to purely Q-switching systems, thus the pulse width for Q-switching in Q-switched mode-locked operation is approximately the same [47]. This kind of Q-switched mode-locked approach is more compact compared to purely mode-locked systems successively amplified by a chain by different optical stages and expensive pump diodes.

2.2 State of the art high power thulium-doped fiber lasers

2.2.1 Continuous-wave systems

As already mentioned in Section 2.1.2 and shown in Figure 2.9, there are different absorption bands available to excite the thulium ions. However only a few of them are of interest for high power systems. Pumping with wavelengths shorter than 790 nm limits the conversion efficiency to under 35% because of the quantum defect [7]. Pumping into the $^3H_5$ level with 1210 nm sources could theoretically reach 50-60% efficiencies, but is not suitable due to a lack of high power pump sources. Another approach to generate high power thulium-doped fiber lasers is to pump directly into the upper laser level ($^3F_4$). This approach provides access to a large bandwidth with reduced quantum defects compared to 790 nm pumping, and avoids issues with cross-relaxation. Unfortunately, there are no high power/brightness sources available in the 1550-1910 nm spectral range [51]. As a result, thulium-doped fiber lasers with $>$ 100 W output powers are pumped at 790 nm due to the availability of high power/brightness pump diodes. Continuous wave high power 790 nm

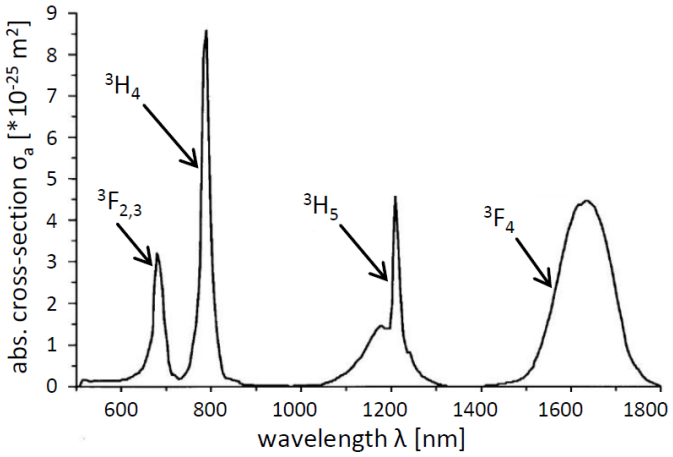

Figure 2.9: Absorption cross-section of Tm^{3+}-doped silica (image adopted from [52]).

pumped thulium-doped fibers emerged over a decade ago with an 85 W, free-space pumped oscillator in 2005 by Frith *et al.* [53]. By 2009, in the work Moulton *et al.*, the level of the output power increased to 300 W with a slope efficiency of 62% [54]. Also in 2009, a 608 W single-frequency system with < 5 MHz linewidth and $M^2 < 1.06$ was demonstrated by Frith *et al.* [32]. Shortly thereafter in 2010, over 1 kW was generated in an all-fiber, two-stage power amplifier with 53.2 % slope efficiency by Ehrenreich *et al.* [55]. This demonstration remains the highest reported power from a 2 μm fiber laser. The highest reported thulium-doped fiber laser single oscillator in all-fiber format produced 567 W at 1970 nm in the work of Walbaum *et al.* [56]. The main limitation for this type of configuration is dopant diffusion when splicing the active and passive fibers leading to excessive scattering losses at the interface due to mode-mismatch. Therefore, optimizing splice parameters is critical for current high power single-mode thulium-doped fiber lasers together with the thermal management of the entire system [57].

2.2.2 Pulsed systems

Thulium-doped fiber lasers in **Q-switching** have been investigated with active modulators. El Sharif *et al.* demonstrated a pulse energy of around 900 μJ with a pulse duration of 150 ns providing a peak power of 4 kW [58]. However, the output power level of this experiment has been below 1 W. A peak power of 9 kW has been demonstrated with a pulse energy of 435 μJ and a pulse width of 49 ns by Kadwani *et al.* [59]. The average output power level of this experiment was around 10 W. Eichhorn reported a diode-pumped Q-switched thulium doped double-clad silica fiber laser; the output power was 30 W at a pulse width of 41 ns and a pulse repetition rate in the range of 10-125 kHz [60]. Stutzki *et al.* also demonstrated a 2.4 mJ, 33 W (at 13.9 kHz pulse repetition rate) actively Q-switched thulium fiber laser; the pulse width was 15 ns, corresponding to a peak power of more than 150 kW [61]. This remains the highest peak power level for a single Q-switched thulium fiber laser.

Up to now, there are no reports about **actively mode-locked** thulium-doped fiber lasers using acousto-optic modulators. Only an EOM has once been used to provide 38 ps for fundamental mode-locking. The fiber laser delivered output power levels in the milliwatt range [62].

Other techniques for generating short pulses in thulium-doped fiber lasers have been investigated. To generate nanosecond pulses **gain-switching** is another effective approach. Some researches about gain-switched thulium doped fiber lasers have been reported, but up to now the output power levels are limited to a few tens of Watt [63, 64, 65, 66].

Another approach consists of using a seed laser providing short pulses and then use a chain of fiber amplifiers to increase the energy. Liu *et al.* achieved an average power of 120.4 W, 16 ps pulsed thulium-doped fiber amplifier. This all-fiber oscillator was mode-locked by a SESAM with a high pulse repetition rate of 333.7 MHz by a short linear cavity to reduce the non-linearity in the power amplifiers [67]. Stutzki *et al.* at Jena University

demonstrated a high power thulium-doped fiber chirped-pulse amplification system with an average output power of 152 W and pulse peak power of 4 MW. The high-compression efficiency has been achieved by using multilayer dielectric gratings with diffraction efficiencies higher than 98% [68]. Recently, Ouyang *et al.* demonstrated a stable all-fiber actively Q-switched thulium doped fiber laser in a MOPA configuration. The seed laser was actively Q-switched by a fiber-coupled AOM, and the output pulse width could be tuned from 1.6 μs to 46.3 ns with an increased pulse repetition rate from 1 kHz to 2 MHz. Then, the milliwatt level laser output power is scaled to over 110 W by a three-stage thulium-doped MOPA system [69]. In 2019, 1060 W average power from an ultrafast thulium-doped fiber chirped pulse amplification system has been reported [70]. The pulse energy of 13.2 μJ with a pulse duration of 265 fs at an 80 MHz pulse repetition rate resulted in a peak power of 50 MW spectrally centered at 1960 nm. This system represents a new average power record for thulium-doped fiber lasers with diffraction-limited beam quality.

Chapter 3

Supercontinuum generation in optical fibers

This chapter is dedicated to the theoretical background of optical fibers and a qualitative explanation of supercontinuum generation in optical fibers. An overview of the basic fiber characteristics, the pulse propagation mechanisms inside fibers and the main non-linear effects stimulating the wavelength broadening is given. At the end of the chapter, an overview of the main materials for mid-IR supercontinuum generation is presented together with an analysis of the state of the art in the scientific literature.

3.1 Fiber geometry

Optical fiber is an important class of optical waveguide with radial symmetry which can guide light over long distances. Due to their strong wave-guiding properties, optical fibers are a flexible delivery tool for laser light in the field of material processing, medical engineering [71] or fast communication over huge distances in the telecommunication area [72]. From the visible to the mid-IR, the waveguide materials are commonly dielectric media (glasses).

The simplest form is a step-index fiber and consists of a core with refractive index n_{core}, surrounded by a cladding layer with refractive index

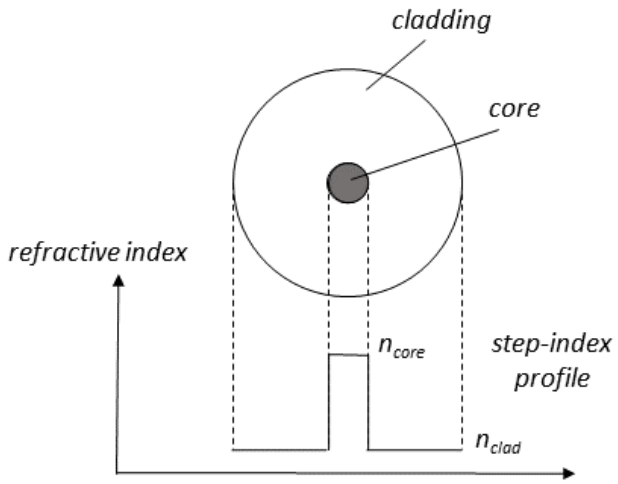

Figure 3.1: Cross-section of a step-index fiber and its radial refractive index profile (*not-true-to-scale*).

n_{clad}, with $n_{core} > n_{clad}$. Usually, a polymer coating is added around the cladding to protect the fiber from external damaging and to increase its robustness. This kind of fiber is called step-index. In Figure 3.1, the cross section of a step-index fiber is shown: the refractive index profile shows the sharp change between n_{core} and n_{clad}. A variation of the refractive index can be obtained by doping the glass material. In fused silica glass (SiO_2), the core is doped with germania (GeO_2) resulting in an increase of the refractive index value, otherwise the refractive index of the cladding can be decreased adding fluorine (F) as dopant [73]. The mechanism of light transportation of step-index fibers can be described by the total internal reflection (TIR) effect. This phenomenon refers to the complete reflection of a ray of light within an optical medium from the surrounding surfaces. Figure 3.2 describes the phenomenon using the simple geometrical ray optics approach, which is valid for fibers whose core size a is much larger than the wavelength of the light λ ($\lambda \ll a$). However, the concept of ray optics is not fully appropriate for describing the propagation details of light in optical fibers when wave aspects are important, in particular for fibers with a small core. The difference in

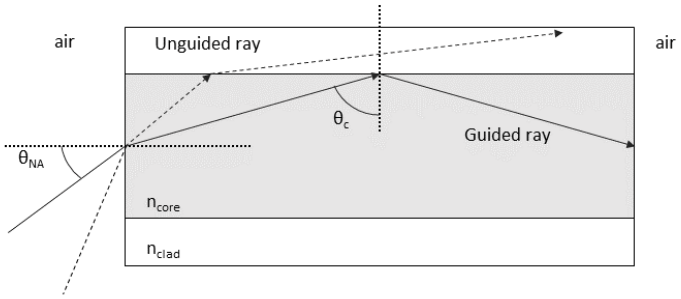

Figure 3.2: Total internal reflection (TIR) mechanism. An incoming ray is reflected into the core only when its incident angle is equal or smaller than the largest acceptance angle θ_{NA} (solid line).

the core and cladding refractive indices defines an acceptance cone and a maximum angle of a ray (against the fiber axis) hitting the fiber core which allows the incident light to be trapped by the core via TIR. The sine of the half-angle (θ_{NA}) of this cone defines the numerical aperture (NA) as:

$$NA = \sin(\theta_{NA}) = \sqrt{n_{core}^2 - n_{clad}^2}. \tag{3.1}$$

If the angle of an incident ray at the fiber entrance gets larger than θ_{NA} the transmitted ray in the fiber is not reflected totally at the core-cladding interface and it is partially transmitted into the cladding.

3.2 Wave equation

For fibers whose core diameter becomes comparable to the wavelength, in order to describe the propagation phenomena, the simple ray picture of geometrical optics has to be replaced. The light propagation in optical fibers can be derived from the Maxwell's equations, which form the theoretical basis for describing classical electromagnetism:

$$\vec{\nabla} \cdot \mathbf{D} = \rho_e, \tag{3.2}$$

$$\vec{\nabla} \cdot \mathbf{B} = 0, \tag{3.3}$$

$$\vec{\nabla} \times \mathbf{E} = -\frac{\partial \mathbf{B}}{\partial t}, \tag{3.4}$$

$$\vec{\nabla} \times \mathbf{H} = j + \frac{\partial \mathbf{D}}{\partial t}. \tag{3.5}$$

Here, $\vec{\nabla}\cdot$ is the divergence and $\vec{\nabla}\times$ the curl operator. $\mathbf{D}$ is the electric displacement field and ρ_e the electric charge density. $\mathbf{B}$ and $\mathbf{E}$ are the magnetic induction and electric fields, respectively, $\mathbf{H}$ the magnetic field strength and j the electric current density. In the absence of free charges in a medium such as optical fibers, $j = 0$ and $\rho_e = 0$. $\mathbf{B}$ depends on $\mathbf{H}$:

$$\mathbf{B} = \mu_0(\mathbf{H} + \mathbf{M}) \tag{3.6}$$

and $\mathbf{D}$ on $\mathbf{E}$:

$$D(r,t) = \varepsilon_0 \mathbf{E} + \mathbf{P}, \tag{3.7}$$

where μ_0 is the free-space permeability, $\mathbf{M}$ the magnetization of the material, ε_0 is the vacuum permittivity and $\mathbf{P}$ the material polarization. At low light intensities the electric polarization is proportional to the electric field strength, whereas non-linear contributions become important at high optical intensities. In this case, the polarization can be expressed as sum of a linear part, P_l, and a non-linear part, P_{nl}:

$$\mathbf{P} = \mathbf{P}_l + \mathbf{P}_{nl} = \varepsilon_0 \cdot \chi^{(1)}\mathbf{E} + \varepsilon_0 \sum_{j>1} \chi^{(j)}\mathbf{E}^j, \tag{3.8}$$

where $\chi^{(j)}$ is the j^{th} order component of the material's magnetic susceptibility tensor, which is defined by the composition and molecular structure of the material. If weak electro-magnetic fields are interacting with the material, P_l can be taken as an accurate approximation, but if the field is strong, higher-order susceptibilities have to be taken into account, which are responsible for different effects: $\chi^{(2)}$ linked to second harmonic generation, sum or difference frequency generation; $\chi^{(3)}$ is related to the Kerr effect, four wave mixing,

or different scattering processes, which will be discussed in the following sections.

To calculate the propagation of the electro-magnetic field in the core of an optical fiber, Equation (3.6) is inserted in Equation (3.4), taking into account the fact that glass is not magnetizable and therefore $\mathbf{M} = 0$:

$$\vec{\nabla} \times \vec{\nabla} \times \mathbf{E} = -\mu_0(\vec{\nabla} \times \frac{\partial \mathbf{H}}{\partial t}). \tag{3.9}$$

By using Equation (3.5), Equation (3.9) and the two following relations:

$$\vec{\nabla} \times \vec{\nabla} \times \mathbf{E} = \vec{\nabla} \cdot (\vec{\nabla} \cdot \mathbf{E}) - \vec{\nabla}^2 \mathbf{E}, \tag{3.10}$$

$$\vec{\nabla} \cdot (\vec{\nabla} \cdot \mathbf{E}) = 0, \tag{3.11}$$

the general wave equation yields a non-linear differential equation:

$$\vec{\nabla}^2 \mathbf{E} = \frac{1}{c^2} \frac{\partial^2 \mathbf{E}}{\partial t^2} + \mu_0 \frac{\partial^2 \mathbf{P}}{\partial t^2}, \tag{3.12}$$

where $c = \frac{1}{\sqrt{\mu_0 \varepsilon_0}}$ is the speed of an electro-magnetic wave in vacuum. The notation x, y, z will indicate the position inside the fiber expressed in the Cartesian coordinate system where the z axis is the propagation direction as shown in Figure 3.3, t the time and ω the angular frequency of the propagating wave, which is:

$$\omega = 2\pi\nu, \tag{3.13}$$

with ν the frequency of the radiation. Equation (3.12) can be solved with some simplifying assumptions. A common approach takes into account the non-linear part of the polarization $\mathbf{P}_{nl}$ as a perturbation of the solution for the linear case (where $\mathbf{P}_{nl} = 0$). Furthermore, $\mathbf{E}$ is assumed to be a quasi-monochromatic signal. This means that $\mathbf{E}$ can be expressed as:

$$\mathbf{E} = \frac{1}{2} \left[E(x, y, t) \exp(-j\omega t) + E^*(x, y, t) \exp(j\omega t) \right], \tag{3.14}$$

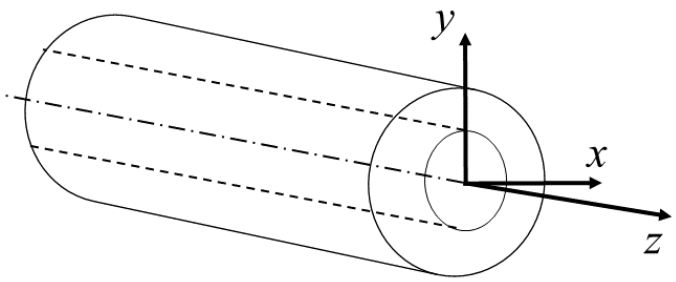

Figure 3.3: Schematic drawing of the optical fiber where x and y are the transversal directions and z is the propagation axis of the electromagnetic wave.

where $E(x, y, t)$ is a slowly-varying complex envelope (compared to the frequency of oscillation ω). Under these conditions, the method of the separation of the variables can be used to solve the Equation (3.12). According to this method, the generic solution can be expressed in the form:

$$E(x, y, z, t) = E_0 \Psi(x, y) A(z, t) e^{i(\beta z - \omega t)}, \tag{3.15}$$

with β as the mode-propagation constant, which will be further described in the following section. $\Psi(x, y)$ represents the transverse modal distribution and $A(z, t)e^{i(\beta z - \omega t)}$ the longitudinal part of the propagating electro-magnetic wave.

3.3 Fiber modes

Regarding the solution of the general wave equation (Equation 3.15), the $\Psi(x, y)$ are the transverse propagation modes. These modes can be found by solving the scalar wave equation in cylindrical coordinates. Since these calculations are rather complicated, Gloge proposed a solution for weakly guiding fibers in which the difference of the refractive index of the cladding

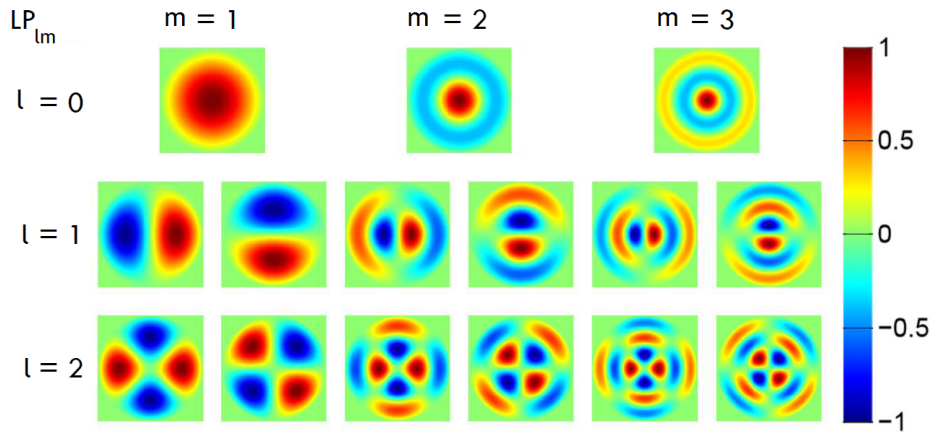

Figure 3.4: Examples of transverse modes LP_{lm} for $l = 0$, 1, 2 and m between 1 and 3. Image adopted from [74].

n_{clad} and the core n_{core} is small [75]. This situation applies for most fibers and can be expressed via:

$$\Delta = \frac{n_{core} - n_{clad}}{n_{clad}} \ll 1. \tag{3.16}$$

Under the assumption of an infinitely extended cladding, expressions for linearly polarized (LP) modes can be derived whose field components into the propagation direction z are negligible small. The electrical transverse field amplitudes in core and cladding in a fiber with the core diameter a then are:

$$E_{core} = E_l \frac{J_l(ur/a)}{J_l(u)} \cos(l\Phi) \quad (0 < r < a), \tag{3.17}$$

$$E_{clad} = E_l \frac{K_l(wr/a)}{K_l(w)} \cos(l\Phi) \quad (a < r < +\infty), \tag{3.18}$$

where J_l is the Bessel function of first kind of order l, K_l is the modified Bessel function of second kind of order l and E_l is the transverse electric field at the core/cladding interface. The parameters u and w are defined as:

$$w = a\sqrt{\beta^2 - n_{iclad}^2 k_0^2}, \tag{3.19}$$

$$u = a\sqrt{n_{core}^2 k_0^2 - \beta^2}. \tag{3.20}$$

The wavenumber k_0 is defined as:

$$k_0 = \frac{2\pi}{\lambda}. \tag{3.21}$$

The different LP modes are identified via two indices l and m. Here l determines the number of angular minima of the dielectric field amplitude divided by two and m the number of minima in radial direction minus one. From the parameters of the fiber and the light wavelength, it is possible to calculate the normalized frequency V which determines the modes that can propagate in the fiber core:

$$V = \frac{2\pi a NA}{\lambda}. \tag{3.22}$$

It can be shown that the cut-off frequency of the LP_{01} mode has a value $V = 0$. Hence it is theoretically always guided and it is called fundamental mode. The mode that is guided next is the LP_{11} for values $V > 2.405$. In Figure 3.4 the different transverse modes that can propagate in an optical fiber are shown.

Single-mode fibers (also called monomode fibers) are optical fibers which are designed such that they support only a single propagation mode for a given wavelength. Higher-order modes do not exist. Single-mode fibers usually have a relatively small core, with a diameter of only a few micrometers, and a small refractive index difference between core and cladding. For single-mode propagation (LP_{01}), the transverse modal profile is a Bessel function of first kind and 0^{th} order inside the fiber core [76]. As it can be seen in Figure 3.5 the transverse intensity profile of the fundamental mode can be well approximated by the Gaussian distribution:

$$I_{Gauss}(r) = \frac{2P_0}{\pi(\frac{MFD}{2})^2} e^{-\frac{2r^2}{(\frac{MFD}{2})^2}}, \tag{3.23}$$

where P_0 is the total power of the mode, MFD is the mode field diameter and r the radial position in the cylindrical coordinate system. As already stated,

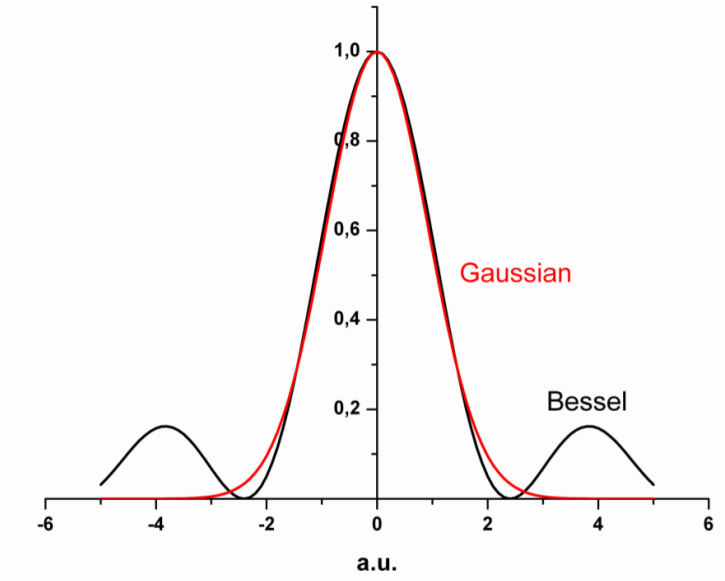

Figure 3.5: Comparison of the fundamental mode of a fiber and a Gaussian function.

for single mode operation, the normalized frequency V has to be < 2.405. A good approximation for the *MFD* has been empirically determined by [77]:

$$MFD \approx 2a(0.65 + 1.619V^{-1.5} + 2.879V^{-6}). \tag{3.24}$$

In contrast to single-mode fibers, multimode fibers are optical fibers which support multiple transverse guided modes for a given optical frequency and polarization. Compared with standard single-mode fibers, multimode fibers usually have significantly larger core areas, but also generally a higher numerical aperture.

The normalized *MFD* is plotted versus the normalized frequency V in Figure 3.6. It can be observed that for V values smaller than 1.5 the *MFD* spreads out into the cladding, and the losses of the fundamental mode increase. A tighter mode confinement in the core is reached for higher values of the V-parameter. If the fiber is highly multi-mode, the total number of

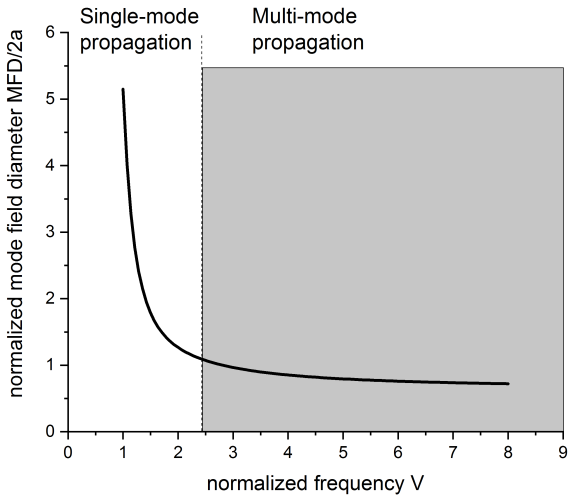

Figure 3.6: Normalized mode field diameter $MFD/2a$ for the fundamental mode as a function of the V-parameter in a step-index fiber, as determined by equation (3.24). Purely single-mode propagation requires $V < 2.405$.

modes, N_{modes}, can be approximated by [11]:

$$N_{modes} \approx \frac{V^2}{2}. \tag{3.25}$$

3.4 Generalised non-linear Schrödinger equation

In order to model the different non-linear effects that result during the propagation of an optical pulse inside an optical fiber (or a general waveguide), the generic solution for the wave equation can be expressed as:

$$E(x, y, z, t) = E_0 \Psi(x, y) A(z, t) e^{i(\beta z - \omega t)}. \tag{3.26}$$

The time-domain envelope $A(z,t)$ is the solution of the generalised non-linear Schrödinger equation (GNLSE) in the frequency-domain [78]:

$$\frac{\partial \widetilde{A}}{\partial z} = -\frac{\alpha(\omega)}{2}\widetilde{A} + \sum_{m\geq 2}\frac{\beta_m}{m!}[\omega-\omega_0]^m\widetilde{A} + j\gamma(\omega)\left(1+\frac{\omega-\omega_0}{\omega_0}\right) \times \mathscr{F}\left(A(z,T)\int_{-\infty}^{+\infty} R(t)\left|A(z,T-T')\right|^2 dT'\right). \quad (3.27)$$

The change of variable:

$$T = t - \beta_1 z \quad (3.28)$$

has been implemented allowing to transform the pulse envelope $A(z,t)$ into a co-moving frame at the envelope group velocity $1/\beta_1$. The β_m are the dispersion coefficients associated with the Taylor series expansion of the propagation constant $\beta(\omega)$ about ω_0 (see Section 3.5.2). $\mathscr{F}(\cdot)$ is the Fourier transform operator and $\widetilde{A}(z,\omega)$ is the Fourier transform of $A(z,t)$ defined as followed:

$$\mathscr{F}\{A(z,t)\} = \widetilde{A}(z,\omega) = \int_{-\infty}^{+\infty} A(z,t)e^{j(\omega-\omega_0)t}dt. \quad (3.29)$$

$\alpha(\omega)$ is the linear propagation loss and $\gamma(\omega)$ is the waveguide non-linear parameter defined as:

$$\gamma = \frac{\omega_0 n_2(\omega_0)}{cA_{eff}(\omega_0)} \quad (3.30)$$

and A_{eff} is the effective mode area which is defined as:

$$A_{eff} = \frac{\left(\int\int_{-\infty}^{+\infty}\left|\Psi(x,y)\right|^2 dxdy\right)^2}{\int\int_{-\infty}^{+\infty}\left|\Psi(x,y)\right|^4 dxdy}. \quad (3.31)$$

Smaller values of A_{eff} increase the non-linearity of the optical fiber by increasing γ, due to the strong confinement of field in the core region. The factor $\left(1+\frac{\omega-\omega_0}{\omega_0}\right)$ added in Equation 3.27 is responsible for self-steepening and it is due to the intensity dependence of the group velocity [78]. Non-linear propagation equations have been derived in both the frequency- and

time-domains. The time-domain equation is usually written by neglecting the frequency dependence of the non-linear parameter and linear propagation loss [79]:

$$\frac{\partial}{\partial z}A(z,T) = -\frac{\alpha}{2}A + \sum_{m\geq 2}\frac{j^{m+1}}{m!}\beta_m\frac{\partial^m A}{\partial T^m} + j\left(\gamma + j\frac{\alpha_2}{2A_{eff}}\right)\left(1+\frac{j}{\omega_0}\frac{\partial}{\partial T}\right) \times \left(A(z,T)\int_{-\infty}^{+\infty} R(T)\left|A(z,T-T')\right|^2 dT'\right), \quad (3.32)$$

where α_2 is the two-photon absorption coefficient.

3.5 Linear effects in optical fibers

3.5.1 Losses

The main factors that contribute to the loss during the propagation of an electromagnetic wave in an optical fiber are material absorption and Rayleigh scattering [78]. The linear propagation loss is defined by:

$$\alpha = -\frac{10}{L}\log\left(\frac{P_T}{P_0}\right), \quad (3.33)$$

where P_0 is the launched power into the core of the optical fiber of length L and P_T is the transmitted power. In the case of optical fibers, α is usually expressed in [dB/m]. Another important extrensic loss factor are bend losses. Based on Maxwell equations [77, 80] and by including the design parameters of the optical fiber, the loss factor for bending can be expressed by:

$$2\alpha_{bend} = \frac{\sqrt{\pi}}{2s}\frac{\left(\frac{u}{V}\right)^2}{(\frac{a^2}{2})K_{l-1}(w)K_{l+1}(w)}\frac{ae^{(\frac{-4w^3\Delta}{3aV^2})R}}{w\sqrt{(\frac{wR}{a})+(\frac{V^2}{2w\Delta})}}. \quad (3.34)$$

The factor α_{bend} represents the losses caused by bending, including a degeneracy factor s, which can be approximated as 2 for the fundamental mode [81]. R is the bend radius of the fiber, w and u are the already introduced (see

Section 3.3) two parameters related to the waveguide dispersion, which can be calculated from the propagation constant β of the mode. K_l is the second kind modified Bessel function of the 1^{st} order:

$$K_l(x) = \frac{\pi}{2}\frac{I_{-l}(x) - I_l(x)}{\sin(\alpha\pi)}. \tag{3.35}$$

$I_l(x)$ is the modified Bessel function of first kind. Moreover, for the fundamental mode, K_{l-1} and K_{l+1} are K_1 [81].

3.5.2 Dispersion

Dispersion refers to a wavelength-dependent phase velocity of propagating electro-magnetic waves inside a material. In optical fibers, this phenomenon can be separated into different contributions:

- **Waveguide dispersion:** this contribution of dispersion arises from waveguide effects. Indeed, the dispersive phase shifts for a wave in a waveguide differ from those which the wave would experience in a homogeneous medium. For the mathematical analysis of the waveguide dispersion, the normalized propagation constant b is introduced for the fundamental mode LP_{01}:

$$b \approx 1 - \left[\frac{1+\sqrt{2}}{1+(4+V^4)^{\frac{1}{4}}}\right]^2, \tag{3.36}$$

  which determines how much of the total radiation propagates in the core of the fiber, assuming a rapid decay of the electro-magnetic field in the cladding with respect to its thickness [82]. This value is plotted in Figure 3.7 versus the normalized frequency V. The waveguide dispersion is then often quantified via a dispersion parameter D_w, which is the time delay per nanometer wavelength and kilometer propagation distance inside a medium caused by this type of dispersion [82]:

$$D_w = -\frac{\lambda}{c} n_{core} \frac{n_{core} - n_{clad}}{n_{clad}} \frac{d^2 b}{d\lambda^2}, \tag{3.37}$$

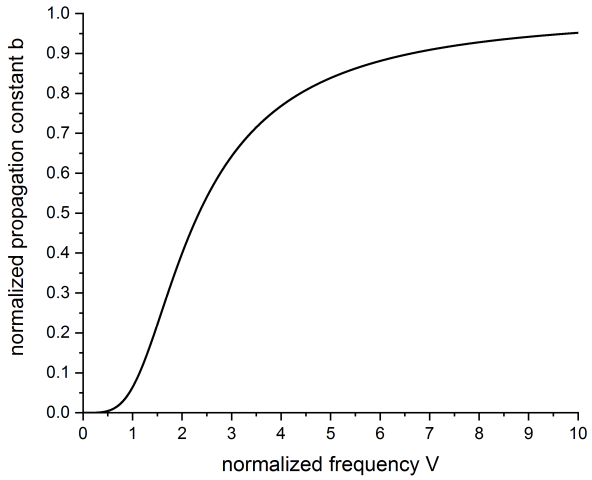

Figure 3.7: Normalized propagation constant b versus normalized frequency V.

where n_{core} and n_{clad} are the refractive indices of the core and the cladding, respectively.

- **Material dispersion:** When a non-monochromatic electromagnetic wave travels in a single mode fiber or in another kind of waveguide, light components of different frequencies interact differently with the surrounding optical medium. This property is the result of the fact that the effective refractive index (n_{eff}) of the medium varies as a function of the light frequency ($n(\omega)$). In other words, light of different wavelengths travels with different velocity. The propagation constant β can be expanded in Taylor series about the center frequency ω_0 as follow:

$$\beta(\omega) \approx \beta_0 + \beta_1(\omega - \omega_0) + \frac{1}{2}\beta_2(\omega - \omega_0)^2 + \cdots + \frac{1}{m!}\beta_m(\omega - \omega_0)^m, \quad (3.38)$$

where β_m is the m^{th} derivate of the mode-propagation constant around

the frequency ω_0:

$$\beta_m = \left(\frac{d^m \beta}{d\omega^m} \right) \Bigg|_{\omega=\omega_0} . \tag{3.39}$$

In particular, the first two coefficients of the Taylor expansion can be expressed in terms of n_{eff} and its derivatives as:

$$\beta_1 = \frac{1}{v_g} = \frac{1}{c} \left(n_{eff} + \omega \frac{dn_{eff}}{d\omega} \right) \tag{3.40}$$

and

$$\beta_2 = \frac{1}{c} \left(2\frac{dn_{eff}}{d\omega} + \omega \frac{d^2 n_{eff}}{d\omega^2} \right) . \tag{3.41}$$

β_1 is the inverse of the group velocity which is the speed of the envelope of a propagating pulse inside the fiber. β_2 stands for the group velocity dispersion (GVD) which is responsible for the pulse broadening in time domain taking into account the different propagation speeds of the different frequency components associated with the traveling pulse. β_2 is a very important parameter, especially in optical fiber communications, because it describes the chirp of an optical pulse and thus the temporal broadening or shortening during its propagation. The GVD parameter β_2 is usually given in the unit of [ps^2/km]. A related material dispersion parameter D_m with opposite sign compared to β_2 is defined as follow:

$$D_m = -\frac{2\pi c}{\lambda^2} \beta_2 = -\frac{\lambda}{c} \frac{d^2 n_{eff}}{d\lambda^2} \tag{3.42}$$

and it is given in unit of [ps/(nm·km)]. The GVD is mostly used in the physics and optics community, whereas D_m is preferred by the engineering community [79].

- **Intermodal dispersion:** it stands for varying propagation characteristics for different transverse modal profiles. This type of dispersion will not be discussed in this thesis due to nearly exclusively used single-mode fibers.

- **Polarization mode dispersion:** this dispersion is based on different polarization states of the propagating modes and will also not be further derived owing to the investigation on centrosymmetric fibers in this thesis, which should theoretically not exhibit polarization-dependent propagation behavior.

The sum of the waveguide and material dispersion is often referred as **chromatic dispersion** and defined as the sum of the two contributions: $D = D_w + D_m$. An important feature is the wavelength at which the chromatic dispersion D is equal to zero and changes sign for longer wavelengths. This wavelength is called zero dispersion wavelength (ZDW). In the context of supercontinuum generation, the position of the ZDW relative to the pump wavelength has great influence on the non-linear spectral broadening characteristics. Two important dispersion regimes depending on the sign of the GVD-parameter have to be distinguished: the normal dispersion regime (where $\beta_2 > 0$, or equivalently $D < 0$) in which the group velocity increases with wavelength, which means that the red components of the pulse travel faster than the blue ones; and the anomalous dispersion regime (where $\beta_2 < 0$, or equivalently $D > 0$) where the group velocity increases with the frequency and so the blue spectral components travel faster than the red ones. Thus, in the linear propagation regime, the dispersion causes a linear frequency chirp depending on the sign of β_2, redistributing the frequency components of the signal inside the pulse envelope, without generating new frequency components (see Figure 3.8).The influence of the dispersion to the supercontinuum generation will be discussed in details in Section 3.7.

3.6 Non-linear effects in optical fibers

Non-linear effects can be observed if the electromagnetic field is intense. The origin of this non-linear behavior is related to the not-harmonic motion of the bound electrons that interact with the traveling electromagnetic field. As

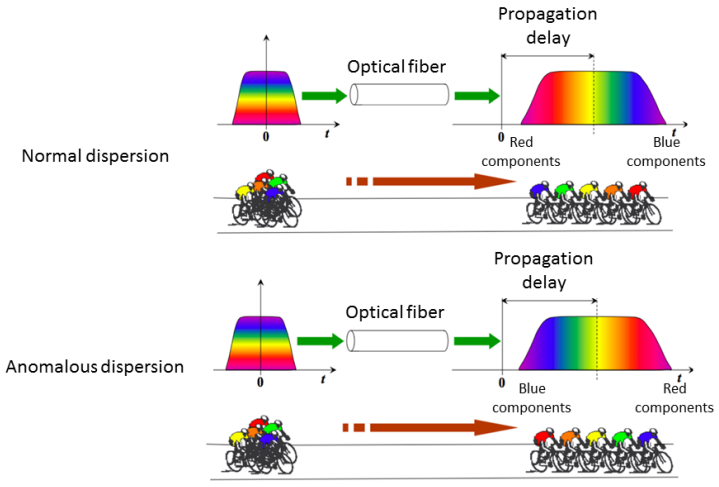

Figure 3.8: In a dispersive single mode fiber, depending on the sign of the GVD (β_2) different spectral components of the traveling pulse experience different speed leading to the temporal broadening of the pulse.

a result, the higher order non-linear susceptibility and the non-linear terms in the total polarization $\mathbf{P}$ in Equation 3.8 are no longer negligible:

$$P_{nl} = \varepsilon_0 \sum_{j>1} \chi^{(j)} \mathbf{E}^j. \tag{3.43}$$

In general, $\chi^{(j)}$ is a tensor of rank (j + 1). The linear susceptibility $\chi^{(1)}$ represents the dominant contribution to $\mathbf{P}$ and its effect is taken into account through the refractive index n and the attenuation coefficient α. $\chi^{(2)}$ is the second order non-linear optical susceptibility which is zero in the case of materials with inversion symmetry (such as glass materials). $\chi^{(3)}$ is the third order non-linear susceptibility. The non-linear effects that originate from $\chi^{(3)}$ are: non-linear refraction and four-wave mixing (FWM). Non-linear refraction arises from the intensity dependence of the refractive index (Kerr effect) as:

$$\bar{n}(\omega, I) = n(\omega) + n_2 I = n + n_2 \left|\mathbf{E}\right|^2, \tag{3.44}$$

where $n(\omega)$ is the linear part which is well approximated by the Sellmeier equation, I is the optical intensity related with the electromagnetic field E and n_2 is the non-linear index coefficient related to $\chi^{(3)}$ by the relation [78]:

$$n_2 = \frac{3}{8n} \operatorname{Re}\left(\chi^{(3)}_{xxxx}\right), \tag{3.45}$$

where, for the sake of simplicity, the optical field is assumed to be linearly polarized so that only one component $\chi^{(3)}_{xxxx}$ of the fourth-rank tensor contributes to the refractive index. The non-linear refraction leads to non-linear effects such as self-phase modulation (SPM) and cross-phase modulation (XPM). These effects are elastic which means that no energy is exchanged between the electromagnetic field and the dielectric medium. Non-linear effects that result from inelastic interchange of energy between the electromagnetic field and the medium are stimulated Raman scattering (SRS) and stimulated Brillouin scattering (SBS).

3.6.1 Self-phase modulation

The simplest effect due to the non-linear refraction is SPM in which the optical field modulates its own phase, due to the Kerr effect. The field amplitude is expressed as:

$$A(t) = A_0 \cdot e^{-j\phi(t)} \tag{3.46}$$

where A_0 is the peak intensity and $\phi(t)$ the instantaneous phase. The change of phase of an optical field changes by:

$$\phi = \bar{n}(\omega, I) k_0 L \tag{3.47}$$

and the non-linear phase shift ϕ_{NL} which can be expressed as:

$$\phi_{NL}(t) = \frac{2\pi}{\lambda} n_2 |A|^2 L. \tag{3.48}$$

In the case where only SPM is included, the non-linear pulse propagation Equation 3.32 can be written as:

$$\frac{\partial A}{\partial z} = j\gamma \left|A\right|^2 A. \tag{3.49}$$

This equation is obtained by assuming an instantaneous material response and ignoring the optical losses. It can be shown that a solution of Equation 3.49 is [78]:

$$A(z,T) = A(0,T)e^{j\gamma|A(0,T)|^2 z} = A(0,T)e^{j\phi(z,T)}. \tag{3.50}$$

On the one hand the temporal pulse shape $|A|^2$ is unchanged during propagation; on the other hand the time dependent phase shift $\phi(z,T)$ gives to the pulse a frequency chirp:

$$\Delta\omega(T) = -\frac{\partial\phi}{\partial T}, \tag{3.51}$$

which is negative near the leading edge of the pulse and positive near the trailing edge of the pulse corresponding to a red-shift and a blue-shift, respectively (see Figure 3.9).

SPM is typically observed in the early stages of supercontinuum generation. In general, the dispersion cannot be neglected during SPM, and the interplay of the two effects must be considered. The results of the interaction depend whether it occurs in the normal dispersion or in the anomalous. In the first case, SPM and normal dispersion interact to lead simultaneous spectral and temporal broadening with the development of a chirp across the central region of the pulse [83], resulting in a more quickly broadening in time of the pulse than that if only dispersion was present. In the second case the interaction between SPM and dispersion leads to the generation of solitons, which will be discussed in the next section.

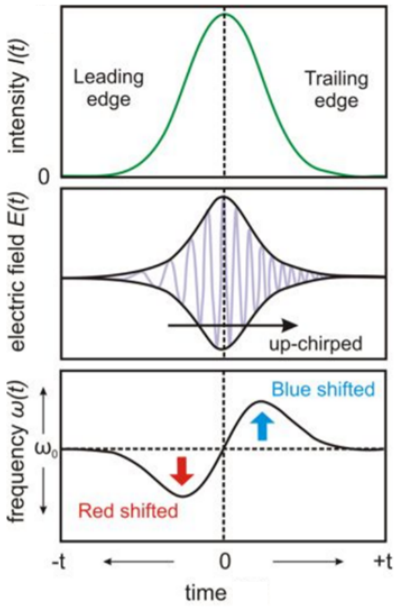

Figure 3.9: Intensity, phase and spectral time-dependence during the self-phase modulation process. Image adopted from [78].

3.6.2 Solitons

The anomalous dispersion leads to a delay of red-shifted pulse components and faster propagation of the blue-shifted part of the pulse. SPM thus compensates the effects of dispersion. It turns out that it is possible for SPM and GVD to exactly balance each other leading to a pulse that can propagate without changing its shape. If the GVD effect is added to Equation 3.49, the GNLSE can be expressed as:

$$\frac{\partial A}{\partial z} = -j\frac{\beta_2}{2}\frac{\partial^2 A}{\partial T^2} + j\gamma\left|A\right|^2 A. \tag{3.52}$$

A solution of this equation, corresponding to a pulse that does not change its shape during propagation, is the fundamental soliton and its expression can be found directly by assuming a shape preserving solution of the form:

$$A(z,T) = V(T)e^{j\phi(z,T)}. \tag{3.53}$$

Inserting this equation into Equation 3.52, then one of its possible solutions is [79]:

$$A(z,T) = \sqrt{P_0}\text{sech}\left(\frac{T}{T_0}\right)e^{\frac{j|\beta_2|}{2T_0^2}z}, \tag{3.54}$$

where P_0 is the peak power of the pulse and T_0 its width. The behaviour of this equation, depends on the value of the ratio N, called the soliton number:

$$N = \sqrt{\frac{L_D}{L_{NL}}} = \sqrt{\frac{\gamma P_0 T_0^2}{|\beta_2|}}. \tag{3.55}$$

This soliton number can be expressed as the ratio of two lengths L_D, the dispersion length and L_{NL}, the non-linear length:

$$L_D = \frac{T_0^2}{|\beta_2|} \quad , \quad L_{NL} = \frac{1}{\gamma P_0}. \tag{3.56}$$

When the peak power P_0 and pulse width T_0 are chosen so that:

$$P_0 = \frac{|\beta_2|}{(\gamma T_0^2)}, \tag{3.57}$$

with $\beta_2 < 0$ to ensure that the dispersion is anomalous, $N = 1$, and the solution is said to be the fundamental soliton. While a higher order soliton is excited in the optical fiber if $N \geq 2$. Higher order solitons do not propagate without changing shape as the fundamental soliton does but they change shape in a periodic manner, recovering their initial shape once each period [78]:

$$z_s \approx \frac{T_0^2}{2\,|\beta_2|}. \tag{3.58}$$

However, during supercontinuum generation, the governing equation is the full GNLSE, and the periodic dynamics is lost. An energetic seed laser pumping in the anomalous dispersion regime can result in a large initial soliton number, and subsequently, the spectrum typically develops through pulse break-up, into a number of fundamental solitons that are often individually distinguishable in a well developed supercontinuum spectrum [79]. This phenomenon will be further discussed in the Section 3.7.

3.6.3 Four-wave mixing and Modulation Instabilities

Four-wave mixing (FWM) describes a non-linear process in which four optical waves oscillating at a frequency ω_1, ω_2, ω_3 and ω_4 interact with each other. FWM is a non-linear interaction between four optical waves. The FWM processes of interest for supercontinuum generation, can be separated in two classes. The first corresponds to the case in which three photons transfer their energies to a single photon at a frequency $\omega_4 = \omega_1 + \omega_2 + \omega_3$. The second corresponds to the case in which two photons at frequency ω_1 and ω_2 are annihilated, while two photons at frequencies ω_3 and ω_4 are created simultaneously so that $\omega_1 + \omega_2 = \omega_3 + \omega_4$. The efficiency of FWM depends strongly on the phase matching condition, namely matching of the wave vectors: $\Delta\mathbf{k} = 0$. Of particular interest is the degenerate case, namely when $\omega_1 = \omega_2$, so that a single input beam can initiate FWM and generate a Stokes and anti-Stokes photon (called sidebands):

$$2\omega_p = \omega_s + \omega_{as}, \tag{3.59}$$

where ω_p, ω_s and ω_{as} are the pump frequency, Stokes wave and anti-Stokes wave frequency, respectively. In this case the phase-matching condition is expressed as:

$$\Delta\mathbf{k} = (2n_p\omega_p - n_s\omega_s - n_{as}\omega_{as})/c = 0, \tag{3.60}$$

where n is the effective mode index at the frequency ω. In the absence of initial seeding, FWM corresponds to an instability of the propagating continuous wave pump and the growth from noise of sidebands symmetric in frequency around the pump. The maximum growth rate is at frequencies satisfying phase-matching. In the time domain, this leads to a temporal modulation, and this process is referred to as a modulation instability (MI). It is important to consider FWM and MI as frequency-domain and time-domain descriptions of the same non-linear phenomenon [84] and both terms are used in literature. In the context of supercontinuum generation, FWM

or MI processes dominate the broadening mechanism in the case of input pulses of picosecond or nanosecond duration [79].

3.6.4 Self-steepening

Self-steepening is a higher order non-linear effect which results from the intensity dependence of the group velocity. It causes an asymmetry in the SPM broadened spectra of ultrashort pulses as the pulse moves at a lower speed than the wings of the pulse [78]. Therefore, as the pulse propagates inside the optical fiber, the peak shifts towards the trailing edge and the trailing edge becomes steeper with increasing distance. Self-steepening of the pulse creates an optical shock and it is only important in the case of ultrashort pulses [79] and for this reason it will not be further investigated in this thesis.

3.6.5 Raman scattering

Raman scattering is another important process during supercontinuum generation and it is related to the imaginary part of $\chi^{(3)}$. In the Raman scattering process, the material interacts with a photon by creating a virtual excited level; the system decays to a lower state by emitting a photon with lower energy, and the energy difference of the two photons is carried away by a phonon. In principle, it is also possible that the photon interacts with the material by absorbing a phonon to generate a higher-energy photon. In this case the resulting photon is defined as an anti-Stokes and it shows a shorter wavelength. The spectra of the optical phonons are relatively broad, in the order of 10 THz to 15 THz for silica, resulting in a large wavelength shift. The process exhibits a threshold-like behavior and the threshold power level is given by [78]:

$$P_{RS} = 16\frac{MFA}{l_{eff} \cdot g_{RS}}, \tag{3.61}$$

where g_{RS} is the Raman gain coefficient dependent on the material. Note that the Raman effect in optical fibers can be used to amplify a weak signal if

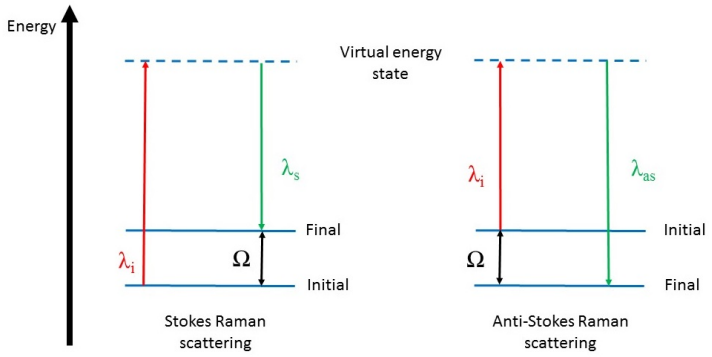

Figure 3.10: Schematic showing the difference between Stokes and anti-Stokes Raman scattering. When a difference in energy occurs between the initial vibrational energy state and the resulting vibrational state, a shift in the frequency of the emitted photon will occur. The difference of these two energy levels is the phonon energy Ω.

that signal is launched together with a strong pump such that their frequency difference lies within the bandwidth of the Raman gain spectrum. In the context of supercontinuum generation, when short pulses are used ($\leq$1 ps) the Raman effect can amplify low frequency pulse components by transferring energy from the high frequency components of the same pulse. Consequently, the shift tends toward the low frequency side increases as the pulse propagates inside the optical fiber [79].

3.7 Influence of the dispersion to the supercontinuum generation

Depending on the position of the pump wavelength with regard to the zero dispersion wavelength of the fiber, different non-linear effects can contribute to the supercontinuum effect during the propagation.

In the case of a non-linear optical fiber pumped in the **normal dispersion region**, namely if the pump wavelength is lower than the zero dispersion wavelength ($\lambda_p < ZDW$), the supercontinuum generation is mainly affected

by the stimulated Raman scattering. This will result in the appearance of individual wavelengths greater than the pump wavelength [79].

In this thesis, only optical fibers with zero dispersion wavelengths lower than 2 μm are used. Since the pump wavelength is located around 2 μm, the optical fibers are pumped in their **anomalous dispersion region** ($\lambda_p > ZDW$). In this case, modulation instabilities are the main cause of supercontinuum generation at the first stage [79]. Modulation instabilities are precursor to the soliton fission and manifest themselves as a breakup of the long pulsewidth pulse radiation into a train of ultra-short pulses during transmission. In the time domain, the pulse disintegrates (soliton fission) and stable soliton entities are formed. As the pulses propagate through the non-linear fiber, each sub-pulse undergoes further spectral broadening through modulation instabilities, stimulated Raman scattering as well as Raman soliton self-frequency shift [85]. This latter phenomenon was discovered in 1986 by Mitschke and Mollenauer [86]. It consists of a continuous redshift of the center frequency of a subpicosecond soliton pulse in a standard single-mode fiber. Due to Raman gain, the blue portion of the soliton spectrum pumps the red portion of the spectrum, causing a continuous redshift in the soliton spectrum. This wavelength shift increases with both input pump power and fiber length. The mathematical basis of Raman soliton self-frequency shift is described by Gordon in [87]: it can be shown that the frequency shift per unit length is proportional to the inverse of the fourth power of the pulsewidth τ:

$$\frac{d\nu}{dz} \propto \frac{h(t)}{\tau^4}, \tag{3.62}$$

where $h(t)$ is a function integrated from the Raman gain spectrum. By pumping in the anomalous dispersion region at an operating wavelength greater than the zero dispersion wavelength of the non-linear fiber, is then possible to broaden the spectrum only toward longer wavelengths [88].

In the case of the pump wavelength equal (or close) to the zero dispersion wavelength of the optical fiber ($\lambda_p \approx ZDW$), the supercontinuum generation

is affected by both solitonic and parametric effects, leading to an homogeneous broadening of the spectrum around the pumping wavelength [79].

3.8 Materials for mid-IR supercontinuum generation

The main goal of this thesis is to investigate non-linear fibers in the mid-IR wavelength range from 2 to 5 μm. Standard optical glass fibers for the telecommunication systems are made of fused silica glass (SiO_2) due to their well-developed optical and mechanical properties. However, silica fibers are not suitable for our experiments since they are transparent up to a wavelength of 2.6 μm because of their intrinsic absorption arising from the excitation of lattice vibrations [89]. In order to target wavelengths above 2.6 μm, soft-glass fibers that are made of glass materials with reduced binding forces, shift the vibrational absorption bands further in the infrared. Side effects of the enhanced transmission range are substantially lower robustness and durability compared to silica fibers.

The most common and mature developed heavy-metal fluoride glass is fluorozirconate commonly known with the acronym ZBLAN. The composition of ZBLAN glass is dependent on the manufacturer, but it is commonly made of ZrF_4 (53%), BaF_2 (20%), LaF_3 (4%), AlF_3 (3%) and NaF (20%) [90]. ZBLAN fibers are transparent from about 0.3 μm up to 4.5 μm [91]. Moreover ZBLAN glass has a low group velocity dispersion with a material zero dispersion wavelength of around 1.6 μm that makes pumping with thulium-doped fiber laser systems feasible in the anomalous dispersion region. Like the fabrication of silica fibers, the preform method in which the fiber is drawn from a preformed glass rod at a temperature below the glass melting temperature, is mostly used for ZBLAN fiber fabrication. However, compared to silica glasses, it is more complicated to make the preform, due to the fact

Material properties	**SiO_2**	**ZBLAN**	**InF_3**
Transmission range [μm]	0.3 - 2.6 [95]	0.3 - 4.5 [96]	0.3 - 5.3 [96]
Transition temperature [°C]	∼1200 [91]	∼260 [97]	∼300 [97]
Refractive index @ 2 μm	1.44 [98]	1.49 [99]	1.48 [99]
Non-linear refractive index n_2 x 10^{-20} [m^2/W]	2.6 [78]	1.8 [79]	0.8 [96]
Zero dispersion wavelength [μm]	1.3 [78]	1.6 [100]	1.8 [100]

Table 3.1: Optical properties of glass fiber materials.

that to achieve high quality fluoride glasses, not only extremely pure starting materials with infrared-absorbing impurities below 1 ppb are needed, but also prevention of contamination are required at all synthesis stages. ZBLAN fiber preforms can be prepared by different casting processes including cladding-over-core casting [92], build-in casting [92, 93] and rotational casting [94]. During the realization of a fiber preform, refractive indices of the core and the cladding have to be precisely controlled to obtain the required index difference. In typical fluoride glasses, PbF_2 and BiF_3 increase the refractive index, and LiF and AlF_3 decrease the index. In order to reduce the crystallization rate, ZBLAN fibers should be drawn with a high drawing speed at temperatures as low as possible, usually in the 340-400 °C range.

A second fluoride glass that has a longer upper wavelength edge of around 5 μm is indium fluoride (InF_3). InF_3 fibers exhibit similar dispersion and nonlinear characteristics compared with ZBLAN fibers and a lower attenuation-induced transmission loss in the spectral range from 4 to 5 μm. However, the fiber drawing technology of fluoroindate glass is technologically not as mature as ZBLAN, and only quite recently the fiber became commercially available. Figure 3.11 displays the material absorption for silica, ZBLAN and InF_3 fibers, respectively. In Table 3.1 some important material properties are summarized from the literature.

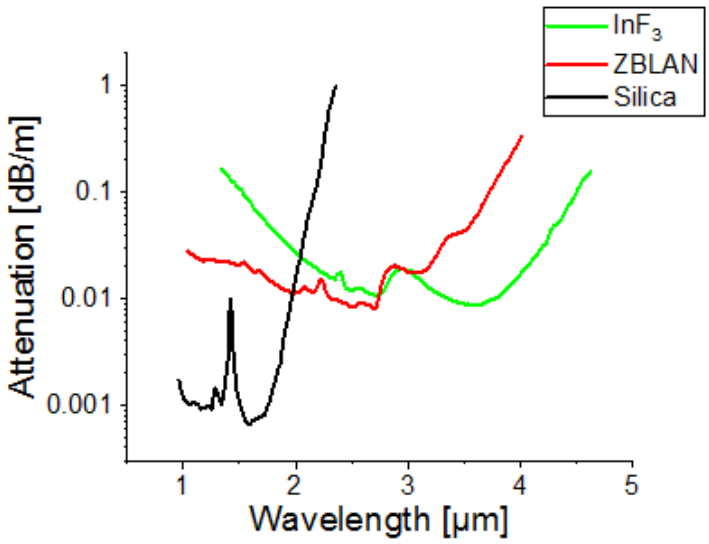

Figure 3.11: Material absorption of silicon oxide (SiO_2), ZBLAN and InF_3 [95, 96].

3.9 State of the art of supercontinuum in fluoride fibers

Supercontinuum generation in ZBLAN and InF_3 fibers, pumped at different pulse durations, has been widely reported over the past decades since the first demonstration of supercontinuum generation in a ZBLAN fiber in 2006 by Hagen *et al.* [101]. In this section a review of the main supercontinuum generation results in ZBLAN and InF_3 fibers that can be found in literature is given. Particular attention is dedicated to the characteristics of the pump source, the fiber properties and concerning the supercontinuum spectrum, its spectral width and average power. Table 3.3 gives an overview of the main supercontinuum results achieved in ZBLAN and InF_3 that are cited in this thesis.

3.9.1 ZBLAN fibers

In the first demonstration in 2006, by Hagen *et al.* [101], a 900 fs pulse produced by a commercial erbium-doped fiber laser has been used to pump a cascaded silica fiber and ZBLAN fiber. The output spectral wavelength range from 1.8 μm spanned to 3.4 μm, and the total average power in this range was 5 mW.

In 2009, Xia *et al.* described an all-fiber-integrated supercontinuum system [81]. The pump system comprises a 1542 nm laser diode generating 1 ns pulses, followed by a single-mode erbium-doped fiber amplifier and multistage cladding-pumped erbium/ytterbium c odoped fiber amplifiers. The optical spectrum of the amplified nanosecond pulses is then broadened by a 2 m length of standard single-mode fiber followed by a 7 m length of ZBLAN fiber. This fiber has a core diameter of 8.9 μm, a cladding diameter of 125 μm and an NA of 0.2. The supercontinuum radiation had a maximum average power of 10.5 W and a continuous spectrum from $\sim$0.8 to 4 μm.

A high average output power in a single-mode ZBLAN fiber has been obtained in 2014 by Liu *et al.* [102], where a single-mode thulium-doped fiber master oscillator power amplifier (MOPA) is used as pump source. The seed source of this MOPA system was a SESAM mode-locked thulium-doped fiber laser with pulse width of 24 ps and repetition rate of 93.6 MHz at 1963 nm. Firstly, the laser spectrum from the seed is broadened to beyond 2.4 μm in a two-stage single mode thulium-doped fiber amplifier with an average power of 42 W. Then, a cascaded single-mode ZBLAN fiber further broadens the output spectrum from the thulium-doped fiber amplifier to 3.8 μm with an average power of 21.8 W. The $\sim$10 m long ZBLAN fiber has a core/cladding diameter of 9/125 μm and an NA of 0.2. The zero-dispersion wavelength is 1.57 μm. To prevent heat induced damage, the fiber is wrapped on an aluminum cylinder with machined spiral grooves.

Another approach for supercontinuum generation based on thermal splicing of a silica fiber and a ZBLAN fiber has been presented by Zheng *et al.* in

2016 [103]. The pump source is a MOPA system, in which the seed laser is a passively mode-locked thulium-doped fiber laser emitting at 1950 nm using a SESAM providing 12.58 ps pulses with a repetition rate of 75.4 MHz. The achieved maximum mid-IR supercontinuum power is 10.67 W with a wavelength spectrum spanning from ∼1.9 to 4.1 μm. Permanent splicing between fibers is the key technique to achieve an integrated all-fiber system. In that work, the ZBLAN fiber for supercontinuum generation has been connected with a standard silica fiber SM1950 by thermal splicing. Fibers with proper end faces flat cleaved, have been fixed on a commercial splicer with a filament as heat source for the splicing. Due to the different fiber melting temperature, an offset splicing method has been used, in this case more heat is applied to the SM1950 silica fiber. After the thermal splicing, the joint was covered with high index UV adhesive and packaged into an aluminum groove after curing and sink on cooled water for better thermal management.

In 2017, Yin *et al.* [104], obtained a supercontinuum generation power beyond 3 μm . A 12 m length of ZBLAN fluoride fiber was used as non-linear medium, which was pumped by a thulium-doped fiber amplifier through a firm fusion-spliced joint with silica fiber. The seed pulses had a duration of 1 ns and a repetition rate of 6 MHz. Then, they were amplified by an erbium-doped fiber amplifier and two erbium/ytterbium-codoped fiber amplifiers to scale up the laser pulse intensities. The peak power after these amplification stages was around 2 kW. The maximum total supercontinuum power was 15.2 W and for wavelengths beyond 2.4 μm, 3 μm and 3.8 μm the average output power was 12.5, 8.1 and 1.08 W, respectively.

Recently, in 2019, the highest average output power supercontinuum radiation has been achieved by Yang *et al.* [105]. They reported an all-fiber supercontinuum source using a piece of ZBLAN fiber. This fiber had a core diameter of 10 μm and it was directly fusion-spliced to the pump source. This pump was a broadband thulium-doped fiber amplifier spanning from 1.9 μm to 2.6 μm. A supercontinuum output average power up to 30 W and

a spectral coverage from 1.9 μm to 3.6 μm was obtained. Such good result was obtained because of the low-loss and robust splicing together with a robust AlF_3 end-cap to prevent water diffusion due to the slightly hygroscopic nature of the fluoride fibers.

3.9.2 InF_3 fibers

The first demonstration of supercontinuum generation in an InF_3 fiber was reported by Théberge in 2013 [100]. A 9.5 m long 16 μm core fiber pumped with 70 fs pulses at 3.4 μm was used and a supercontinuum spectrum spanning from 2.7 to 4.7 μm was presented.

Since then, much effort has been paid to improve the output power as well as the spectral coverage of InF_3 fiber-based mid-IR supercontinuum. Swiderski *et al.* and Michalska *et al.* scaled the output power to 2.09 W and 1.4 W using an erbium-ytterbium-doped fiber amplifier and a thulium-doped fiber amplifier, respectively, with a 20-dB spectral coverage of 1.05-2.65 μm [91] and 1.87-3.9 μm [106]. The pulse duration for both systems was $\sim$1 ns.

Afterwards, Gauthier *et al.* [107] pumped a 15 m long piece of InF_3 fiber with an erbium-doped ZBLAN fiber amplifier seeded by sub-nanosecond pulses from an OPO operating at 2.8 μm, and extended to 5.4 μm the supercontinuum upper limit.

Recently, in the experiment of Liang *et al.* [108], a gain-switched diode-seeded thulium doped MOPA producing up to 295 kW picosecond pulses (35 ps) at a repetition rate of 1 MHz has been used to pump a $\sim$1 m long segment of InF_3 fiber. They generated watt-level ($\sim$1.7 W) supercontinuum spanning from 750 nm to 5000 nm.

The first 10 Watt-level supercontinuum generation in InF_3 fibers (and, up to date, the current highest average output power) belongs to Wu *et al.* [109]. In their experiment, the supercontinuum source is composed of a thulium-doped MOPA system and 11 m long segment of InF_3 fiber. The thulium-doped MOPA system consists of a mode-locked thulium-doped fiber laser

and a dual-stage single-mode thulium-doped fiber amplifier. The seed laser is mode-locked by a SESAM and emits laser pulses with a pulse repetition rate of 33 MHz and pulse duration of 60 ps. The InF_3 fiber had a core diameter and core NA of 7.5 μm and 0.3, respectively. The fiber has been fusion spliced to the output fiber of a mode field adapter placed between the MOPA system and the InF_3 fiber. A maximum supercontinuum average output power of 11.3 W has been demonstrated with a spectrum extension up to 4.7 μm.

Reference	Pump source	Fiber properties	SC Spectral width	SC Output power
Yang *et al.* [105]	Tm-doped fiber amp. 1 ns, 30 MHz 1.9 μ to 2.6 μm	ZBLAN 10/125 μm ⌀ ZDW 1.56 μm	1.9 - 3.8 μm	30 W
Liu *et al.* [102]	Tm-doped fiber MOPA system 24 ps, 93.6 MHz 1963 nm	ZBLAN 10 m 9/125 μm ⌀ ZDW 1.57 μm	1.9 - 3.8 μm	21.8 W
Xia *et al.* [81]	Er-doped fiber amp. 1 ns, 3.3 MHz 1542 nm	ZBLAN 7 m 9/125 μm ⌀ ZDW 1.57 μm	0.8 - 4 μm	10.5 W
Zheng *et al.* [103]	Tm-doped fiber MOPA system 13 ps, 75.4 MHz 1950 nm	ZBLAN 8 m 9/125 μm ⌀ ZDW 1.57 μm	1.9 - 4.1 μm	10.67 W
Yin *et al.* [104]	Tm-doped fiber amp. 1 ns, 6 MHz $\sim$2 μm	ZBLAN 12 m 9/125 μm ⌀ ZDW 1.49 μm	1.9 - 4.2 μm	15.2 W
Swiderski *et al.* [91]	Er-Yb-doped fiber amp. 1 ns, 420 kHz 1.55 μm	InF_3 8 m 16.7/125 μm ⌀ ZDW 1.83 μm	1.05 - 2.65 μm	2.09 W
Michalska *et al.* [106]	Tm-doped fiber amp. 1 ns, 500 kHz 1.8 - 2.7 μm	InF_3 12 m 9/125 μm ⌀ ZDW 1.83 μm	1.87-3.9 μm	1.4 W
Gauthier *et al.* [107]	Er-doped fiber amp. $<$ 1 ns 2.8 μm	InF_3 15 m 13.5/100 μm	2.35-5.4 μm	21.4 mW
Liang *et al.* [108]	Tm-doped MOPA system 35 ps, 1 MHz 1952 nm	InF_3 1 m 9/125 μm ⌀	0.75 - 5 μm	$\sim$1.7 W
Wu *et al.* [109]	Tm-doped MOPA system 60 ps, 33 MHz	InF_3 11 m 7.5/125 μm ⌀	0.8-4.7 μm	11.3 W

Table 3.3: Resume of the main supercontinuum results achieved in ZBLAN and InF_3 cited in this thesis.

Chapter 4

Characterization of thulium-doped silica fiber pump laser

In the following chapter the characteristics of the thulium-doped fiber laser used for supercontinuum generation will be presented. The mechanisms leading to laser-induced thermal damages in optical fibers are shown and the characteristics of the two AR-coated fused-quartz end caps spliced at the tips of the active thulium fiber to solve these issues are discussed. The results are then presented for the different operational regimes of the laser, namely continuous wave, Q-switching and Q-switched mode-locking. Even if only the latter regime has been used for supercontinuum generation, the other regimes of the fiber laser have been investigated to better understand and improve the performances of the laser source.

4.1 Experimental setup

Figure 4.1 represents the schematic drawing of the pump thulium-doped silica fiber laser emitting at 2 μm used during this thesis. The radiation from two fiber pigtailed pump diode modules is collimated by two AR-coated achromatic lenses whose focal length is 20 mm. The diode set emits at a wave-

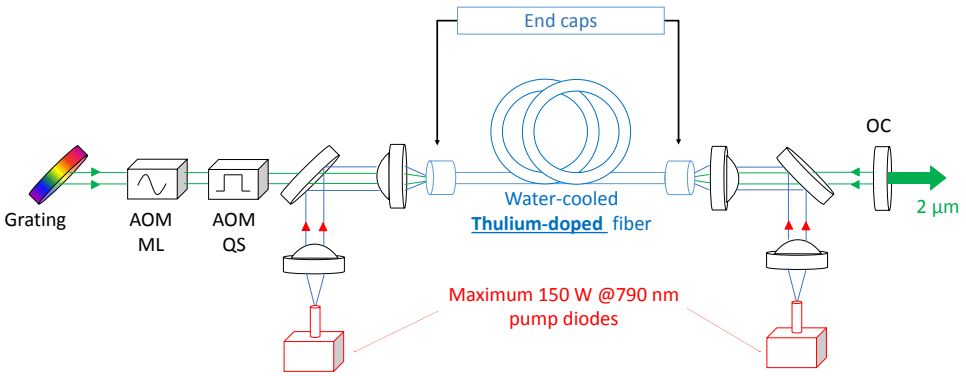

Figure 4.1: Schematic setup of the thulium-doped fiber laser.

length of 792 nm and they are actively-cooled with a controlled water flow at a temperature of 18 °C providing a total power of 150 W per module. Their radiation is delivered via multimode fibers with a core diameter of 400 μm and an NA of 0.22 (which corresponds to a beam quality factor M^2 of the pump radiation of around 140). Then the light is reflected by two dichroic mirrors which are transparent for the laser wavelength and highly reflecting for the pump diodes under an incident angle of 45°. The pump radiation is then launched into the active thulium-doped fiber by two AR-coated (at the pump and laser wavelength) lenses with a focal length of 15 mm. These lenses are used to collimate the laser beam as well; however, due to the different refractive index at the two wavelengths, the 2 μm laser output beam is slightly divergent. The thulium-doped fiber is placed in a steel container which is filled with water cooled at a temperature of 19 °C. The fiber has a bend radius of around 10 cm inside the steel container. The bend losses have been estimated to around 0.006 $\frac{dB}{m}$ at a wavelength of 2 μm using Equation 3.34 from Section 3.5.1. For active mode-locking and active Q-switching,

two free-space AOMs are used inside the cavity. The data sheet from the manufacturer states a diffraction efficiency of the AOM for Q-switching of more than 90%, when operated at a fixed radio-frequency of 40 MHz with a build-up time of 500 ns. The AOM for mode-locking provides a diffraction efficiency of at least 10%, depending on the power of the radio-frequency. A diffraction grating with 450 grooves per millimeter and 70% of diffraction efficiency for the 0^{th} order at 2 μm has been used as end cavity mirror. This implementation allows for wavelength tuning, which is obtained by changing the grating orientation around the vertical axis. Furthermore, the grating has a damage threshold of 7 J/cm^2 in pulsed operation and 3 kW/cm^2 for continuous wave lasers; these values are higher than 2.5 J/cm^2 and 2 kW/cm^2 estimated during pulsed regime and continuous wave, respectively. For the characterization of the laser power a high power water cooled thermal sensor is used (Ophir Photonics - L300W-LP). This sensor has a broadband spectral detectivity range from 0.19 to 20 μm and a measurable power range from 1 to 300 W. For measuring the output laser wavelength, an optical spectrum analyzer (Yokogawa - AQ6376) with a large wavelength coverage from 1500 to 3400 nm is employed. The spectral linewidth resolution for this device has been measured resulting in 0.11 nm at 2 μm [110]. This system cannot be used for supercontinuum spectra measurements since it cannot detect wavelengths longer than 3.4 μm. For that purpose, a 320 mm focal length monochromator (Jobin-Yvon - iHR320) and a InSb detector (EG&G - Judson, Model: J10D - M204 - R01M - 20) have been used. This setup will be described in details in the following chapter. Two different photo-detectors have been used to measure the pulse width of the laser depending on the pulse duration. The first is a photoelectromagnetic detector with an electrical bandwidth up to 1 GHz (Vigo System, Model: PEM-10.6) suitable for pulses with $>$ 400 ps duration. The second photo-detector (Discovery Semiconductor - DSC2-30S) is an uncooled InGaAs high speed photodiode designed for high power applications with bandwidth up to 22 GHz resulting

in a minimum detectable pulse duration of 15 ps and longer. In order to visualize and process the signal from the detectors, an oscilloscope with an electrical bandwidth of 50 GHz is available (Tektronix - DPO75002SX). For measuring the beam profile intensity, a thermal camera (Spiricon - Pyrocam III) has been employed. This camera is sensitive for wavelengths between 1.06 μm and 3000 μm and its active area is 12.8 mm $\times$ 12.8 mm.

4.2 Thulium-doped fiber

The specifications of the non-polarization maintaining active thulium-doped fiber are summarized in Table 4.1. The doping concentration has been chosen around 2.8 %wt., in order to ensure a good CR efficiency [27]. This value of doping concentration corresponds to a thulium ions concentration of $1.86{\cdot}10^{26}$ ions/m^3. The core diameter is 25 μm with an NA of 0.09. The normalized factor V is 3.14 at a laser wavelength of 2 μm resulting in a sligthly multimode fiber. As shown in Figure 4.2, the shape of the cladding is octagonal to increase the absorption efficiency. The distance between two opposite flat sides is 300 μm. The NA of the inner cladding is 0.46, which gives a pump beam quality M^2 of around 200. The outer cladding is a round shaped polymer material with a diameter of 460 μm. The nominal fiber absorption is 4.5 dB/m at 790 nm. The length of the fiber has been chosen taking care about two different factors: the absorption of the fiber in order to reach good lasing efficiencies and to prevent any damages for the diode modules due to the non-absorbed pump radiation, and the length of the optical cavity, in order to match it with the frequency repetition rate of the AOM for mode-locking. According to the manufacturer, 10% is the maximum amount of power that can be back-scattered without having feedback induced instabilities or diode damages. Therefore, a pump light absorption of the thulium fiber around 10 dB is needed to ensure safe operation for the diode modules over the whole output power range. A theoretical absorption

Parameter	Value
Doping level [%wt.]	2.8
Core diameter [μm]	25
NA core	0.08
Inner cladding diameter [μm]	300
NA inner cladding	0.46
Outer cladding diameter [μm]	460
Absorption at 790 nm [dB/m]	4.1
Polarization maintaining	NO

Table 4.1: Optical properties of Thulium-doped silica fiber used in this thesis. From manufacturer.

of 10 dB is obtained with a length of 2.2 m of thulium fiber. By pumping the fiber from one side only the absorbed power has been measured around 90% (9 dB). This difference is most likely due to the slightly different length of the fiber, that has been changed during the stripping and cleaving procedures.

4.3 Choice of end-caps solution

Most of the experimental issues during this thesis raised from the thermal instability of the pump laser source at high power operation. In fact, the tips of the fiber are subject to high localized heat that can lead to the damage of the active fiber and stop the lasing action.

Depending on the characteristics of the laser radiation, different factors can contribute to the laser induced damages in optical materials. For pulsed laser radiations in the range of nano- or pico-seconds duration, the fundamental mechanisms responsible for bulk damage in a glass material are avalanche

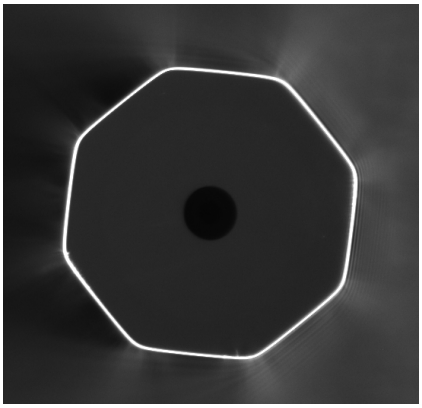

Figure 4.2: Example of a fiber cross-section used as thulium-doped active fiber. The image has been recorded with the camera system of a fiber splicer machine.

breakdown and electronic heating [111]. It starts from an initial conduction band electron in the solid that is accelerated by the electric field of the electromagnetic wave. When the field is sufficiently intense, the electron may be accelerated, so that it can create a new conduction electron by ionization or by creation of an electron-hole pair. The electrons transmit a fraction of their energy to phonons that, in turn, lead to heating of the lattice. For fused silica glass, the threshold for avalanche breakdown is $\sim$100 J/cm^2 [36] for nanosecond pulses at a wavelength of 1 μm. For continuous wave radiation, the reason for bulk damage in dielectric materials is mainly induced by defects. Most materials contain absorbing impurities. These may originate either from the raw materials or from the fabrication processes and can be minimized using appropriate technologies. Gas treatments, for example, have been shown to eliminate or melt these absorbing particles into even smaller contaminating fractions [112]. If the defect is large enough ($> 10\lambda$ of irradiation), the particle will heat up, add to the absorption coefficient and act as a scattering center. If the impurity size is between 10λ and 0.1λ, the particle will absorb and strain the lattice. Finally, if the size is lower than 0.1λ, then it will only add to the absorption but not lead to either the scatter

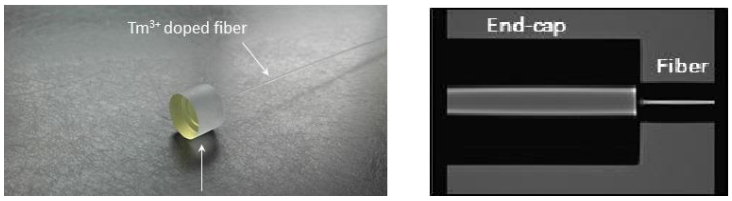

Figure 4.3: *left:* AR-coated fused-quartz end cap fusion-spliced on the fiber tip; *right:* Profile of the splicing, observed with the Fujikura splicer's camera.

of the light or the strain in the lattice. The choice of a high quality preform and the minimization of external particles during the drawing process of optical fibers are then extremely important to reduce the laser-induced bulk damage.

The damage phenomenon of an optical fiber is usually determined by the surface conditions rather than the bulk material. The maximum power that can be guided within a fiber is mainly restricted by the maximum power density at the fiber extremities [113]. Moreover, even microscopic pollution at the interface between the air and the optical fiber probably can initiate end facet damage. These detrimental effects can be obviated using an end-cap, which is a short length of bulk glass material spliced onto the fiber tip. Without a fiber core to confine the beam, the mode field diameter of the beam will diverge within the end-cap: the large diameter reduces the power density and improves the tolerance to the end face defects [114]. In addition to that, in the 2 μm pump laser system used in this thesis, the end-caps are clamped in such a way that all the active fiber is actively-cooled over its entire length. The left side of Figure 4.3 shows one side of the fiber spliced with an end-cap; whereas the right part of the figure shows the side profile image of the splicing taken by the integrated camera of the splicer machine. Figure 4.4 shows the schematic drawing of the fiber end cap. According to the geometric relationships, the diameter of the laser spot at the output surface of the end cap (D_{spot}) is given by the following relationship, where

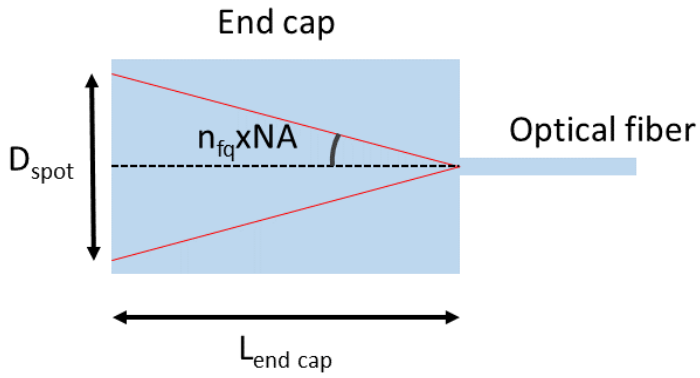

Figure 4.4: Schematic drawing of the fiber end cap.

n_{fq} is the refractive index of fused quartz (1.44 at a wavelength of 2 μm):

$$D_{spot} = MFD_{core} + 2L_{endcap} \cdot \tan(n_{fq} \cdot NA) \tag{4.1}$$

in this formula, MFD_{core} is the mode field diameter of the core at 2 μm, L_{endcap} is the length of the end-cap. Using this relation, D_{spot} is equal to $\sim$1.1 mm. The resulting beam area at the fiber end face significantly lowers the power density, namely by more than three orders of magnitude. A CO_2 laser splicer has been used to splice the end-cap to the thulium-doped optical fiber. At present, the electrode discharge and flame methods are widely applied in most fiber splicing machines, but in the case of large core diameter fibers, as in the case of the end-caps, it is very difficult to control the heat. Unlike these splicing machines, a CO_2 splicer uses thermal absorption to splice the fiber, and with this technique it is easier to precisely control the deposited heat. Moreover, the CO_2 laser can guarantee that no any attached pollutant is added to the splicing point, and the stable temperature of the splicing point [115]. The implementation of these end-caps has drastically improved the thermal handling of the entire pump laser system.

In order to test the stability of the splice and the laser performances, the output power has been monitored for 2 hours in Q-switched mode-locking

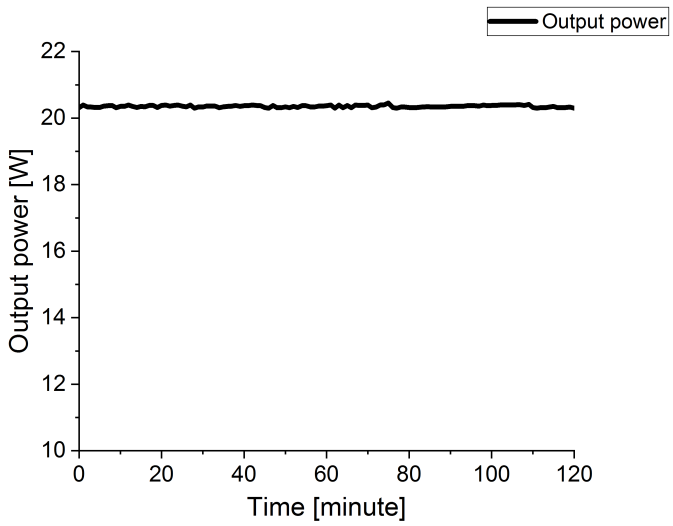

Figure 4.5: Output power stability measurement during 2 hours at 20 W in Q-switched mode-locking regime.

regime at 20 W. The result of this test is shown in Figure 4.5 and it proves the optimal stability of the laser without any detrimental effect on the splice between the thulium fiber and the end-cap.

4.4 Results

4.4.1 Continuous wave operation

The measured output power versus the emitted pump power is shown in Figure 4.6. A total power of 45 W has been reached with a slope efficiency of 58%. The experimental pump power threshold was around 5.2 W and for a lasing wavelength of $\sim$1.9 μm. In order to prevent possible thermally induced damages of the fiber, the maximum pump input power was limited to $\sim$90 W, corresponding to a power density of 2 kW/cm^2 on the fiber extremities.

According to ISO Standard 11146 [116], the beam quality factor M^2 can be calculated with a fitting procedure, applied to the measured evolution of

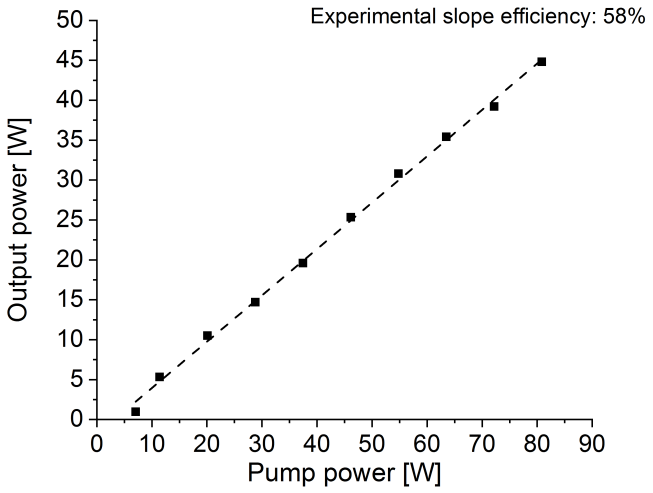

Figure 4.6: Output power versus launched power in continuous wave operation. The highest achieved value is 45 W with a slope efficiency of 58%.

the beam diameter along the propagation direction z, that can be expressed as:

$$d(z) = \sqrt{a_1 + a_2 z + a_3 z^2} \tag{4.2}$$

From the values of a_1, a_2 and a_3, one can obtain the value of M^2 as:

$$M^2 = \frac{\pi}{8\lambda}\sqrt{4a_1 a_3 - a_2^2} \tag{4.3}$$

In continuous wave, an M^2 value of 1.1 in both x and y transverse directions has been observed at an output power level of 20 W. Figure 4.7 shows the results of the measurement. The nominal V-parameter for the active thulium-doped fiber is 3.14, and thus, the fiber is not strictly single mode. The observation of a beam with an M^2 of 1.1, near to the diffraction limit, indicates that the fiber laser is operating primarily, if not exclusively in single mode, most likely due to high losses for higher order modes due to the coiling of the fiber inside the active-cooled container. It is interesting to note that this value will ensure a good coupling into a single-mode fiber.

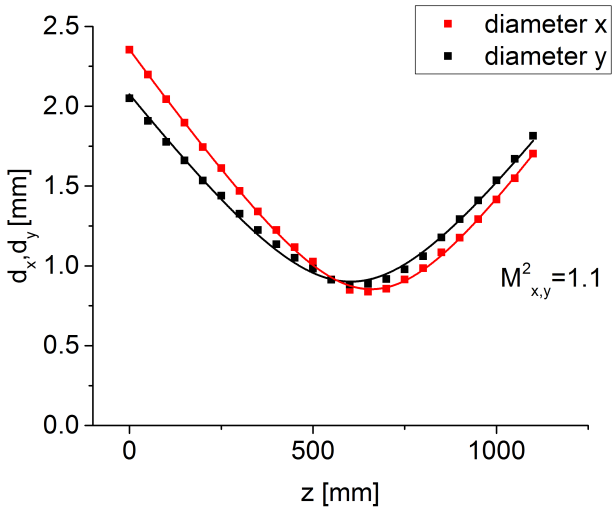

Figure 4.7: M^2 measurement for x and y transverse directions at an output power level of 20 W.

The use of the grating as end cavity mirror allows to change the emitted laser wavelength. The broad emission cross-sections of the thulium-doped silica fiber enable a broad wavelength tuning from 1920 – 2050 nm. The results are shown in the left part of Figure 4.8. The lasing linewidth of the most efficient laser wavelength is shown in the right part of Figure 4.8. The linewidth has been measured around 0.17 nm.

4.4.2 Q-switching

For the Q-switching operation, the laser is first characterized by measuring the output power versus the pump power at different Q-switch repetition rates. The results are shown in Figure 4.9. The slope efficiencies and the lasing threshold are similar to the continuous wave operation. However, at a certain pump power, depending on the Q-switching repetition rate, the output power decreases. The reason of this decrease can be attributed to ASE (Amplified Spontaneous Emission). Indeed, when the Q factor of the

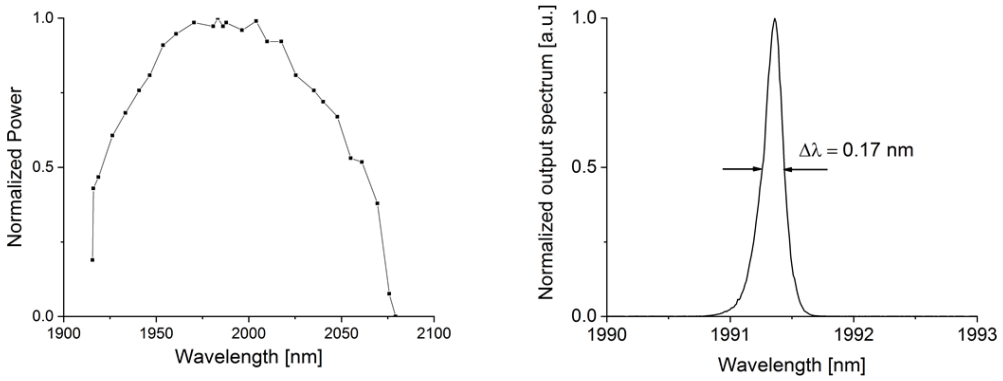

Figure 4.8: *left:* Tunability of the laser; *right:* Output spectrum at the most efficient laser wavelength.

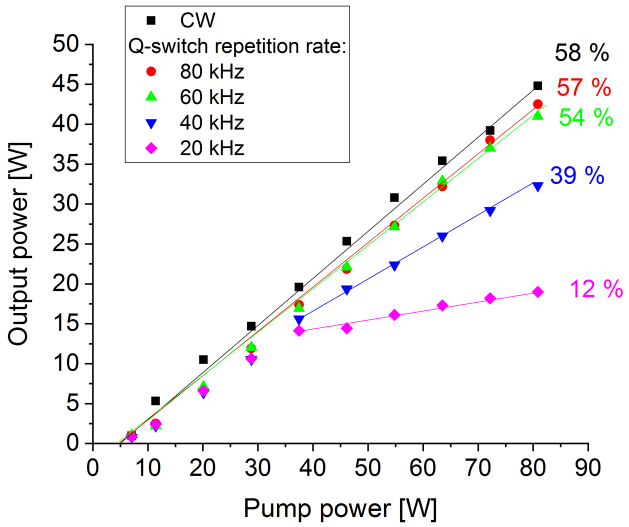

Figure 4.9: Output power versus launched pump power in Q-switching operation at different Q-switch repetition rates.

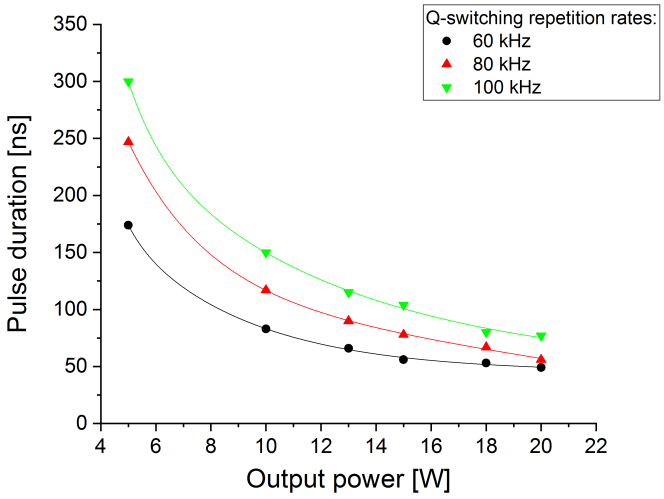

Figure 4.10: Measured pulse duration versus average output power during Q-switching operation for different Q-switching repetition rates.

cavity is decreased, a population inversion is created and the energy is stored in the active fiber. ASE in the fiber can depopulate the upper level and decrease the stored energy, thus limiting the Q-switched pulse. Increasing the pump power further increases the ASE while the inversion stays fixed at the ASE threshold. The increase of the pulse peak power is less proficent and the Q-switched operation becomes then less effective and less stable [60].

The Q-switching output FWHM pulse duration has been measured for different output power levels and Q-switching repetition rates. During these measurements the laser was operating at a wavelength around 1.9 μm. The curves shown in Figure 4.10 indicate the evolution of the Q-switching pulse duration versus the output power. E_{QS}, can be defined as:

$$E_{QS} = \frac{P_{out}}{\Delta\nu_{QS}} \tag{4.4}$$

As shown in Figure 4.11, the maximum achieved pulse energy was 330 μJ at a repetition rate of 60 kHz, a pulse duration of 48 ns and a peak power of approximately 7 kW.

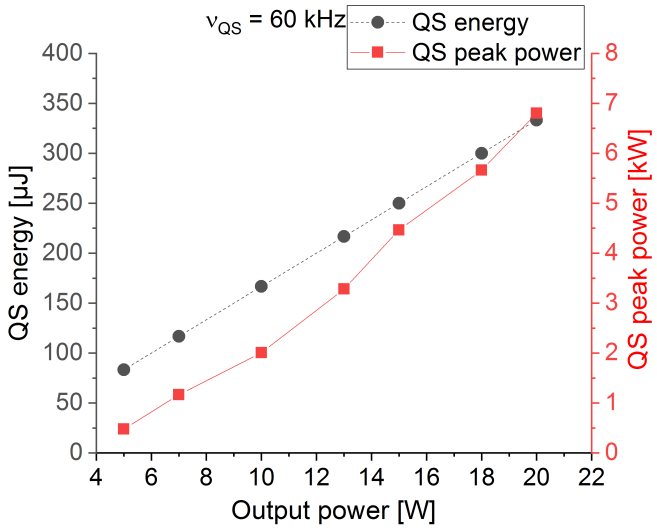

Figure 4.11: Energy and peak power of the pulses in a Q-switching operation at a repetition rate of 60 kHz.

Figure 4.12 shows the lasing linewidth of the Q-switching output radiation for different Q-switching pulse energies at a repetition rate of 60 kHz. For an increase of energy from 89 μJ to 240 μJ, the output spectrum broadens from 0.15 nm to 1.5 nm. This spectral broadening is due to self-phase modulation [117].

The fiber laser output performance concerning beam quality and wavelength tunability are similar compared to the continuous wave regime.

4.4.3 Q-switched mode-locking

When active Q-switching and active mode-locking are employed simultaneously, the mode-locked pulses train is modulated by the Q-switch, resulting in energies and peak powers that can be orders of magnitude higher compared to single Q-switching or mode-locking. Figure 4.13 reports a typical Q-switched mode-locking pulse train. The measurement has been performed at an output power level of 15 W and a Q-switch repetition rate of 120 kHz.

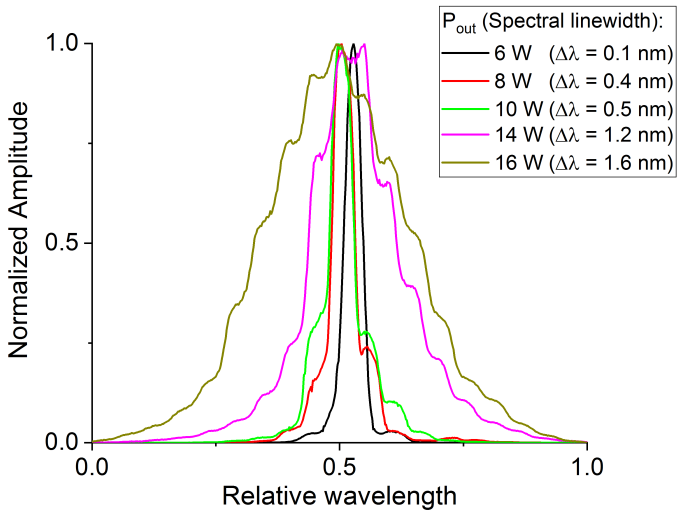

Figure 4.12: Measured output spectral linewidth for different Q-switching output energy levels at a constant repetition rate of 60 kHz.

At this output power level and Q-switch repetition rate, about 9 mode-locked pulses are enveloped by the Q-switch modulation and the Q-switch envelope is around ∼90 ns.

In order to establish a stable mode-locking regime, an AOM for active mode-locking is used. This component is a standing-wave modulator consisting of a fused quartz optic with a $LiNbO_3$ transducer and a Brewster window configuration. As already described, a laser is mode-locked when the longitudinal cavity modes of the laser are forced to maintain a fixed phase relationship with each other. From a frequency-domain point of view, introducing a time-varying transmission through an amplitude modulator inside the laser resonator creates sidebands on each oscillating axial mode which overlap with adjacent axial modes. The operation can be described by assuming that the mode with the frequency ν_o, nearest the peak of the laser gain profile, will start to oscillate first. If the AOM operates at a frequency ν_m, the carrier frequency ν_o will develop sidebands at $\pm\nu_m$. If the modulating frequency is

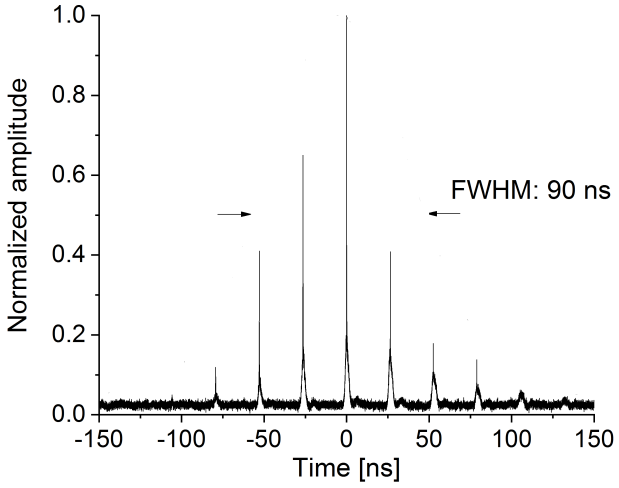

Figure 4.13: Q-switched mode-locked pulse train, the measure has been performed at an output power of 15 W and Q-switch repetition rate of 120 kHz.

chosen equal to the axial mode frequency separation ($\nu_m = \Delta\nu = c/2L$), the coincidence of the upper ($\nu_o + \nu_m$) and the lower ($\nu_o - \nu_m$) sidebands with the adjacent axial mode resonances will couple the two modes with a defined amplitude and phase. As the $\nu_o - \nu_m$ and the $\nu_o + \nu_m$ oscillations will pass through the modulator, they will also be modulated and their sidebands will couple to the $\nu_o \pm 2\nu_m$ modes to the previous three modes. This process will continue until all axial modes falling within the laser linewidth are coupled. The mode-locker transducer operates at a precise frequency with a very narrow bandwidth (10 kHz). This requires the laser cavity length to be adjusted to match the mode locker resonant frequency with a precision cavity length adjustment on the micron scale. Moreover, the laser resonator cavity should be temperature stabilized as every change in length will effect the mode-locked pulse output. For this reason, the mode-locking modulator includes a thermoelectric heat controller to fine tune the resonant mode locker frequency which is adjusted to match the precise driver frequency. A thermistor

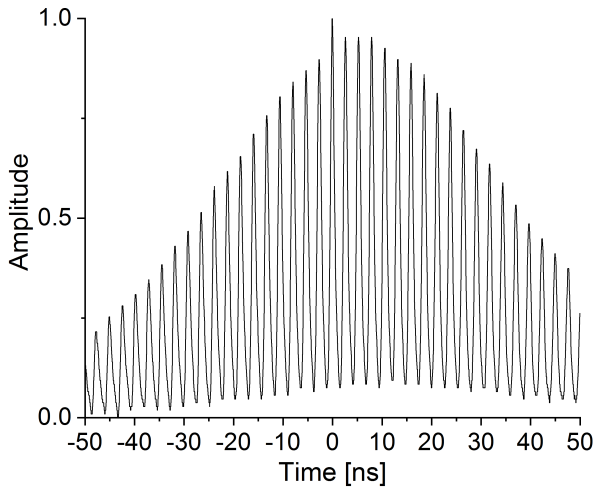

Figure 4.14: Mode beating of the fiber laser in continuous wave operation with additional modulation caused by relaxation oscillations.

is attached to the optic in order to monitor its temperature and drive the thermoelectric heat controller to maintain the temperature constant.

In order to determine the round-trip time τ_{rp} and the fundamental repetition rate, it is possible to monitor the mode beating of the laser system in continuous wave operation. A typical temporal evolution of the mode beating signal is shown in Figure 4.14 where the relaxation oscillations of the continuous wave output signal are additionally modulated by this mode beating effect, whose frequency corresponds exactly to the fundamental repetition rate of the laser cavity [118]. The fundamental repetition rate has been measured resulting in a frequency of 37.9 MHz which corresponds to an optical cavity length of 3.9 m. Different effects can change the optical cavity length. Because of the broad tunability of the thulium-doped fiber laser, the change in optical length of the cavity caused by the material dispersion has to be considered. The derivative of the refractive index versus the wavelength at around 2 μm for silica is around 1.55 nm^{-1} [98], which causes a change of

the optical length of the cavity per nanometer wavelength:

$$\frac{dl_{tm}}{d\lambda} = \frac{dn}{d\lambda} l_{tm} \approx 0.031 \frac{mm}{nm} \tag{4.5}$$

Considering the broad tunability of the laser system (∼130 nm), a change in cavity length up to 4 mm is observed between the two limit wavelengths. For this reason the diffraction grating has been mounted on a translation stage to change the optical cavity length and to establish a stable mode-locked operation. The temperature of the fiber, which depends on the pump power level, also influences the optical fiber length, thus the cavity length has also to be adapted for an increasing pump power level. The change of optical length according to the temperature can be quantified with 0.07 mm/K [119].

If the most energetic mode-locked pulse is observed on a more resolved time scale, it is possible to remark a pedestal around the mode-locked pulse peak. The peak and the pedestal have a FWHM duration of 32 ps and 1.6 ns, respectively, as shown in Figure 4.15. In order to estimate the ratio of energy between the short peaks and their pedestals, their integrals are compared with each other. To do that, the peaks have been cut out manually to observe only the pedestals, which are then fitted with a Gaussian profile. Only an energy level between 5% and 10% of the total energy is included in the mode-locked peak. This could be a cause for the lower conversion efficiency during supercontinuum generation (as it will be shown in the next chapter) compared to other results in literature.

The energy and the peak power levels of the pedestals depend on the Q-switch output pulse parameters from the fiber laser: the shorter the duration of the Q-switching pulses is, the smaller will be the number of mode-locked pulses underneath the Q-switch envelope. The mode-locked pulses will thus contain more energy in relation to the Q-switching output pulse energy, E_{QS}, given by Equation 4.4. In order to evaluate the pulse energy and the peak power for every single peak, a measure has been performed at an output power of $P_{out} = 15$ W and a Q-switch repetition rate of $\nu_{QS} = 60$ kHz,

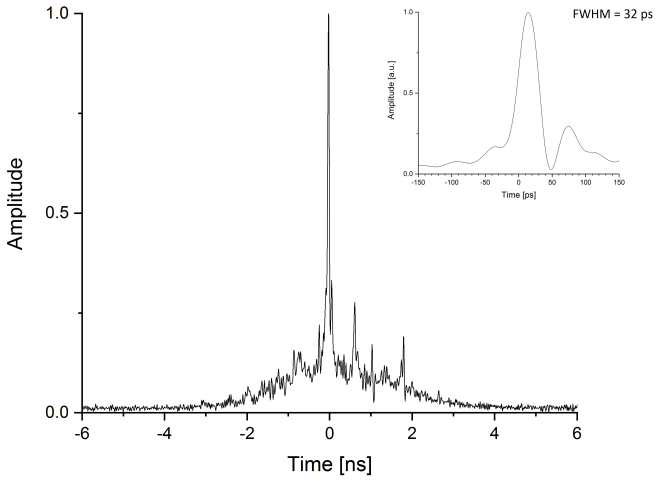

Figure 4.15: Temporal profile of the most energetic mode-locked pulse; *inset:* resolved measure of the peak on top of the pedestal indicating a FWHM duration of 32 ps.

corresponding to an average pulse train energy of $E_{QS} = 220$ μJ. In these conditions the duration of the Q-switch pulse envelope was around 50 ns, which corresponds to 6 mode-locked pulses underneath the Q-switch envelope. The energy for each pulse was determined by normalizing the integral of the pulse train to one. As a result, the integral of each single pulse just represented the part of the energy that it was carrying. Thus, by multipling the integral of each single pulse with $E_{QS} = 220$ μJ one is able to calculate the pulse energy. For the peak power, a calibration factor has been calculated by dividing the integral of the pulse train by the period, and multiplying this value for the total average output power. For both energies and peak powers, the results are shown in Figure 4.16. For the supercontinuum generation experiments, described in the following chapter, the most energetic mode-locked pulse (pulse #3) has an energy of 88 μJ and a peak power of $\sim$60 kW, 8 times more than pure Q-switch operation.

Figure 4.17 shows the Q-switched mode-locked slope curves for different

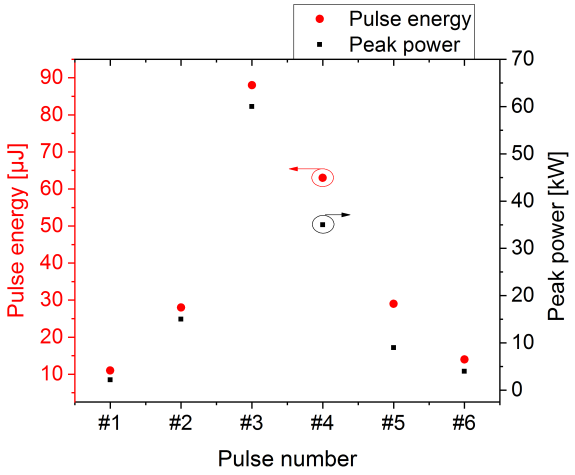

Figure 4.16: Energy and peak power for the different pulses in a Q-switched mode locked pulse train corresponding to an average output power of 15 W and a Q-switch repetition rate of 60 kHz. In these conditions only 6 peaks are included underneath the Q-switch envelope. The pulse #3 corresponds to the central peak.

Q-switch repetition rates as well as the continuous wave case for comparison. The maximum output power level has been 40 W, for Q-switch repetition rates of 150 kHz. At the output power level of 20 W and a Q-switch repetition rate of 50 kHz, the laser provided a Q-switching output energy of around 400 μJ. The lasing threshold is around 5 W, independent of the value of the Q-switch repetition rate and similar to the one for the continuous wave regime. The curves in the Q-switched mode-locking regime show a lower slope efficiency compared to the continuous wave performance and they have a rollover behavior at different pump power levels based on the Q-switch repetition rate. This effect looks similar to the one analyzed in the previous section and related to the ASE of the fiber laser. Nonetheless, the pump power thresholds for the same effect in Q-switched mode-locking are lower. The reason for this rollover could be non-linear effects in the silica fiber stimulated by the high peak intensities. Indeed, at high Q-switch output pulse energies, a Raman peak at $\sim$2100 nm can be observed in the laser spectrum

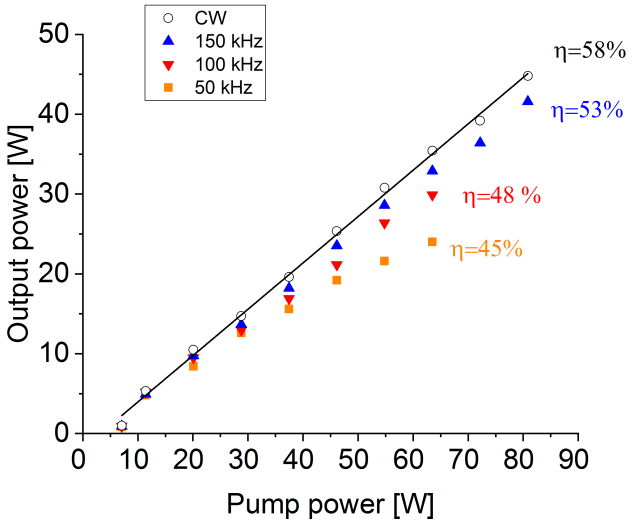

Figure 4.17: Output power versus launched pump power in Q-switched mode locking operation for different Q-switch repetition rates.

(Figure 4.18), most probably due to the high peak power of the mode-locked pulse. However, the percentage of the laser emission that is Raman-shifted resulted in a value around 5% which is then negligible. Another possible reason for the rollover of the output power could be the spectral cutting at the diffraction grating. The active mode-locking operation builds up the oscillation of many longitudinal modes after some round-trips, which broadens the lasing linewidth in Q-switched mode-locking operation. The diffraction grating is only highly reflective within a certain wavelength range. If it does not provide feedback of the coupled longitudinal modes at the wings of the lasing linewidth, their power is coupled out after each round-trip, causing losses.

4.5 Conclusion

In **continuous wave** the highest achieved output power has been 45 W with a slope efficiency of 58%. The measured beam quality, even at high output

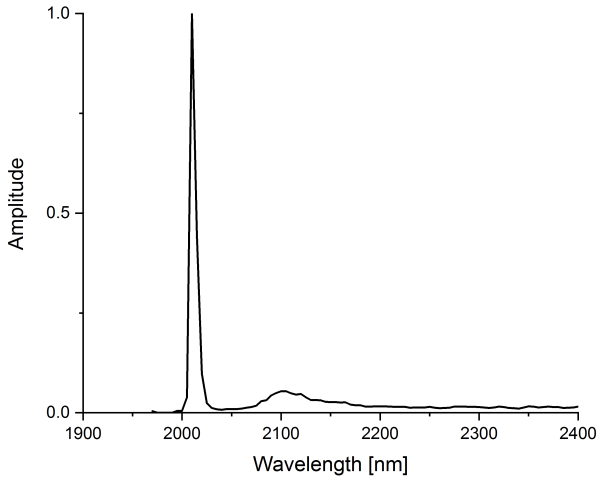

Figure 4.18: Spectrum of the Raman-shifted output radiation.

power levels, has been close to the diffraction limit, resulting in a value of $M^2 = 1.1$. Power scaling of the thulium-doped fiber laser was not the main objective of this thesis; however, the implementation of the end-caps at the active thulium-doped fiber increased the efficiency and the stability of the system and therefore higher output power and laser efficiency compared to the past results at ISL.

In **Q-switching** regime, the highest obtained output energy has been 330 μJ at a repetition rate of 60 kHz, a pulse duration of 48 ns and a peak power level of 7 kW approximately.

Unfortunately, there are no reports of **Q-switched mode-locked** lasers with thulium-doped fibers in order to compare the presented results. For the most energetic mode-locked pulse the energy and the peak power were 88 μJ and $\sim$60 kW, respectively. This measurement has been performed at an average output power level of 15 W. This value will be used for the supercontinuum generation experiments explained in the following chapter. This level of power will ensure a high enough peak power level to stimulate

supercontinuum generation effects and good stability of the pulses.

Chapter 5

Supercontinuum generation in fluoride fibers

In this chapter the results of mid-IR supercontinuum generation are presented. In the first part, an overview on the materials used for supercontinuum generation in the mid-IR is given. Second, a description of the cleaving and stripping procedures for the fluoride fibers is detailed. The optical setup with all the available materials and characterization tools is described. Finally, the results of the high power supercontinuum generation are presented, together with an analysis of the supercontinuum evolution depending on different parameters such as input power levels and pulse energies. These results are then compared to the scientific literature.

5.1 Materials

Two optical fiber materials have been investigated during this thesis work: ZBLAN and InF_3. The material absorption of the two fibers, is shown in Figure 5.1 (data from the manufacturer *Le Verre Fluoré*). The InF_3 fiber shows a much broader transmission bandwidth in the mid-IR compared to ZBLAN, but the absorption is higher in the range between 1 μm and 4 μm. One can define the absorption wavelength edge as the wavelength at which

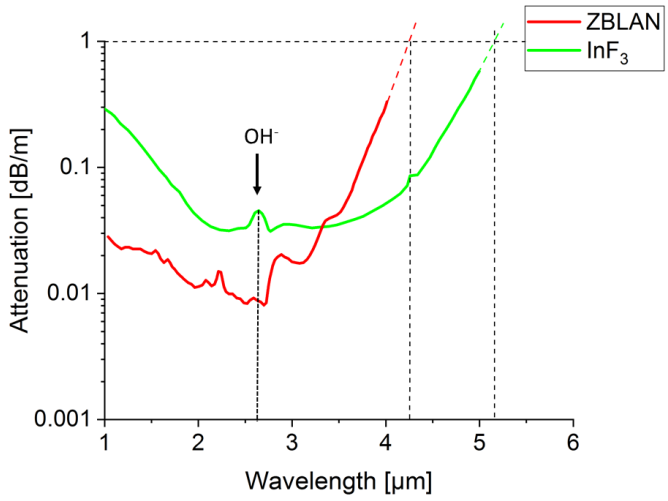

Figure 5.1: Material absorption of the available fluoride fibers.

the level of absorption is >1 dB/m. From Figure 5.1, this value is ∼4.5 μm for the ZBLAN fiber and ∼5 μm for the InF_3 fiber, respectively. These values could be obtained by extrapolating the absorption curves. The long wavelength absorption increase is mostly caused by the zirconium and aluminium of the glass composition [120]. Concerning the InF_3 fiber, the absorption wavelength edge is ∼5 μm caused by multiphonon absorption [120]. Both fibers exhibit a peak of the attenuation in the wavelength range around 3 μm, this increase is due to OH^- absorption, especially visible in the InF_3 fiber and rather suppressed in the ZBLAN fiber where other peaks are more relevant. This emphasizes the importance of keeping low the OH^- impurities during the manufacturing of these kind of glass materials. Table 5.1 summarizes the most important design parameters of the used fibers. The InF_3 has an inner and outer cladding diameter of 125 μm and 250 μm, respectively. The ZBLAN fiber has a double clad structure, with inner, second and outer cladding of 125 μm, 220 μm and 250 μm, respectively. The ZBLAN fiber has a normalized frequency parameter $V = 4.3$ at 2 μm, and so it exhibits a multi-mode propagation since up to four modes could propagate; on the

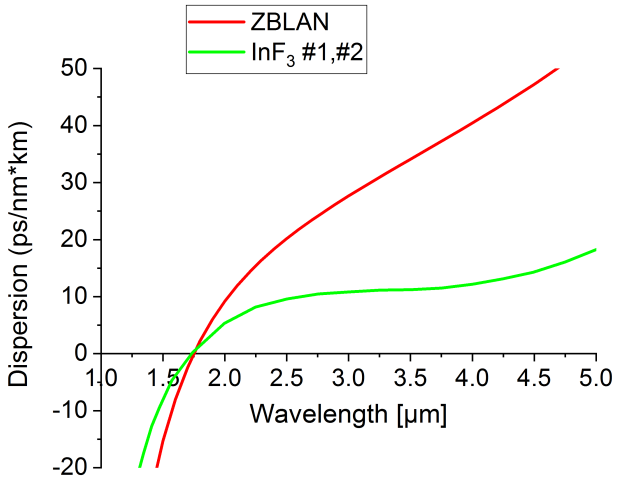

Figure 5.2: Dispersion parameter of the three fibers used for supercontinuum generation experiments (ZBLAN, InF_3 #1 and InF_3 #2) versus wavelength.

other hand the InF_3 fiber has a $V = 3.53$, which results in an almost complete single-mode propagation at the pump wavelength around 2 μm. In general, one could state that the higher the number of modes at the pump wavelength are, the easier the coupling of the pump light into the fiber core.

Taking the derivation from Section 3.5.2, the dispersion parameter curves of the fluoride fibers are shown in Figure 5.2. The data for the numerical simulation of the dispersion of ZBLAN and the InF_3 fibers have been taken from the manufacturer [96]. Furthermore, the influence of waveguide dispersion varies resulting in different zero-dispersion wavelengths, 1.65 μm and 1.75 μm for the ZBLAN and InF_3 fiber, respectively. These two values are lower than the pump laser wavelength around 2 μm, which allows to stimulate supercontinuum generation in the anomalous dispersion region.

To characterize the integrity of the fiber core, the manufacturer can use a non-destructive test of the fluoride optical fiber similar to the one described in [121]. In this publication, Gagnon *et al.* developed a technique

Fibers	Dimensions	NA	ZDW	IR screening
ZBLAN	12/125/220/250 μm (20 m)	0.23	1.65μm	NO
InF_3#1	7.5/125/250 μm (12.25 m)	0.3	1.75μm	NO
InF_3#2	7.5/125/250 μm (15 m)	0.3	1.75μm	YES

Table 5.1: Main parameters of the three fluoride fibers used for supercontinuum generation experiments in this thesis.

to perform the quality control of chalcogenide fibers because of their limited transparency in the visible spectral range. The experimental setup consists of an erbium-doped fluoride fiber laser at 2.8 μm and an InSb infrared camera. This camera allows the observation of defects along the optical fibers, giving visual indication of defective areas. The comparison with different images obtained with an added infrared spectral filters for removing the laser's contribution, allows the identification of different types of defects (e.g. scattering or absorbing defects) associated with localized thermal heating. The results of this screening technique allow then the selection of high-quality fibers for high power applications. Only one of the used fluoride fibers (InF_3#2) for supercontinuum generation has been tested with this method.

Based on Equation 3.34, the losses caused by bending have been calculated for the fundamental mode propagating in ZBLAN and InF_3 fibers. From the results, it can be said that bend losses are negligible (0.001 dB/m) for supercontinuum generation experiments in the range between 2 μm and 5 μm for bending radii greater than 10 cm.

5.2 Fluoride fiber cleaving

The cleaving procedure of fibers for mid-IR applications, as it is the case for fluoride fibers, is more sophisticated compared to standard fused silica fibers. The fluoride fibers require a careful handling for stripping and cleaving procedures due to their softness and fragility. In order to remove the coating,

Figure 5.3: Automated optical fiber cleaver Fujikura CT-106 with variable tension.

a stripper gel provided by the manufacturer has been used. This gel is a mixture of dichloromethane and methanol which melt the polymer of the coating. After stripping and cleaning, the end facets of the fiber are cleaved to obtain smooth and plain surfaces, to reduce the coupling losses and, as described in Section 4.3, to minimize the thermal induced damages at the optical fiber input and output surfaces. Due to the lower material strength compared to standard silica, fluoride glasses have to be cleaved with a cleaver (Figure 5.3) which allows to change different parameters such as the clamp force, the cleave tension and the starting position of the diamond cleave blade. The cleaver applies an axial tension to the fiber and then starts an automated scribe process using the diamond cleave blade. The tension causes the scribe to propagate perpendicular to the fiber, resulting in a smooth and clean cleaved surface. The key parameter for a successful cleave is the tension, which is dependent on the material, on the cladding diameter and whether the backstop is used or not. The micrometer backstop is a special mechanical

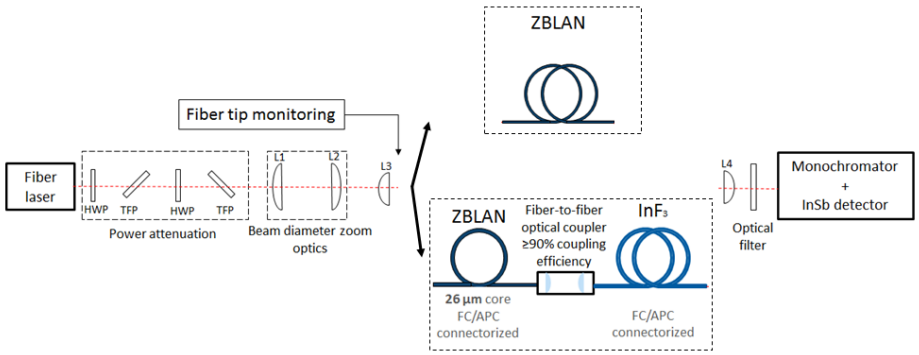

Figure 5.4: Schematic drawing of the experimental setup used to generate supercontinuum radiation.

tool embedded into the cleaver which prevents the fiber from deforming and moving when hit by the blade, allowing to reduce the tension needed to cleave by about 20%. Since the tension is lower, the crack propagates more slowly, resulting in smoother surfaces.

For ZBLAN and InF_3 fibers with a cladding diameter of 125 μm, a cleave tension between 90-100 g and 85-95 g has been used, respectively. In order to prevent any back-reflection inside the optical fiber during supercontinuum generation experiments, the cleave angle has been chosen between 4° and 8°.

5.3 Experimental setups for supercontinuum generation

Figure 5.4 shows the experimental setup used for investigating supercontinuum generation in fluoride fibers. It consists of a first stage to condition and attenuate the 2 μm free space propagating beam before coupling into the non-linear fiber. A polarization stage, made by a half wave plate and a thin film polarizer, reflects one polarization of the laser beam and transmits the other one for pumping the non-linear fiber. The actual attenuation stage allows the setting of the pump power level to inject into the fluoride fiber

so that the thulium fiber laser can work at stable high power operation with constant parameters. An afocal zoom optic, made by two AR-coated aspheric silica lenses with focal lengths 100 mm and 130 mm (L1 and L2 in Figure 5.4 respectively), increases the beam diameter of the pump beam for mode field adaptation to the fluoride fiber. A third lens is used to couple the laser beam into the fiber. It can be shown [122] that in the case of a collimated gaussian beam, the following relationship holds true for an efficient beam coupling:

$$\frac{f}{D} = \frac{\pi w}{4\lambda} \tag{5.1}$$

where D is the beam diameter and f the focal length of the lens. By choosing an injection AR-coated aspherical silica lens with the appropriate focal length (L3), considering the *MFD* of the non-linear fiber, and playing with the zooming factor, coupling efficiencies around 90% can be achieved[1]. A measurement of the beam waist after the focusing lens L3 has been performed using the knife edge technique as displayed in Figure 5.5. A sharp blade has been placed on a translation stage. For a fixed position of z, the blade is moved in the x-axis and the corresponding power values measured by the detector have been plotted. In order to obtain the beam radius w, the power values have been fitted with the following relation:

$$P = \frac{P_{max}}{2}\left[1 - \mathrm{erf}\left(\frac{\sqrt{2}(x)}{w}\right)\right] \tag{5.2}$$

where P_{max} is the maximum power, and erf is the standard error function. The operation is repeated for different values of z and all the beam radii are plotted and fitted with the relation:

$$w(z) = w_0\sqrt{1 + \left(\frac{\lambda z}{\pi w_0^2}\right)^2} \tag{5.3}$$

[1]The coupling efficiency is here defined as the ratio of input power and power coupled into the fiber.

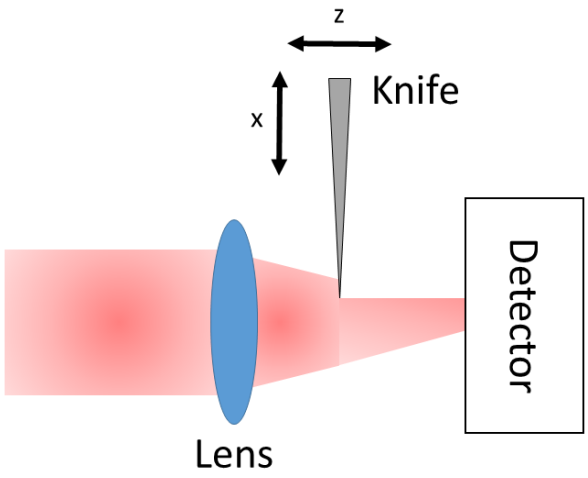

Figure 5.5: Schematic drawing from the top view of the knife-edge method. The knife is place on a translation stage which allows the movement in the x and z axis (where z is the axis of laser propagation).

The position of the three lenses is then adjusted until the expected waist value is obtained. Figure 5.6 shows the result of the measure and the related fitting. The minimum beam waist after L3 achieved is $\sim$11 μm, which is comparable to the *MFD* of the fundamental mode in ZBLAN fiber (10 μm).

In the case of the ZBLAN fiber, the 2 μm radiation is injected directly into the fiber. The bare ZBLAN fiber is placed on a six dimensional hexapod stage with a linear/angular accuracy of 0.1 μm/2 μrad, respectively. The input tip of the fiber is monitored with a USB microscope to check its integrity during the supercontinuum experiments. An image from the microscope at 95$\times$ of magnification is shown in Figure 5.7.

InF_3 fibers, on the other hand, is less mature from a technological point of view, and more sensitive to light propagation in the cladding compared to ZBLAN. For this reason, an intermediate 26 μm single mode ZBLAN fiber is used. The large core of this fiber allows for stable and reliable air-to-fiber coupling and also acts as a filter for the higher modes. The radiation from

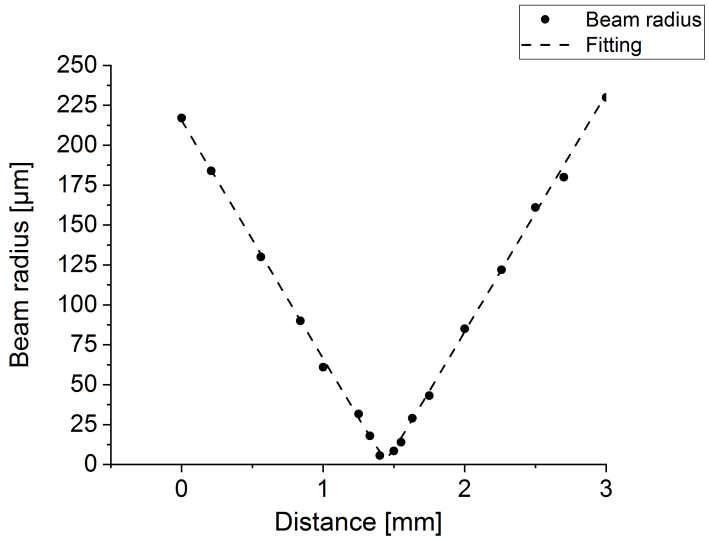

Figure 5.6: Beam radius measured at different z position after the focusing lens. The points are the fitted to find the minimum beam radius.

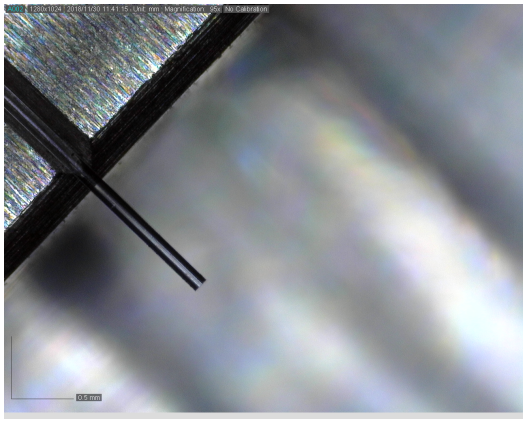

Figure 5.7: Image caught from the USB microscope used for monitoring the input tip of the fiber during supercontinuum generation experiments.

the ZBLAN fiber is then coupled into the core of the InF_3 fiber by means of a commercial fiber-to-fiber coupler allowing to interconnect two FC/APC connectorized fibers. It is made by two collimators with a system of lenses to reduce the optical aberrations. The fibers can be then aligned and the laser radiation can be focused with high precision, low coupling losses and high stability during all the experiment.

An uncoated calcium fluoride (CaF_2) lens with a focal length of 20 mm (L5) collects the supercontinuum output radiation before the measurement stage. Different optical long wave pass filters with 3 dB cut-off wavelengths around 2 μm, 2.65 μm, 3.1 μm and 3.5 μm are mounted on a filter wheel and can be inserted to measure the supercontinuum radiation in specified wavelength regions. The average power of the supercontinuum output radiation is measured with a thermal power meter capable of measure up to 50 W. The spectral power distribution is detected with a liquid-nitrogen cooled indium-antimonide (InSb) detector, which is sensitive in the wavelength range between 1 μm and 5.5 μm. This detector is placed at the output slit of a 320 mm focal length monochromator with a grating with 300 lines/mm blazed at 2 μm. The signal from the detector is treated by a preamplifier and a lock-in amplifier. The supercontinuum output radiation reaches the monochromator by means of a 500 μm diameter hollow-core fiber with a inner coating made by silver for total internal reflection. The complete measurement system (the silver hollow core fiber, the monochromator and the InSb detector) has been calibrated with a black body radiator emitting at 725 K. The calibration procedure with the results are described in Appendix A.

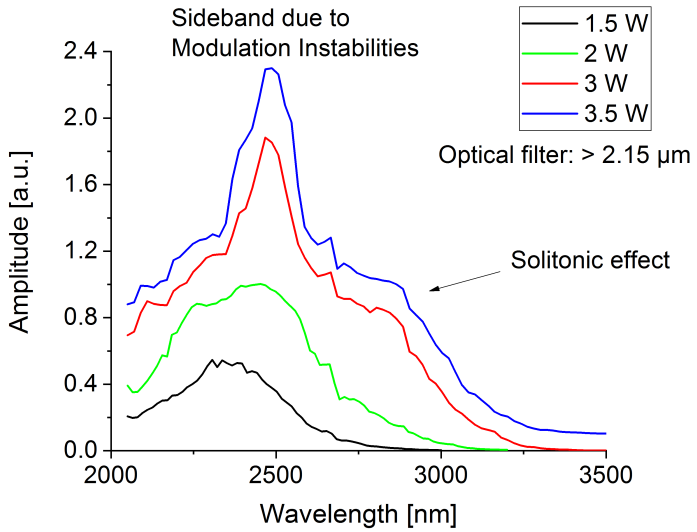

Figure 5.8: Evolution of the supercontinuum radiation for different pump power levels.

5.4 Characterization of the supercontinuum output performance

5.4.1 Evolution of the spectrum for different pump powers

Figure 5.8 shows the supercontinuum generation extension for different pump power levels. The 12 μm core ZBLAN fiber has been used for this study. The pump wavelength was located around 2 μm and the Q-switch repetition rate of the laser was 60 kHz. As explained in the previous chapters, when the optical fibers are pumped in their anomalous dispersion region, in the early stage of supercontinuum generation, modulation instabilities break-up the initial pulse into different sub-pulses in the time domain. In the spectral domain, the effect of modulation instabilities is the appearance of two side-bands around the pump. Figure 5.8 shows one of these side-bands in the region of wavelengths greater than the pump wavelength. The spectral

shift is strongly dependent on the pump power [123], this can be noticed by increasing the pump power. For higher levels of pump power, the supercontinuum generation becomes stronger. This broadening is mainly due to solitonic propagation.

5.4.2 Evolution of the spectrum for different Q-switch energies

As described in the previous chapter, the output characteristics of the Q-switched mode-locked pulses depend on the input power and the Q-switch repetition rates. It plays hence an important role for mid-IR supercontinuum generation what is the level of the Q-switch energy and how it is distributed among all the mode-locked pulses underneath the Q-switch envelope. To characterize this dependency of the supercontinuum radiation, the thulium doped fiber laser has been operated at constant output power level (15 W) and different Q-switch repetition rates (from 120 kHz to 65 kHz). The power after the power attenuation stage was around 2 W resulting in Q-switch pulse energies from 16 μJ to 30 μJ for the different Q-switch repetition rates. Figure 5.9 shows the results for the 20 m double cladding ZBLAN fiber. In this case, no optical filters have been used before the spectrometer. Since the spectra broaden only towards the longer wavelengths, which is expected for pumping well above the zero dispersion wavelength in the anomalous dispersion regime [124], all the graphs reported are plotted for wavelengths above 2 μm. As expected, the higher the level of energies, the broader and more efficient the supercontinuum extension is. For supercontinuum generation, a compromise between the highest E_{QS} achievable for enhancing the supercontinuum performance and a sufficiently low Q-switch energy to limit the probability of damaging has to be found. The long wavelength edges measured at 0.01 mW/nm are 3.1 μm, 3.3 μm, 3.4 μm, 3.5 μm at a Q-switch energy of 16 μJ, 18 μJ, 24 μJ, 30 μJ, respectively. Thus, for the rest of the experiments, a Q-switch repetition rate between 50 kHz and

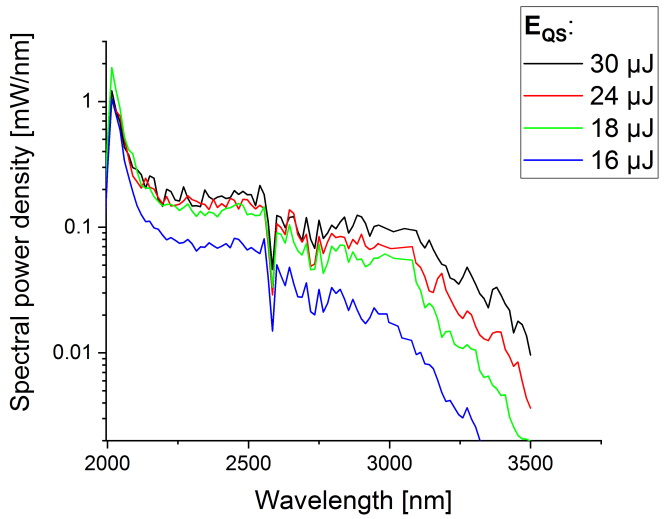

Figure 5.9: Supercontinuum output spectra for different Q-switch pulse energies.

65 kHz will be used. This value will ensure enough Q-switch energy for efficient supercontinuum generation and limit the probability of damaging of the fluoride fiber.

It should be noted that the ZBLAN fiber used during this experiment is multi-mode at the pump wavelength of 2 μm. In order to analyze how the higher modes of the fiber influence the supercontinuum conversion efficiency, the angular position of the input facet of the fiber has been changed. In this way, higher-modes can be excited without changing significantly the coupling efficiency. In these conditions, the supercontinuum conversion efficiency dropped about a factor two in terms of broadening and power efficiency, similarly to what is reported in [125]. For the rest of this thesis particular care has been adopted to ensure that most of the pump light is coupled into the fundamental transverse mode of the fiber.

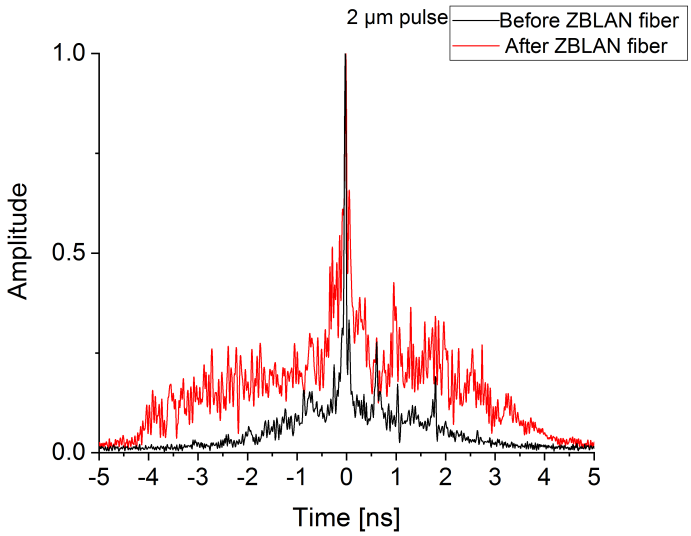

Figure 5.10: Temporal profiles of the most energetic Q-switched mode-locked pulse measured before and after the propagation in the ZBLAN fiber.

5.4.3 Analysis of the output pulses in the time-domain

The temporal profile evolution of the most energetic Q-switched mode-locked pulse at 2 μm before and after the propagation in the ZBLAN fiber has been analyzed. The results of these measures are displayed in Figure 5.10. It is possible to notice an increase of the duration of the pedestal from $\sim$1.6 ns to $\sim$4 ns, probably due to the dispersion. This measurement is in agreement with the description of the supercontinuum generation mechanisms for pulses in the range of nanosecond or picosecond duration, explained in Chapter 2. In the early stage of supercontinuum generation, the pulse first breaks up into a train of solitons through the modulation instabilities in the fiber. The generated solitons then experience frequency down-shifting due to the soliton self frequency shift, with the wavelength red-shifting in the spectrum.

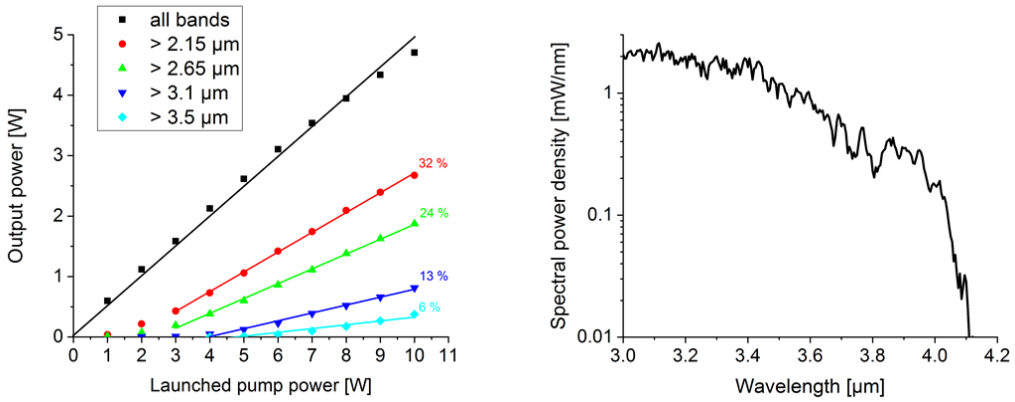

Figure 5.11: *left*: Output power versus launched pump power fro ZBLAN pumped by the fiber laser with a Q-switch output pulse energy of 200 μJ; *right*: Output spectrum at the highest output power level, measured after the optical long wave pass filter at 3 μm.

5.5 High power experiments

5.5.1 ZBLAN

For the 12 μm core ZBLAN fiber (whose main parameters are shown in Table 5.1), a length of 20 m has been used for high power supercontinuum generation. Two experiments are reported with this fiber and the results are displayed in Figure 5.11. In both cases the laser operated at a constant average output power of 20 W and a Q-switch repetition rate of 60 kHz corresponding to a Q-switch pulse energy of 330 μJ. In total, 5 W have been reached with 2.7 W/1.8 W/0.8 W/0.4 W beyond the corresponding optical long wave pass filters (2.15 μm, 2.65 μm/3.1 μm/3.5 μm) with a slope efficiency of 32%/24%/13%/6%, respectively. The coupling efficiency was estimated to be around 90%. A plot of the output spectrum at the highest output power after a 3 μm optical long wave pass filter is displayed in the right side of Figure 5.11. In this experiment, the long wavelength edge measured at 0.01 mW/nm of spectral intensity has been measured around

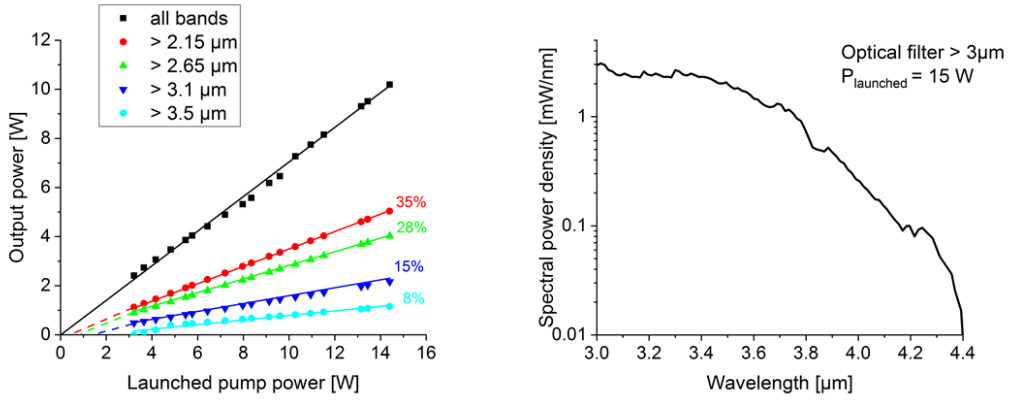

Figure 5.12: *left*: Output power versus launched pump power for ZBLAN fiber pumped by the fiber laser with a Q-switch output pulse energy of around 330 μJ; *right*: Output spectrum at the highest output power level, measured after the 3 μm optical long wave pass filter.

4.1 μm. The power scaling was limited by damage of the output end facet of the fiber. The reason might be connected to water absorption. Because of the hygroscopic nature of this type of fluoride glass, the water diffuses through the end facets. As the average output power in the mid-IR around 3 μm increases, the water absorption raises as well, leading to a localized temperature increase at the output facet. To avoid this limitation, the non-linear fiber has been protected by a sealed box with dry air flow.

Figure 5.12 shows the results with the new box in place. More than 10 W in all spectral bands have been reached with 5 W/3.8 W/2.3 W/1.1 W beyond the corresponding optical long wave pass filters (2.15 μm, 2.65 μm/3.1 μm/3.5 μm) with a slope efficiency of 35%/28%/15%/8%, respectively. Moreover, the long wavelength edge has been extended to 4.4 μm. The limitation in terms of output power scaling during this experiment was not the damage of the fiber end facet; in literature, it has been stated that a standard uncooled ZBLAN fiber can withstand around 15 W of average power, after that, active cooling must be applied [126]. For this reason the ZBLAN fiber was not pushed to its limit under these conditions, in order to preserve its integrity. However,

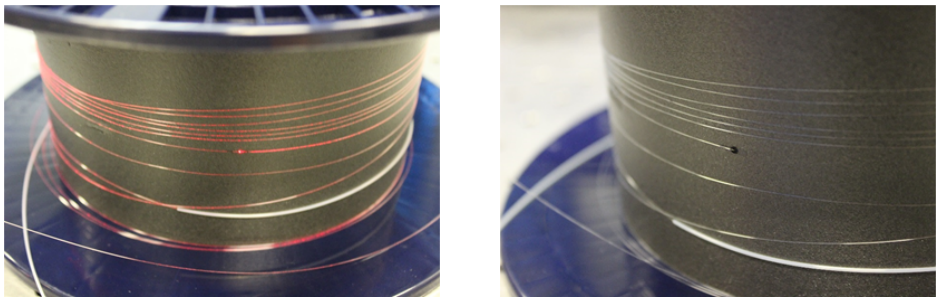

Figure 5.13: *left:* A check test of the InF_3 #1 fiber has been performed by injecting a HeNe laser emitting at 632.8 nm. A scattering point is visible along the fiber; *right:* Damaged InF_3 #1. The fiber damage occurred at the scattering point shown on the left side.

because of the fast increasing of the material absorption at wavelengths beyond 4 μm, significant changes of the long wavelength edge will probably not be possible.

5.5.2 InF_3

For mid-IR supercontinuum generation experiments with the InF_3 fibers (InF_3 #1 and InF_3 #2 whose main parameters are summarized in Table 5.1), the thulium-doped fiber laser has been operated at an output power level of 15 W and a Q-switch repetition rate of 60 kHz for stable operation, resulting in a total pulse energy of 250 μJ. A total coupling efficiency of ~90% between the first ZBLAN injection stage and the InF_3 fiber has been measured.

Before injecting the 2 μm pump, the presence of defects is monitored in InF_3 #1 by using a He-Ne laser. Several scattering points have been observed and marked. During the high power experiment with the 2 μm laser, the fiber has been monitored using a thermal camera. After a few minutes of pumping the fiber at 2 W, one marked point increased its temperature and the fiber got damaged. Figure 5.13 shows the InF_3 #1 fiber during the check test with the HeNe laser and after the high average power experiment. The fiber damage occured at the scattering point previously marked. The results of

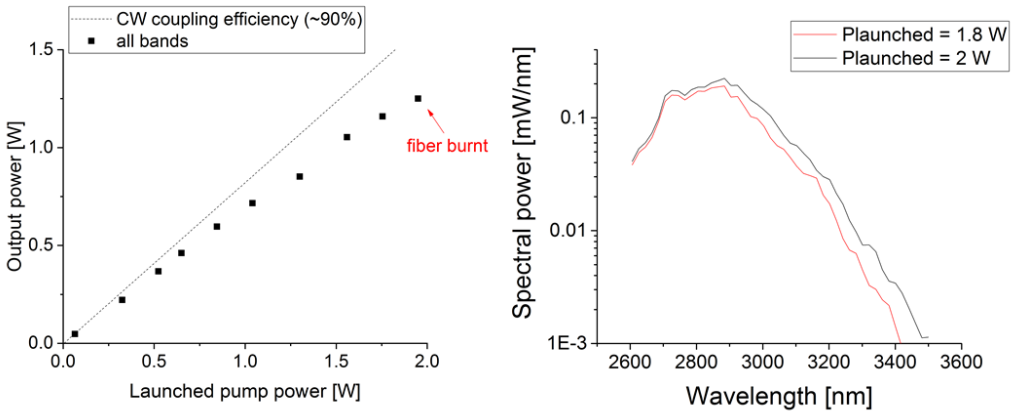

Figure 5.14: *left:* Output power versus launched pump power for InF_3 #1 fiber. During this experiment the fiber burnt at a launched pump power of 2 W; *right:* Spectral power density at two different launched pump powers.

the experiment are shown in Figure 5.14. In total, a supercontinuum output power level in all spectral bands of around 1.2 W has been obtained at a launched pump power of 2 W. The supercontinuum output spectra are shown for two different launched pump power levels. The long wavelength edge at 0.001 mW/nm has been 3.4 μm and 3.5 μm for a launched pump power of 1.8 W and 2 W, respectively. The limitation in terms of power scaling has been set by the fiber damages due to impurities, scattering and absorbing points incorporated along the fiber.

To ensure efficient heat dissipation, we repeated the experiment with the InF_3 #2 fiber placed on a duralumin water-cooled plate at 19 °C. Figure 5.16 shows the results achieved with InF_3 #2. Thanks to the lack of scattering centers along the fiber, together with the improved thermal handling, a pumping level up to 10 W was achieved and a general improvement has been obtained compared to the previous experiment. At a launched pump power of 10 W, 7 W in all spectral bands have been reached with 2 W and 34 mW for wavelengths above 2 μm and 3.5 μm, respectively. The spectra at different launched pump powers are displayed in the right part of Figure 5.16. At

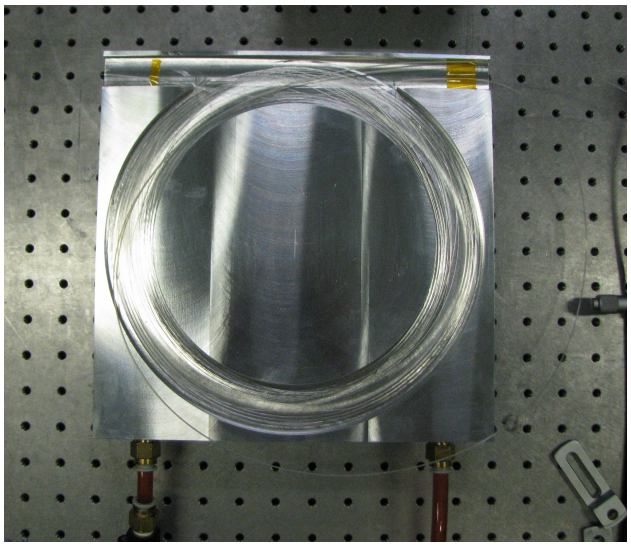

Figure 5.15: Duralumin cooling plate. The radius of curvature of the fiber is 10 cm which ensures negligible bend losses for wavelengths up to 5 μm.

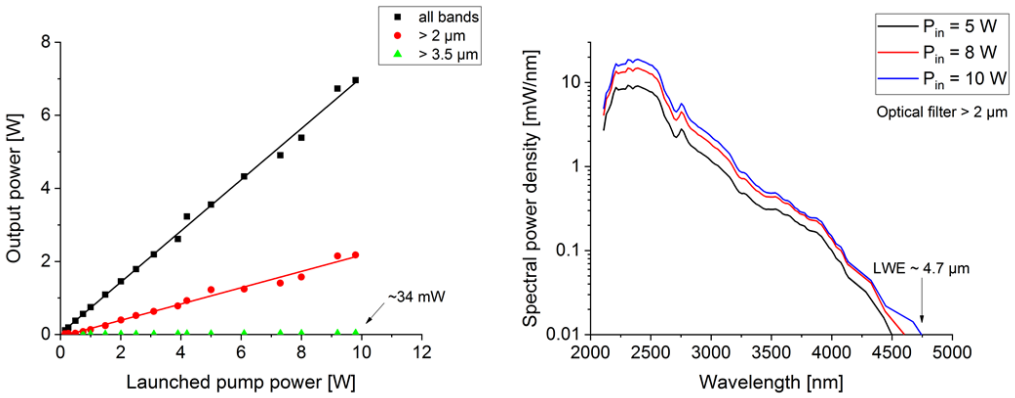

Figure 5.16: *left:* Supercontinuum output power versus launched pump power in all bands and with different optical long wave pass filters in the InF_3 #2 fiber; *right:* Output spectra for three different launched pump power levels.

the highest launched pump power (10 W) a long wavelength edge of 4.7 μm at a spectral power density of 0.01 mW/nm has been reached. The spectral distribution is not flat as expected. Also the overall conversion at highest wavelengths is lower compared to the one with the ZBLAN fiber or others experiments in literature [109]. It is very difficult to compare the achieved efficiency with results reported in literature because of different pump laser systems. There are no reports with Q-switched mode-locked laser systems used for supercontinuum generation experiments. In all the reported pump laser systems, the supercontinuum is generated by pulse trains with almost identical pulses. A possible explanation for the lower conversion efficiency could be that in the setup described in this thesis, the supercontinuum output radiation is a superposition of the different spectra generated by all the different mode-locked pulses. The pulses at the temporal edges of the Q-switch envelope are less energetic and intense than the ones close to the Q-switch peak, making the overall supercontinuum generation efficiency lower. Also the existence of the pulse pedestal could be one of the reason of lower conversion efficiency.

5.6 Conclusion

The highest achieved mid-IR supercontinuum output power in **ZBLAN** has been 10 W with a spectrum extension up to 4.4 μm. The fiber had a length of 20 m. An output average power of 5 W/3.8 W/2.3 W/1.1 W has been reached beyond the corresponding optical long wave pass filters (2.15 μm/2.65 μm/3.1 μm/3.5 μm) with a slope efficiency of 35%/28%/15%/8%, respectively. The achieved conversion efficiencies in this thesis have been defined as the slope of the output power beyond the optical long pass wavelength filters versus the launched pump power. In literature, usually the ratio of the output power beyond the filters to the output power level in all spectral bands is used to evaluate the supercontinuum conversion efficiency.

Using this definition, in total 50%/38%/23%/11% of the transmitted supercontinuum radiation in all spectral bands have been converted beyond the wavelength of 2.15 μm/2.65 μm/3.1 μm/3.5 μm, respectively. The highest reported supercontinuum output power level from a ZBLAN reported in literature has been 30 W [105]. In this experiment the ZBLAN fiber has been fusion-spliced to the pump source leading to a high and stable coupling efficiency and a AlF_3 end cap has been implemented to the end tip of the ZBLAN fiber to prevent water diffusion. This reduces the re-absorption at longer wavelengths during supercontinuum generation. If these modifications would be implemented in the setup presented in thesis, much higher output power level and conversion would be feasible. Moreover, if only the most-energetic Q-switched mode-locked pulse would be used solely for pumping the fluoride fibers, much higher conversion efficiencies would be feasible as well.

The results obtained with the $\mathbf{InF_3}$ fiber in this thesis resulted in a total average supercontinuum output power of 7 W with a conversion efficiency of 29% for wavelengths from 2.1 μ to 4.7 μm. The fiber was IR screened by the manufacturer in order to find and avoid the presence of defects or absorbing points. Moreover, to increase the heat dissipation along the fiber, it has been placed on a dural cooled-plate. The highest reported average output power level in InF_3 fibers has been achieved by Wu *et al.* [109]. In this publication, a maximum supercontinuum average output power of 11.3 W has been demonstrated with a spectrum extension up to 4.7 μm with the highest conversion efficiency of 66.5%. As in the case of the ZBLAN fiber, also during this experiment the InF_3 fiber has been fusion-fusion spliced with the pump source to increase the coupling efficiency and equipped with an end cap made of aluminum fluoride.

Chapter 6

Conclusion and Outlook

In this thesis a thulium-doped fiber laser has been built and characterized in continuous wave, Q-switching and Q-switched mode-locking regime. In **continuous wave** operation, as much as 45 W have been reached with a slope efficiency of 58%. The implementation of two fused-quartz end-caps fusion spliced at the extremities of the active-fiber, improved the thermal management and the overall stability of the entire laser system in all the mentioned regimes of operation, allowing for higher pump powers. **Q-switching** resulted in an output power level of 40 W with variable Q-switch repetition rates. The highest output power energy has been 350 μJ with a pulse width of 48 ns leading to a peak power of 7 kW. In **Q-switched mode-locking**, the additional modulation of the mode-locked pulse train by the Q-switch envelopes enabled very high mode-locked pulse energies. The most energetic mode-locked pulse used during the supercontinuum generation experiments had an energy of 88 μJ and a peak power of $\sim$60 kW, 8 times more than pure Q-switch operation. Typically, for obtaining such high peak power levels, seed laser diodes with at least three amplification stages have to be used [81]. The Q-switched mode-locked pulse had a temporal shape of a short peak on top of a pedestal with pulse duration in the range of 30 ps and 1.6 ns, respectively. The fiber laser output performance concerning the beam quality was similar for all the three operation regimes of the laser, resulting

in a M^2 value of 1.1, close to the diffraction limit. This fiber laser has been used to pump fluoride optical fibers for supercontinuum generation in the range from 2 μm to 5 μm. The pump laser was used only in the Q-switched mode-locking regime because it was the only operation regime able to ensure sufficient peak power levels for the wavelength extension. The experiments have been focused on the fluoride materials ZBLAN and InF_3. The investigated ZBLAN fiber had a core diameter of 12 μm, an NA of 0.23 and a total length of 20 m. More than 10 W in all spectral bands have been reached. The highest supercontinuum conversion efficiency during this investigation with this ZBLAN fiber resulted in 35%/28%/15%/8% of the transmitted supercontinuum output radiation that has been converted beyond the wavelength of 2.15 μm/2.65 μm/3.1 μm/3.5 μm, respectively, with an output spectrum extending up to 4.4 μm. The highest quality InF_3 optical fiber had a core diameter of 7.5 μm and an NA of 0.3. A new design of a injection system, consisting of a large core diameter ZBLAN optical fiber and a commercial fiber-to-fiber coupler, allowed to enhance the thermo-mechanical stability of the fiber. The supercontinuum generated in the InF_3 fiber showed an output spectrum spanning up to around 4.7 μm with an output power level of 7 W in all spectral bands. This was the first Watt-level demonstration in an InF_3 fiber pumped by a single-oscillator.

For future work, there are many opportunities to further improve the setup while maintaining a single-oscillator laser pump system. In particular, an all-fiber pump laser seems to be feasible, especially because of the ongoing research activities on pump combiners, fiber-coupled modulators and cavity end mirrors in the form of fiber Bragg gratings at ISL. The use of this components will allow to deliver the laser radiation directly via an optical fiber. This could improve the mid-IR supercontinuum generation by directly splicing the input face of the fluoride fiber onto a passive silica fiber and thus increase the coupling efficiency and the overall stability. However, the great discrepancies of the glass transition temperature between silica fibers (1215

°C) and fluoride fibers (∼180 - 300 °C) makes fusion splicing very challenging [104].
The splicing between silica and fluoride fiber can also prevent the diffusion of water into the input tip of the fiber, which causes optical damages during high power operation. On the other fiber extremity, this can be limited splicing an AlF_3 end-cap which is more chemically resistant against water. It should be noted that in this thesis, the water diffusion has been limited inserting the tip of the fiber into a sealed box with dry air.
Another limiting aspect for high average power supercontinuum generation is the cooling of the fluoride fiber. In this thesis a water-cooled duralumin plate has been used to reduce the thermal-related problems; this system has to be improved to uniformly cool the fiber all over its entire length.
The supercontinuum output performance with the InF_3 fiber has been relatively lower concerning the broadening conversion and flatness of the spectrum compared to the ZBLAN fiber results. Further investigations have to be performed in order to understand this behavior.

Finally, it could be interesting to splice the InF_3 fiber onto the output end facet of the ZBLAN fiber to further extend the long wavelength edge of the supercontinuum radiation generated by the ZBLAN fiber.

Appendix A

Calibration of the optical spectrum analyzer

As mentioned in Section 4.1, the mid-IR supercontinuum output radiation has been measured in terms of spectral power distribution with a self-built spectrometer, including a monochromator and a InSb detector. The sensitivity of this detector with a field of view (FOV) of 60° is shown in Figure A.1. The spectrometer has been calibrated with a black body radiator, operated at an absolute temperature of 725 K. The right side of the figure shows the Planck spectrum for that temperature, calculated with:

$$P(\lambda) = \frac{2\pi hc^2}{\lambda^5(e^{\frac{hc}{\lambda kT}} - 1)} \tag{A.1}$$

The black curve in the graph presents the measured values from the spectrometer. The measurement of the radiation from the black body radiator has been conducted with an optical long wave pass filter between the emitter and the spectrometer for suppressing the detection of the second diffraction order. Two optical filters at 2.1 μm and 3.4 μm have been used for that purpose. Up to 3.5 μm, the spectrum is recorded only with the optical filter at 2.15 μm and corrected with the measured transmission filter curve of the filter. Beyond 3.5 μm, the filter at 2.65 μm has been implemented. The wavelength region beyond 5.5 μm did not play an important role in this

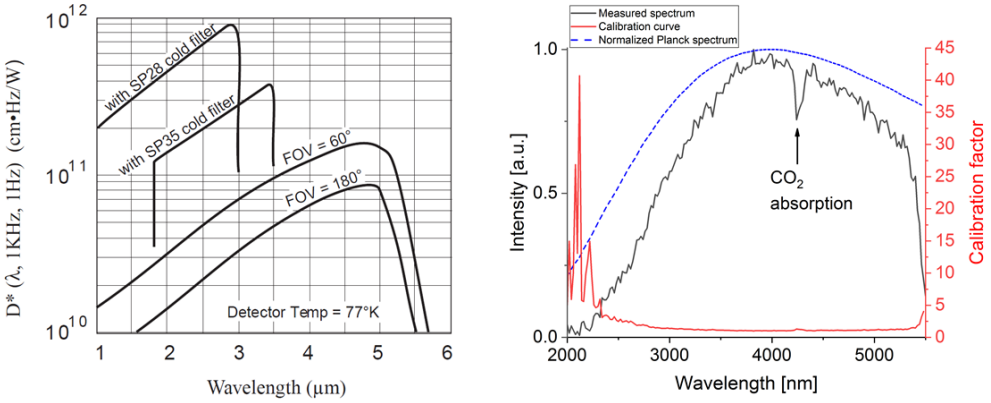

Figure A.1: *left:* Detectivity of the used InSb detector with field of view of 60° [127]; *right:* Measured signal from the monochromator for an input radiation from a black body radiator emitting at 725 K and the related calibration curve.

thesis. The measured curve in the right part of Figure A.1 shows a local minimum in the wavelength around 4.3 μm due to CO_2 absorption. In order to reduce this effect, the inside of the monochromator has been filled with Nitrogen gas.

Bibliography

[1] T. Morioka, K. Mori, S. Kawanishi, and M. Saruwatari. "Multi-WDM-channel, Gbit/s pulse generation from a single laser source utilizing LD-pumped supercontinuum in optical fibers". *IEEE Photonics Technology Letters*, 6(3):365–368, March 1994.

[2] R. Thapa, D. Rhonehouse, D. Nguyen, K. Wiersma, C. Smith, J. Zong, and A. Chavez-Pirson. "Mid-IR Supercontinuum Generation in Ultra-Low Loss, Dispersion-Zero Shifted Tellurite Glass Fiber With Extended Coverage Beyond 4.5 μm". *Proc SPIE*, 8898:08, 10 2013.

[3] J. Mandon, E. Sorokin, I. T. Sorokina, G. Guelachvili, and N. Picqu. "Supercontinua for high-resolution absorption multiplex infrared spectroscopy". *Optics Letters*, 33(3):285, Jan 2008.

[4] R. R. Anderson, W. Farinelli, H. Laubach, D. Manstein, A. N. Yaroslavsky, J. Gubeli III, K. Jordan, G. R. Neil, M. Shinn, W. Chandler, G. P. Williams, S. V. Benson, D. R. Douglas, and H.F. Dylla. "Selective photothermolysis of lipid-rich tissues: A free electron laser study". *Lasers in Surgery and Medicine*, 38(10):913–919, 2006.

[5] D. Huang, E.A. Swanson, C.P. Lin, J.S. Schuman, W.G. Stinson, W. Chang, M.R. Hee, T. Flotte, K. Gregory, and C.A. Puliafito. "Optical coherence tomography". *Science*, 254(5035):1178–1181, 1991.

[6] A. Labruyre, A. Tonello, V. Couderc, G. Huss, and P. Leproux. Compact supercontinuum sources and their biomedical applications. *Optical Fiber Technology*, 18(5):375 – 378, 2012. Fiber Supercontinuum sources and their applications.

[7] A. Sincore, J. D. Bradford, J. Cook, L. Shah, and M. C. Richardson. "High Average Power Thulium-Doped Silica Fiber Lasers: Review of Systems and Concepts". *IEEE Journal of Selected Topics in Quantum Electronics*, 24(3):1–8, May 2018.

[8] B. E. A. Saleh and M. C. Teich. *Fundamentals of photonics; 2nd ed.* Wiley, 2007.

[9] A. Liu and K. Ueda. "The absorption characteristics of circular, offset, and rectangular double-clad fibers". *Optics Communications*, 132(5):511 – 518, 1996.

[10] D. Kouznetsov, J. V. Moloney, and E. Wright. "Efficiency of pump absorption in double-clad fiber amplifiers in fiber with circular symmetry". *Journal of The Optical Society of America B-optical Physics*, 18:743–749, 06 2001.

[11] `https://www.rp-photonics.com/double_clad_fibers.html`.

[12] S.D. Jackson. "The spectroscopic and energy transfer characteristics of the rare earth ions used for silicate glass fibre lasers operating in the shortwave infrared". *Laser & Photonics Reviews*, 3(5):466–482.

[13] K. Barat. "ANSI Laser standards, Education, Research, Development or Testing", 2014.

[14] L. F. Johnson, J. E. Geusic, and L. G. Van Uitert. "Coherent oscillations from Tm^{3+}, Ho^{3+}, Yb^{3+} and Er^{3+} ions in yttrium aluminum garnet". *Applied Physics Letters*, 7(5):127–129, 1965.

[15] T. S. McComb, R. A. Sims, C. C. C. Willis, P. Kadwani, L. Shah, and M. Richardson. "Atmospheric transmission testing using a portable, tunable, high power thulium fiber laser system". In *Conference on Lasers and Electro-Optics 2010*, page JThJ5. Optical Society of America, 2010.

[16] P. Sprangle, A. Ting, J. Penano, R. Fischer, and B. Hafizi. "Incoherent combining and atmospheric propagation of high-power fiber lasers for directed-energy applications". *IEEE Journal of Quantum Electronics*, 45(2):138–148, Feb 2009.

[17] I. Mingareev, N. Gehlich, T. Bonhoff, A. Abdulfattah, A. M. Sincore, P. Kadwani, L. Shah, and M. Richardson. "Principles and applications of trans-wafer processing using a 2-μm thulium fiber laser". *The International Journal of Advanced Manufacturing Technology*, 84(9):2567–2578, Jun 2016.

[18] I. Mingareev, F. Weirauch, A. Olowinsky, L. Shah, P. Kadwani, and M. Richardson. "Welding of polymers using a 2 μm thulium fiber laser". *Optics & Laser Technology*, 44:20952099, 10 2012.

[19] I. Moskalev, S. Mirov, M. Mirov, S. Vasilyev, V. Smolski, A. Zakrevskiy, and V. Gapontsev. "140 W Cr:ZnSe laser system". *Opt. Express*, 24(18):21090–21104, Sep 2016.

[20] C. Kieleck, A. Berrou, B. Donelan, B. Cadier, T. Robin, and M. Eichhorn. "6.5 W $ZnGeP_2$ OPO directly pumped by a Q-switched Tm^{3+}-doped" single-oscillator fiber laser. *Opt. Lett.*, 40(6):1101–1104, Mar 2015.

[21] W. Koechner. *Solid-state laser engineering*. Springer, 2006.

[22] S.D. Jackson. "Cross relaxation and energy transfer upconversion processes relevant to the functioning of 2 μm Tm^{3+}-doped silica fibre lasers". *Optics Communications*, 230:197–203, 01 2004.

[23] J. Ganem, J. Crawford, P. Schmidt, N. W. Jenkins, and S. R. Bowman. "Thulium cross-relaxation in a low phonon energy crystalline host". *Physical Review B*, 66:245101, Dec 2002.

[24] L. B. Shaw, R. S. F. Chang, and N. Djeu. "Measurement of up-conversion energy-transfer probabilities in Ho:$Y_3Al_5O_{12}$ and Tm:$Y_3Al_5O_{12}$". *Physical Review B*, 50:6609–6619, Sep 1994.

[25] D. A. Simpson, G. W. Baxter, S. F. Collins, W. E. K. Gibbs, W. Blanc, B. Dussardier, and G. Monnom. "Energy transfer upconversion in Tm^{3+}-doped silica fiber". *Journal of Non Crystalline Solids*, 352(2):136–141, Feb 2006.

[26] D. F. de Sousa and L. A. O. Nunes. "Microscopic and macroscopic parameters of energy transfer between Tm^{3+} ions in fluoroindogallate glasses". *Phys. Rev. B*, 66:024207, Jul 2002.

[27] Dexter D. L. "A theory of sensitized luminescence in solids". *The Journal of Chemical Physics*, 21(5):836–850, 1953.

[28] Arai K., Namikawa H., Kumata K., Honda T., Ishii Y., and Handa T. "Aluminum or phosphorus codoping effects on the fluorescence and structural properties of neodymiumdoped silica glass". *Journal of Applied Physics*, 59(10):3430–3436, 1986.

[29] B. Faure, W. Blanc, B. Dussardier, and G. Monnom. "Improvement of the Tm^{3+}:$^3H_4$ level lifetime in silica optical fibres by lowering the local phonon energy". *Journal of Non-Crystalline Solids*, 353:2767–2773, July 2007.

[30] S. D. Jackson and S. Mossman. "Efficiency dependence on the Tm^{3+} and Al^{3+} concentrations for Tm^{3+}-doped silica double-clad fiber lasers". *Applied Optics*, 42(15):2702–2707, May 2003.

[31] C. A. Millar, S. R. Mallinson, B. J. Ainslie, and S. P. Craig. "Photochromic behaviour of thulium-doped silica optical fibres". *Electronics Letters*, 24(10):590–591, May 1988.

[32] G. Frith, A. Carter, B. Samson, J. Faroni, K. Farley, K. Tankala, and G. E. Town. "Mitigation of photodegradation in 790 nm-pumped Tm-doped fibers". volume 7580, pages 7580 – 7580 – 9, 2010.

[33] W. S. Brocklesby, A. Mathieu, R. S. Brown, and J. R. Lincoln. "Defect production in silica fibers doped with Tm^{3+}". *Optics Letters*, 18(24):2105–2107, Dec 1993.

[34] M. M. Broer, D. M. Krol, and D. J. DiGiovanni. "Highly nonlinear near-resonant photodarkening in a thulium-doped aluminosilicate glass fiber". *Optics Letters*, 18(10):799–801, May 1993.

[35] S. D. Agger and J. H. Povlsen. "Emission and absorption cross section of thulium doped silica fibers". *Optics Express*, 14(1):50–57, Jan 2006.

[36] D. Ristau. *Laser-induced damage in optical materials*. CRC Press, 2016.

[37] Shashi P. Karna and Alan T. Yeates. *Nonlinear Optical Materials: Theory and Modeling*, chapter 1, pages 1–22.

[38] A. Dhollande. Private communication, 2018.

[39] U. Keller, K. J. Weingarten, F. X. Kartner, D. Kopf, B. Braun, I. D. Jung, R. Fluck, C. Honninger, N. Matuschek, and J. Aus der Au. "Semiconductor saturable absorber mirrors (SESAMs) for femtosecond

to nanosecond pulse generation in solid-state lasers". *IEEE Journal of Selected Topics in Quantum Electronics*, 2(3):435–453, Sep. 1996.

[40] Vladimir Kalosha, Liang Chen, and Xiaoyi Bao. Feasibility of kerr-lens mode locking in fiber lasers. *Proceedings of SPIE - The International Society for Optical Engineering*, 7099, 06 2008.

[41] R. C. Sharp, D. E. Spock, N. Pan, and J. Elliot. "190-fs passively mode-locked thulium fiber laser with a low threshold". *Opt. Lett.*, 21(12):881–883, Jun 1996.

[42] M. A. Solodyankin, E. D. Obraztsova, A. S. Lobach, A. I. Chernov, A. V. Tausenev, V. I. Konov, and E. M. Dianov. "Mode-locked 1.93 μm thulium fiber laser with a carbon nanotube absorber". *Opt. Lett.*, 33(12):1336–1338, Jun 2008.

[43] H. Ahmad, K. Thambiratnam, F. D. Muhammad, M. Z. Zulkifli, A. Z. Zulkifli, M. C. Paul, and S. W. Harun. "Q-switching and mode-locking in highly doped Zr_2O_3 Al_2O_3 Er_2O_3-doped fiber lasers using graphene as a saturable absorber". *IEEE Journal of Selected Topics in Quantum Electronics*, 20(1):9–16, Jan 2014.

[44] P. Hübner, C. Kieleck, S. D. Jackson, and M. Eichhorn. "High-power actively mode-locked sub-nanosecond Tm^{3+}-doped silica fiber laser". *Opt. Lett.*, 36(13):2483–2485, Jul 2011.

[45] Yung-Fu Chen, Jian-Lung Lee, Hung-Dau Hsieh, and Sheng-Wei Tsai. "Analysis of passively Q-switched lasers with simultaneous mode locking". *IEEE Journal of Quantum Electronics*, 38(3):312–317, March 2002.

[46] Jiaqun Zhao, Ying Li, Su Zhang, Li Li, and Xinlu Zhang. "Diode-pumped actively Q-switched Tm:YAP/$BaWO_4$ intracavity Raman laser". *Opt. Express*, 23(8):10075–10080, Apr 2015.

[47] P. Datta, S. Mukhopadhyay, S. Das, L. Tartara, A. Agnesi, and V. Degiorgio. "Enhancement of stability and efficiency of a nonlinear mirror mode-locked Nd:YVO_4 oscillator by an active Q-switch". *Optics express*, 12:4041–6, 09 2004.

[48] J. K. Jabczyński, W. Zendzian, and J. Kwiatkowski. "Q-switched mode-locking with acousto-optic modulator in a diode pumped Nd:YVO_4 laser". *Opt. Express*, 14(6):2184–2190, Mar 2006.

[49] N. Kishi, J. N. Carter, R. Mottahedeh, P. R. Morkel, R. G. Smart, A. J. Seeds, J. S. Roberts, C. C. Button, D. N. Payner, A. C. Tropper, and D. C. Hanna. "Actively mode-locked and passively Q-switched operation of thulium-doped fibre laser using multiquantum well asymmetric Fabry-Perot modulator". *Electronics Letters*, 28(2):175–177, Jan 1992.

[50] J. Lee, J. Koo, You Min C., P. Debnath, Y.-W. Song, and J. Lee. "Experimental investigation on a Q-switched, mode-locked fiber laser based on the combination of active mode locking and passive Q-switching". *Journal of the Optical Society of America B*, 29:1479–1485, 06 2012.

[51] T. Tanbun-Ek, R. Pathak, Z. Xu, H. Winhold, F. Zhou, M. Peters, D. Schleuning, and B. Acklin. "Improved long wavelength 14xx and 19xx nm InGaAs/InP lasers". volume 9733, pages 9733 – 9733 – 7, 2016.

[52] S. D. Jackson and T. A. King. "Theoretical modeling of Tm-doped silica fiber lasers". *J. Lightwave Technol.*, 17(5):948, May 1999.

[53] G. P. Frith, D. G. Lancaster, and S. D. Jackson. "85 W Tm^{3+}-doped 2 μm fibre laser pumped at 793 nm". In *2005 IEEE LEOS annual meeting conference proceedings*, pages 746–747, United States, 2005. Institute of Electrical and Electronics Engineers (IEEE).

[54] P. F. Moulton, G. A. Rines, E. V. Slobodtchikov, K. F. Wall, G. Frith, B. Samson, and A. L. G. Carter. "Tm-doped fiber lasers: Fundamentals and power scaling". *IEEE Journal of Selected Topics in Quantum Electronics*, 15(1):85–92, Jan 2009.

[55] T. Ehrenreich, R. Leveille, I. Majid, and K. Tankala. "1-kW, All-Glass Tm: fiber laser". In *Proc. SPIE*, volume 7580, 2010.

[56] T. Walbaum, M. Heinzig, T. Schreiber, R. Eberhardt, and A. Tünnermann. "Monolithic thulium fiber laser with 567 W output power at 1970 nm". *Opt. Lett.*, 41(11):2632–2635, Jun 2016.

[57] N. Simakov, A. V. Hemming, A. Carter, K. Farley, A. Davidson, N. Carmody, M. Hughes, J. M. O. Daniel, L. Corena, D. Stepanov, and J. Haub. "Design and experimental demonstration of a large pedestal thulium-doped fibre". *Opt. Express*, 23(3):3126–3133, Feb 2015.

[58] Ashraf El-Sherif and T.A. King. Analysis and optimization of q-switched operation of a tm3+-doped silica fiber laser operating at 2 μm. *Quantum Electronics, IEEE Journal of*, 39:759 – 765, 07 2003.

[59] Pankaj Kadwani, Norbert Modsching, Andrew Sims, Lasse Leick, Jes Broeng, Lawrence Shah, and Martin Richardson. Q-switched thulium-doped photonic crystal fiber laser. *Optics letters*, 37:1664–6, 05 2012.

[60] M. Eichhorn and S. D. Jackson. "High-pulse-energy actively Q-switched Tm^{3+}-doped silica 2 μm fiber laser pumped at 792 nm". *Opt. Lett.*, 32(19):2780–2782, Oct 2007.

[61] F. Stutzki, F. Jansen, C. Jauregui, J. Limpert, and A. Tünnermann. "2.4 mJ, 33 W Q-switched Tm-doped fiber laser with near diffraction-limited beam quality". *Opt. Lett.*, 38(2):97–99, Jan 2013.

[62] Ke Yin, Bin Zhang, Weiqiang Yang, He Chen, Shengping Chen, and Jing Hou. "Flexible picosecond thulium-doped fiber laser using the active mode-locking technique". *Opt. Lett.*, 39(14):4259–4262, Jul 2014.

[63] M. Jiang and P. Tayebati. "Stable 10 ns, kilowatt peak-power pulse generation from a gain-switched Tm-doped fiber laser". *Opt. Lett.*, 32(13):1797–1799, Jul 2007.

[64] J. Swiderski, M. Michalska, and G. Maze. "Mid-IR supercontinuum generation in a ZBLAN fiber pumped by a gain-switched mode-locked Tm-doped fiber laser and amplifier system". *Opt. Express*, 21(7):7851–7857, Apr 2013.

[65] Yulong Tang and Jianqiu Xu. "Hybrid-pumped gain-switched narrow-band thulium fiber laser". *Applied Physics Express*, 5(7):072702, jun 2012.

[66] N. Simakov, A. Hemming, S. Bennetts, and J. Haub. "Efficient, polarised, gain-switched operation of a Tm-doped fibre laser". *Opt. Express*, 19(16):14949–14954, Aug 2011.

[67] Jiang Liu, Jia Xu, Kun Liu, Fangzhou Tan, and Pu Wang. "High average power picosecond pulse and supercontinuum generation from a thulium-doped, all-fiber amplifier". *Opt. Lett.*, 38(20):4150–4153, Oct 2013.

[68] F. Stutzki, C. Gaida, M. Gebhardt, F. Jansen, A. Wienke, U. Zeitner, F. Fuchs, C. Jauregui, D. Wandt, D. Kracht, J. Limpert, and A. Tünnermann. "152 W average power Tm-doped fiber CPA system". *Opt. Lett.*, 39(16):4671–4674, Aug 2014.

[69] D. Ouyang, J. Zhao, Z. Zheng, S. Ruan, C. Guo, P. Yan, and W. Xie. "110 W all fiber actively Q-switched thulium-doped fiber laser". *IEEE Photonics Journal*, 7(1):1–6, Feb 2015.

[70] C. Gaida, M. Gebhardt, T. Heuermann, F. Stutzki, C. Jauregui, and J. Limpert. Ultrafast thulium fiber laser system emitting more than 1 kW of average power. *Optics Letters*, 43(23):5853–5856, Dec 2018.

[71] S. D. Jackson and A. Lauto. "Diode-pumped fiber lasers: A new clinical tool?". *Lasers in Surgery and Medicine*, 30(3):184–190, 2002.

[72] Govind Agrawal. *Lightwave technology : components and devices*. 06 2005.

[73] John Buck. *Fundamentals of Optical Fibers*. John Wiley and Sons, 04 2004.

[74] Arnaud Malvache. *Optique non-lineaire a haute intensite : Compression d'impulsions laser Interaction laser-plasma*. PhD thesis, Ecole Polytechnique X, 2011.

[75] D. Gloge. "Weakly Guiding Fibers". *Appl. Opt.*, 10(10):2252–2258, Oct 1971.

[76] R. Brüning, Y. Zhang, M. Mclaren, M. Duparré, and A. Forbes. "Overlap relation between free-space Laguerre Gaussian modes and step-index fiber modes. *Journal of the Optical Society of America. A, Optics, image science, and vision*, 32:1678–1682, 09 2015.

[77] D. Marcuse. "Loss analysis of single-mode fiber splices". *The Bell System Technical Journal*, 56(5):703–718, May 1977.

[78] G. P. Agrawal. *Nonlinear Fiber Optics*. Academic Press, Elsevier, 2007.

[79] J. M. Dudley, G. Genty, and S. Coen. "Supercontinuum generation in photonic crystal fiber". *Rev. Mod. Phys.*, 78:1135–1184, Oct 2006.

[80] J. Sakai and T. Kimura. "Bending loss of propagation modes in arbitrary-index profile optical fibers". *Appl. Opt.*, 17(10):1499–1506, May 1978.

[81] C. Xia, Z. Xu, M. N. Islam, F. L. Terry, M. J. Freeman, A. Zakel, and J. Mauricio. "10.5 W time-averaged power mid-IR supercontinuum generation extending beyond 4 μm with direct pulse pattern modulation". *IEEE Journal of Selected Topics in Quantum Electronics*, 15(2):422–434, March 2009.

[82] Casimer DeCusatis. *Handbook of Fiber Optic Data Communication*. Elsevier, 2013.

[83] D. Grischkowsky and A. C. Balant. "Optical pulse compression based on enhanced frequency chirping". *Applied Physics Letters*, 41(1):1–3, 1982.

[84] R. H. Stolen, J. P. Gordon, W. J. Tomlinson, and H. A. Haus. "Raman response function of silica-core fibers". *J. Opt. Soc. Am. B*, 6(6):1159–1166, Jun 1989.

[85] F. Théberge, N. Bérubé, S. Poulain, S. Cozic, L. Robichaud, M. Bernier, and R. Vallée. "Watt-level and spectrally flat mid-infrared supercontinuum in fluoroindate fibers". *Photonics Research*, 6(6):609–613, Jun 2018.

[86] F. M. Mitschke and L. F. Mollenauer. "Discovery of the soliton self-frequency shift". *Opt. Lett.*, 11(10):659–661, Oct 1986.

[87] J. P. Gordon. "Theory of the soliton self-frequency shift". *Opt. Lett.*, 11(10):662–664, Oct 1986.

[88] M. Michalska, J. Mikolajczyk, J. Wojtas, and J. Swiderski. "Mid-infrared, super-flat, supercontinuum generation covering the 2-5 μm spectral band using a fluoroindate fibre pumped with picosecond pulses". *Scientific Reports*, 6:39138, 12 2016.

[89] T. Izawa, N. Shibata, and A. Takeda. "Optical attenuation in pure and doped fused silica in the IR wavelength region". *Applied Physics Letters*, 31(1):33–35, 1977.

[90] D. Tran, G. Sigel, and B. Bendow. "Heavy metal fluoride glasses and fibers: A review". *Journal of Lightwave Technology*, 2(5):566–586, October 1984.

[91] J. Swiderski, F. Théberge, M. Michalska, P. Mathieu, and D. Vincent. "High average power supercontinuum generation in a fluoroindate fiber". *Laser Physics Letters*, 11(1):015106, December 2013.

[92] S. Mitachi, T. Miyashita, and T. Kanamori. "Fluoride-Glass-Cladded Optical Fibres for Mid-Infrared Ray Transmission". *Electronics Letters*, 17:672–673, 02 1981.

[93] S. Mitachi, T. Miyashita, and T. Manabe. "Preparation of fluoride optical fibers for transmission in the mid-infrared". 23:196–201, 12 1982.

[94] D. C. Tran, C. F. Fisher, and G. H. Sigel. "Fluoride glass preforms prepared by a rotational casting process". *Electronics Letters*, 18(15):657–658, July 1982.

[95] `https://www.thorlabs.com/`.

[96] `https://www.leverrefluore.com/`.

[97] G. Tao, H. Ebendorff-Heidepriem, A. M. Stolyarov, S. Danto, J. V. Badding, Y. Fink, J. Ballato, and A. F. Abouraddy. "Infrared fibers". *Adv. Opt. Photon.*, 7(2):379–458, Jun 2015.

[98] I. H. Malitson. "Interspecimen comparison of the refractive index of fused silica". *J. Opt. Soc. Am.*, 55(10):1205–1209, Oct 1965.

[99] Fuxi Gan. "Optical properties of fluoride glasses: A review". *Journal of Non-Crystalline Solids*, 184:9 – 20, 1995. Non-oxide Glasses.

[100] F. Théberge, J.-F. Daigle, D. Vincent, P. Mathieu, J. Fortin, B. E. Schmidt, N. Thiré, and F. Légaré. "Mid-infrared supercontinuum generation in fluoroindate fiber". *Optics Letters*, 38(22):4683–4685, Nov 2013.

[101] C. L. Hagen, J. W. Walewski, and S. T. Sanders. "Generation of a continuum extending to the mid-infrared by pumping ZBLAN fiber with an ultrafast 1550-nm source". *IEEE Photonics Technology Letters*, 18(1):91–93, Jan 2006.

[102] Kun Liu, Jiang Liu, Hongxing Shi, Fangzhou Tan, and Pu Wang. "High power mid-infrared supercontinuum generation in a single-mode ZBLAN fiber with up to 21.8 W average output power". *Optics Express*, 22(20):24384–24391, Oct 2014.

[103] Zhijian Zheng, Deqin Ouyang, Junqing Zhao, Minqiu Liu, Shuangchen Ruan, Peiguang Yan, and Jinzhang Wang. "Scaling all-fiber mid-infrared supercontinuum up to 10 W-level based on thermal-spliced silica fiber and ZBLAN fiber". *Photon Research*, 4(4):135–139, Aug 2016.

[104] Ke Yin, Bin Zhang, Linyong Yang, and Jing Hou. "15.2 W spectrally flat all-fiber supercontinuum laser source with >1 W power beyond 3.8 μm". *Optics Letters*, 42(12):2334–2337, Jun 2017.

[105] Linyong Yang, Ying Li, Bin Zhang, Tianyi Wu, Yijun Zhao, and Jing Hou. 30-w supercontinuum generation based on zblan fiber in an all-fiber configuration. *Photon. Res.*, 7(9):1061–1065, Sep 2019.

[106] M. Michalska, P. Grzes, P. Hlubina, and J. Swiderski. "Mid-infrared supercontinuum generation in a fluoroindate fiber with 1.4 W time-averaged power". *Laser Physics Letters*, 15:045101, 04 2018.

[107] J.-C. Gauthier, V. Fortin, J.-Y. Carrée, S. Poulain, M. Poulain, R. Vallée, and M. Bernier. "Mid-IR supercontinuum from 2.4 to 5.4 μm in a low-loss fluoroindate fiber". *Optics Letters*, 41(8):1756–1759, Apr 2016.

[108] S. Liang, L. Xu, Q. Fu, Y. Jung, D. P. Shepherd, D. J. Richardson, and Shaif ul Alam. "295-kWpeak power picosecond pulses from a thulium-doped-fiber MOPA and the generation of watt-level >2.5-octave supercontinuum extending up to 5 μm". *Optics Express*, 26(6):6490–6498, Mar 2018.

[109] Tianyi Wu, Linyong Yang, Zhiyuan Dou, Ke Yin, Xuan He, Bin Zhang, and Jing Hou. "Ultra-efficient, 10-watt-level mid-infrared supercontinuum generation in fluoroindate fiber". *Opt. Lett.*, 44(9):2378–2381, May 2019.

[110] M. Schellhorn. Private communication, 2018.

[111] Arlee V. Smith and Binh T. Do. "Bulk and surface laser damage of silica by picosecond and nanosecond pulses at 1064 nm". *Appl. Opt.*, 47(26):4812–4832, Sep 2008.

[112] S. Roy Choudhury and Y. Jaluria. "Practical aspects in the drawing of an optical fiber". *Journal of Materials Research*, 13:483 – 493, 02 1998.

[113] R.M. Wood. *Laser-induced damage of optical materials*. 01 2003.

[114] K. Egashira and M. Kobayashi. Optical fiber splicing with a low-power co2 laser. *Appl. Opt.*, 16(6):1636–1638, Jun 1977.

[115] https://www.fujikura.co.uk/products/fusion-splicers-and-accessories/fusion-splicers-specialty/lazermaster-lzm-100-laser-splicing-system/.

[116] Lasers and laser related equipment – Test methods for laser beam widths, divergence angles and beam propagation ratios. Standard, International Organization for Standardization, February 2005.

[117] R. H. Stolen and Chinlon Lin. "Self-phase-modulation in silica optical fibers". *Phys. Rev. A*, 17:1448–1453, Apr 1978.

[118] Anthony E. Siegman. *Lasers*. University Science Books, 1986.

[119] J. H. Wray and John T. Neu. "Refractive Index of Several Glasses as a Function of Wavelength and Temperature". *J. Opt. Soc. Am.*, 59(6):774–776, Jun 1969.

[120] Poulain M. *"Fluoride Glass Composition and Processing"*. Academic Press, 1991.

[121] M.-A. Gagnon, V. Fortin, R. Valle, P. Lagueux, and E. Guyot. "Non-Destructive Testing of Mid-IR Optical Fiber Using Infrared Imaging". 01 2016.

[122] https://www.newport.com/n/fiber-optic-coupling.

[123] G. Millot, S. Pitois, P. Tchofo Dinda, and M. Haelterman. Observation of modulational instability induced by velocity-matched cross-phase modulation in a normally dispersive bimodal fiber. *Opt. Lett.*, 22(22):1686–1688, Nov 1997.

[124] C. Kneis, T. Robin, B. Cadier, F. Joulain, M. Poulain, I. Manek-Hönninger, M. Eichhorn, and C. Kieleck. "Mid-IR Supercontinuum

Generation in ZBLAN Fibers with High Output Power and High Conversion Efficiency". In *Advanced Solid State Lasers*, page AW4A.10. Optical Society of America, 2015.

[125] Robert R. Alfano. The supercontinuum laser source. 1989.

[126] C. Xia. *Mid-Infrared Supercontinuum Laser System and its Biomedical Applications*. PhD thesis, University of Michigan, 2009.

[127] `http://www.teledynejudson.com/products/indium-antimonide-detectors`.